The structure of a working catalyst ; from flat surfaces to nanoparticles
Roobol, S.B.

Cover Page

Universiteit Leiden

Author: Roobol, Sander Bas
Title: The structure of a working catalyst : from flat surfaces to nanoparticles
Issue Date: 2014-12-02
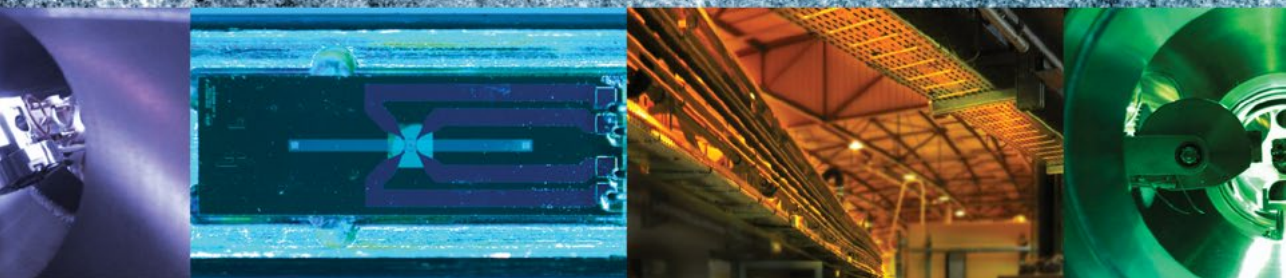
The structure of a working catalyst
From flat surfaces to nanoparticles

Sander Roobol

The structure of a working catalyst
From flat surfaces to nanoparticles

The structure of a working catalyst
From flat surfaces to nanoparticles

Proefschrift

ter verkrijging van
de graad van Doctor aan de Universiteit Leiden
op gezag van Rector Magnificus prof. mr. C. J. J. M. Stolker
volgens besluit van het College voor Promoties
te verdedigen op dinsdag 2 december 2014
klokke 11.15 uur

door

Sander Bas Roobol
geboren te Zeist
in 1985

Promotor:

 Prof. dr. J. W. M. Frenken
 Universiteit Leiden

Overige leden van de promotiecommissie:

 Prof. dr. E. R. Eliel
 Universiteit Leiden

 Dr. I. M. N. Groot
 Universiteit Leiden

 Dr. P. J. Kooyman
 Technische Universiteit Delft

 Prof. dr. E. Lundgren
 Lund University, Lund, Zweden

 Prof. dr. B. E. Nieuwenhuys
 Universiteit Leiden

 Prof. dr. ir. T. H. Oosterkamp
 Universiteit Leiden

In memory of my grandfather, dr. Kees Kruit.
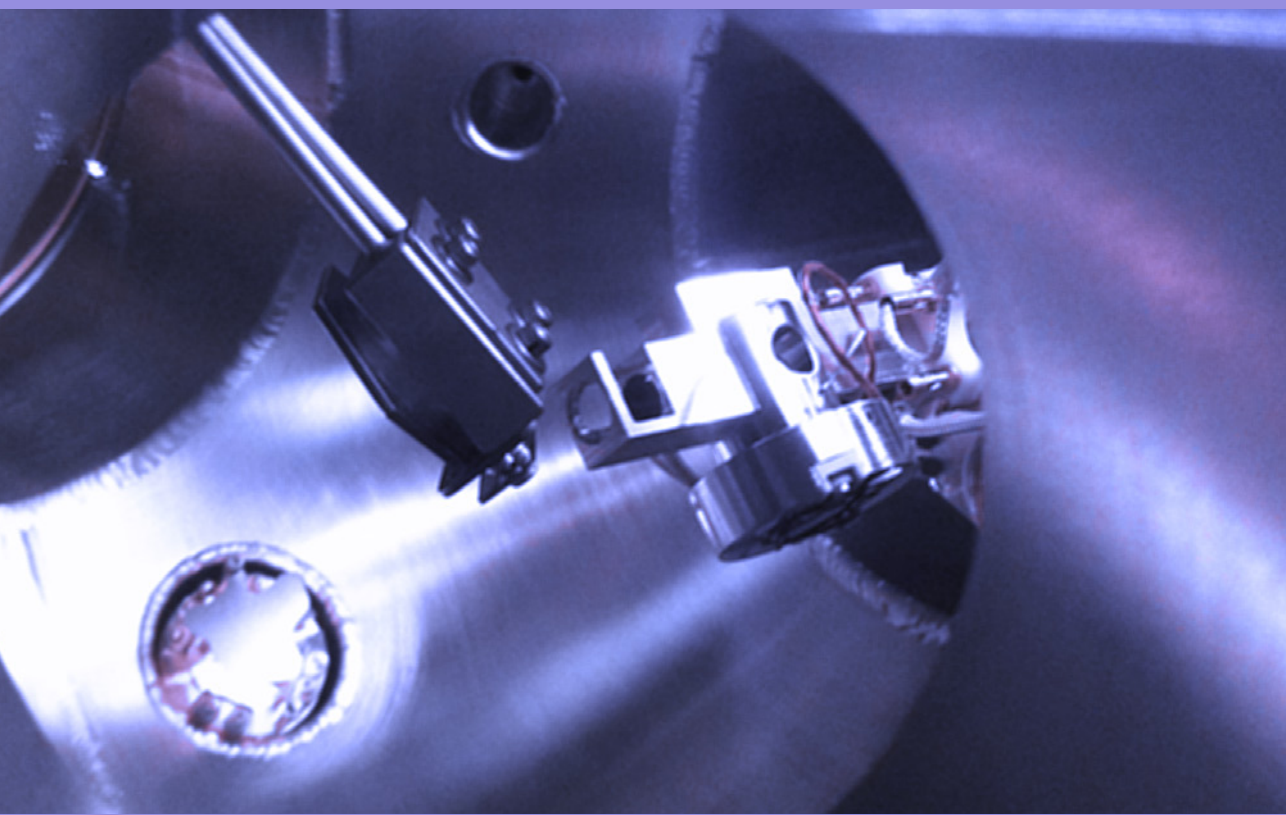
About this thesis

Catalysis is the working horse of the chemical industry. In many cases, it is a poorly understood process that takes place at the surfaces of nanoparticles under relatively harsh conditions, such as high pressures and high temperatures.

This thesis focuses on new approaches to acquire atomic-scale information on catalytic processes on metal nanoparticles in high-pressure, high-temperature conditions. This thesis starts with a general introduction that motivates the need for *operando* or *in-situ* observations and advocates the simultaneous use of a combination of atomic-scale measurement techniques. The body of this thesis is organised in two parts that can be read independently.

Part I takes a comprehensive approach to the development of novel instruments and methods for *in-situ* experiments on model catalysts under working conditions. It introduces the mechanical and electronic hardware of the ReactorAFM, the world's first high-pressure, high-temperature non-contact Atomic Force Microscope. In addition, it describes two software packages for the analysis of *in-situ* microscopy data, and for the analysis of surface X-ray diffraction data.

In part II we have applied our new instrument in combination with other, recently developed *in-situ* measurement techniques to study catalytic model systems at atmospheric pressures and elevated temperatures. We first describe a study of the interaction of gas mixtures of nitric oxide and hydrogen on the Pt(110) surface, using surface X-ray diffraction. This study serves as a stepping stone for the next chapter, where we exposed a Pt nanoparticle model catalyst to mixtures of nitric oxide and hydrogen in a high-pressure reaction cell in a transmission electron microscope. Finally, we have investigated spontaneous reaction oscillations on Pd nanoparticles during the catalytic oxidation of carbon monoxide. Using a combination of four *in-situ* techniques, including our new ReactorAFM, we have established the periodic formation and reduction of a thin oxide shell on the nanoparticles during the oscillations.

As will be explained in the first chapter, the differences between the idealised world of traditional surface science and the complex world of practical catalysis are commonly categorised into the *pressure gap* and the *materials gap*. The approach taken in this thesis to combine several *in-situ* measurement techniques, is necessary to bridge the *pressure gap* and at the same time take a significant step across the *materials gap*.

Contents

Chapter 1

Introduction

Surface science and heterogeneous catalysis are a natural match, and this thesis further strengthens this alliance. In both fields, the interaction of molecules with solids forms a central topic. Although the two fields are complementary, as they approach this topic from two different sides, it is usually difficult to directly relate results obtained in one field to results obtained in the other. Bridging this gap has been a driving force for the work described in this thesis.

Traditional catalysis research can be seen as taking a top-down approach. Understanding is derived from ensemble measurements on the reactants and products, e.g. the catalyst activity (how much reactant is converted) and selectivity (how much of the desired product is formed compared to undesired byproducts). This is often combined with extensive catalyst characterisation before and after reaction, using spectroscopy and microscopy. The challenge of this approach is usually in the catalytic system itself, for example because there are several competing reactions, or because the catalyst has a complex composition or structure. The gain is relevant knowledge for applications in e.g. the chemical industry, but the knowledge is often phenomenological in character.

Catalytic surface science takes a bottom-up approach and uses highly simplified model systems under minutely controlled conditions. A typical surface-science experiment studies a flat single crystal metal surface, often during interaction with molecules, in Ultrahigh Vacuum (UHV), and often at cryogenic temperatures. The difficulty of such experiments is to exert near-perfect control over the sample, and at the same time apply highly sensitive and often very delicate measurement techniques. When succeeding in both, the experiment gives information on the atomic scale, e.g. on the chemical state or the atomic structure of the surface or the adsorbates.

The pressure gap and the materials gap

In practice, it is often difficult to relate results obtained by the traditional chemical approach to results obtained by surface science techniques. There are only a few documented cases in which the activity and selectivity of a real catalyst under realistic conditions can be predicted even to within one order of magnitude, based on the extrapolation of surface-science experiments[1, 2]. This suggests that there are intrinsic qualitative differences, for example in the reaction mechanisms, that are introduced when the experimental conditions differ too much. The two fields are often said to be separated by two gaps, the *pressure gap* and the *materials gap*. This thesis describes work done in the field of *in-situ* catalysis, in which we have aimed to overcome these gaps and combine the atomic-scale sensitivity of surface science with the relevant conditions of traditional catalysis research.

The *pressure gap* refers to the difference in operating pressure and temperature between applied catalysis and traditional surface science. In the chemical industry, catalysis typically takes place at pressures in the range of 1-100 bar and temperatures up to 1000 K[3]. Classical surface science uses low pressures in the range of 10^{-10} to 10^{-6} mbar, and a wide range of temperatures, down to a few K and beyond 1000 K[4]. A naïve justification to extrapolate surface science results to real catalysis would be to use thermodynamics to argue that the conditions can be chosen such that the chemical potentials of the involved species are the same in certain low-pressure, low-temperature conditions as they are in the real high-pressure, high-temperature conditions. However, real catalytic processes are never in thermodynamic equilibrium and the role of kinetics must be taken into account. The kinetics strongly depend on temperature, and the enormous difference in kinetic limitations between high and low temperature are the cause of the *pressure gap*. These kinetic limitations could be either on the catalyst surface (e.g. due to barriers for diffusion, adsorption/desorption or reaction steps) or in the gas phase (where not only diffusion but also fluid dynamics needs to be considered).

It is important to realise that it is not enough to operate at high pressure and high temperature to fully overcome the *pressure gap*. This only gives representative kinetics on the catalyst surface, given a certain chemical potential for the relevant gas species. But the composition of the gas phase, and thus the chemical potential, is not necessarily representative. To reach true catalytic conditions, the activity of the catalyst needs to be representative as well, not only when expressed in converted molecules per site per second, but also when expressed in terms of the (local) partial pressures of the products and reactants. This means that the reactor volume and the residence time of the gas in the reactor need to be matched to the catalyst activity and surface area, and for a surface-science experiment this typically means that the reactor volume needs to be minimised. Only then, the true interplay between catalyst structure and reactivity can be studied. This interplay goes both ways: the

reactants and the products affect the catalyst structure, but the catalyst structure influences the activity and thus the presence of reactants and products[5].

The *materials gap* is due to the difference in complexity of catalysts between industrial catalysis and traditional surface science. Real, commercial catalysts are typically multi-scale materials, e.g. metal nanoparticles, dispersed on a three-dimensional, porous oxide support, pressed into centimetre-sized pellets. The flat metal surfaces used in surface science are easier to understand, but lack many of the features of a real catalyst. For example, nanoparticles have a much larger variety of adsorption sites than extended flat single-crystal surfaces[6] and they can have a different electronic structure from the bulk material[7]. Additional effects arise from the interaction between the metal particle and the support, e.g. via spillover effects[8] or further changes in the electronic structure[9].

New instrumentation to bridge the gaps

New instrumentation is needed to bridge the *pressure gap* and the *materials gap* and combine the best of both approaches. The ambition is to combine the atomic-scale sensitivity from surface science with the applicability and relevance of traditional catalysis research. In other words, to obtain information on the fundamental atomic-scale mechanisms that are actually at play in a real catalyst under real conditions. The first part of this thesis is dedicated to the development of new instrumentation for this purpose.

Several *in-situ* techniques are already available, some of which have been developed very recently. These include Scanning Tunneling Microscopy (STM)[10, 11], Transmission Electron Microscopy (TEM)[12, 13], several hard X-ray scattering techniques[14, 15], several variants of X-ray absorption spectroscopy[16], X-ray Photoelectron Spectroscopy (XPS)[17], and infrared spectroscopy[18]. Preferably, these techniques should be used simultaneously with traditional chemical techniques such as mass spectrometry and calorimetry. In addition to these experimental techniques, theoretical approaches such as the combination of Density Functional Theory (DFT)[19] with Kinetic Monte-Carlo[20] and fluid dynamics simulations[21] can be also considered to bridge the *pressure gap*.

This thesis takes a multi-technique approach to *in-situ* catalysis research. We have applied new and existing *in-situ* measurement techniques to study the fundamentals of several catalytic reactions. The latest technique is Atomic Force Microscopy (AFM), for which we have built a novel instrument with unique capabilities. The other *in-situ* techniques that we have applied are TEM and three X-ray scattering techniques: X-Ray Diffraction (XRD), Surface X-ray Diffraction (SXRD) and Grazing Incidence Small Angle X-ray Scattering (GISAXS).

The first part of this thesis describes the development of new instrumentation

for *in-situ* catalysis in all its aspects: mechanical hardware, electronic hardware, and software. A major part of this is devoted to the ReactorAFM that we have developed as part of this thesis work. The ReactorAFM is the world's first high-pressure, high-temperature Non-Contact AFM.

Chapter 2 describes in detail the design and performance of this instrument. In short, the ReactorAFM can image model catalysts, not only flat surfaces but also supported nanoparticles, at temperatures up to 600 K and pressures up to 6 bar, with a resolution in the order of a nanometre. The instrument consists of a 0.5 ml high-pressure flow reactor joined with an AFM scanner based on a quartz tuning fork. The reactor/scanner is located in an ultrahigh vacuum system to be able to use standard surface-science techniques to prepare and characterise the sample. The true value of the ReactorAFM is demonstrated in chapter 7, where it provides an essential element in a combined study with three other *in-situ* techniques, showing that it can bridge both the *pressure gap* and the *materials gap* while providing information on the atomic scale.

In the context of instrumentation development for complex experiments, new hardware cannot be seen separately from specialised software, in order to deal with the increasing complexity of the generated data. Chapter 3 introduces *Spacetime*, a user-friendly data browser for *in-situ* experiments. During *in-situ* microscopy studies, a variety of signals is recorded in addition to the images, for example the sample temperature, the gas flow settings and the output of a mass spectrometer. These signals are typically recorded independently from the microscopy data, often on separate computers, by a variety of software packages, ranging from home-built LabVIEW programs to professionally designed, commercial applications. *Spacetime* can provide an integrated overview of the heterogeneous datasets obtained during *in-situ* experiments, and has now become an essential tool in our laboratory.

A second software package is described in chapter 4. Thanks to recent developments in the field of SXRD, the data acquisition rate has increased tremendously. We have developed *BINoculars* as a tool for the reduction and analysis of large datasets obtained by a two-dimensional X-ray detector. When operating at a modern diffraction beamline and with access to a computing cluster, it allows the acquisition and processing of large-area, high-resolution reciprocal space intensity maps on a time scale of tens of minutes. It is already considered part of the basic toolkit by the staff of the ID03 beamline at the ESRF and it has received interest from several recurring users.

Operando catalysis

The second part of this thesis concerns studies on relevant catalytic model systems with several *in-situ* or *operando* techniques.

We start with two studies on the reduction of nitric oxide (NO) by hydrogen (H_2) using a platinum catalyst. This system can be seen as a model reaction for the reduction of NO that takes place in the three-way car catalyst. Since no literature was available on high-pressure surface-science experiments on this reaction, we started with a flat single crystal surface. In chapter 5, SXRD is used to study the interaction of mixtures of H_2 and NO with a Pt(110) surface at 1 bar and 100-400°C. This surface orientation of Pt easily reconstructs, and we have observed several new reconstructions under high-pressure conditions. In addition, after prolonged exposure to NO/H_2 mixtures, the flat surface started faceting into vicinal orientations close to the (320) orientation. As many catalytic reactions take place predominantly on step sites, it is extremely relevant to understand when and how a catalyst might be actively forming steps. In this case, we suggest that the mechanism for the step formation is related to the surface stress of the Pt(110) surface, which is dramatically altered by the high coverage of adsorbed NO molecules due to their repulsive interaction. This demonstrates that high-pressure restructuring mechanisms can not exclusively be interpreted or predicted on the basis of adsorption energies at different sites, but also the surface stress needs to be considered. This is a true *pressure gap* effect: the high NO coverage, combined with sufficient mobility of the metal atoms on the surface to reorder on this scale, can only be obtained under high-temperature, high-pressure conditions.

Having seen this mechanism on flat surfaces, it is natural to wonder what this means for a more realistic catalyst, i.e. a system of metal nanoparticles. This is the topic of chapter 6, where we used TEM in combination with nanoreactors, specially designed for *in-situ* catalysis studies[13]. In general, the shape of a nanoparticle is dictated by the relative free energies of all interfaces between the particle and the gas environment. We observed that initially faceted particles became more rounded under the influence of NO, i.e. the flat, low-index facets broke up into vicinal surfaces. Thanks to the measurements on the flat (110) surface in the previous chapter, we can now understand that this is the logical nanoparticle analogue of the same mechanism: adsorbate-induced stress is held responsible for the change in surface free energies.

For the last chapter, we took on the archetypal model system of CO oxidation on palladium, but brought it to the next level by bridging the *materials gap*. This study builds on the vast amount of surface-science knowledge, both at low- and at high-pressure, that is already available for CO oxidation catalysed by palladium surfaces. In addition, CO oxidation at high pressures is a great example to show the defining difference between high-pressure surface science and *in-situ* catalysis. The reason for this is the existence of a diffusion-limited high-reactivity regime, which is accompanied by large gradients in the CO partial pressure. This shows that aspects such as reactor design cannot be neglected. High-pressure surface science

can be used to study surface structures, but the relevance for catalysis needs to be established from a surface-sensitive, *in-situ* catalytic measurement.

Apart from taking a true *in-situ* approach to bridge the pressure gap, chapter 7 also bridges the *materials gap*, by moving beyond flat surfaces to a supported nanoparticle model system. Using size-selected Pd particles on a Al_2O_3 substrate, we observed reaction oscillations: at constant conditions (external heating power and gas feed), the system periodically switches between a high-reactivity regime and a low-reactivity regime. Here, our multi-technique approach really shows its power: by combining XRD, GISAXS, AFM and TEM, all *in-situ* during high-temperature, high-pressure reaction conditions, we have resolved a key ingredient of the mechanism of the reaction oscillations by establishing the presence of a 1 nm thin oxide shell, which is only present during the high-reactivity part of the oscillation period.

A multi-technique approach

The multi-technique approach to *in-situ* catalysis, as advocated in this thesis, is imperative. There is no single *in-situ* technique that can tackle all aspects of even the simplest catalytic reactions.

By combining several *in-situ* techniques, we can gain detailed understanding not only of archetypal model reactions like CO oxidation, but also of more complex catalytic systems.

Part I

Instruments and methods
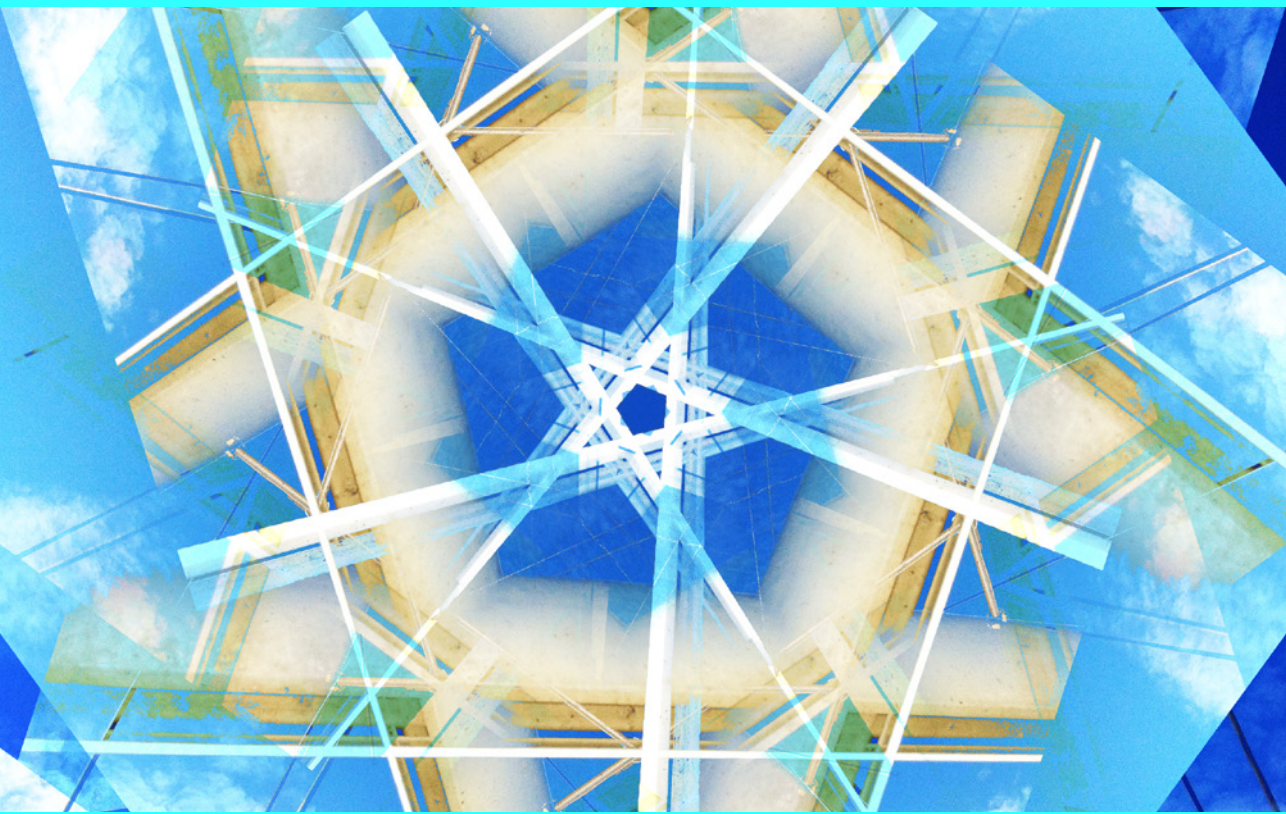
Chapter 2

The *ReactorAFM*: Non-Contact Atomic Force Microscope operating under high-pressure and high-temperature catalytic conditions

An Atomic Force Microscope (AFM) has been integrated in a miniature high-pressure flow reactor for in-situ observations of heterogeneous catalytic reactions under conditions similar to those of industrial processes. The AFM can image model catalysts such as those consisting of metal nanoparticles on flat oxide supports in a gas atmosphere up to 6 bar and at a temperature up to 600 K, while the catalytic activity can be measured using mass spectrometry. The high-pressure reactor is placed inside an Ultrahigh Vacuum (UHV) system to supplement it with standard UHV sample preparation and characterization techniques. To demonstrate that this instrument successfully bridges both the *pressure gap* and the *materials gap*, images have been recorded of supported palladium nanoparticles catalyzing the oxidation of carbon monoxide under high-pressure, high-temperature conditions.

2.1 Introduction

Fundamental research on heterogeneous catalysis has been one of the driving forces behind the development of the field of surface science. However, the idealised world of surface-science experiments in Ultrahigh Vacuum (UHV) is radically different from industrial catalytic processes.

While traditional surface chemistry research takes place on single crystal surfaces at pressures below 10^{-6} mbar and temperatures ranging from a few K to beyond 1000 K, the chemical industry uses reactors at pressures that are easily 10 orders of magnitude higher, and only elevated temperatures. In addition, a commercial catalyst usually consists of a complex multi-scale material, e.g. metal nanoparticles on some porous oxide support pressed into cm-sized pellets, whereas the typical surface-science experiment is performed on single crystal samples that are extremely flat and homogeneous (the only structure is on the atomic scale, i.e. the crystal lattice).

These two differences between the conditions in traditional surface science and industrial catalysis are known as the *pressure gap* and *materials gap* respectively. It is now accepted that it is often incorrect to extrapolate observations across those gaps. This is due to kinetic barriers that cannot be overcome at low temperatures[20], differences in coordination number between single crystal surfaces and nanoparticles[6], and metal-support interactions[8, 9].

During the last decade new instruments have been developed that bridge the pressure- and/or materials gap and allow surface-sensitive in-situ measurements at the atomic or molecular scale. These instruments are based on either averaging techniques or real-space microscopy.

The averaging techniques are all photon based. Examples are vibrational sum frequency generation laser spectroscopy[18] and near-ambient pressure X-ray photoelectron spectroscopy[17], giving information on the vibrational states of adsorbed molecules and the chemical state of atoms respectively. A third example is surface X-ray diffraction (SXRD)[22] that provides information on surface structure.

Two approaches are starting to deliver microscopic structural information under catalytic conditions. One is the development of ultrathin reactors for transmission electron microscopy[13, 23]. The other is formed by scanning probe microscopes (SPMs). While electron-based techniques are challenging at high pressures because of the short mean free path of electrons, scanning probes do not have this intrinsic limitation. The potential of scanning tunneling microscopy (STM) for in-situ catalysis studies was first explored in 1992[24]. Twenty years later our group was the first to demonstrate atomic resolution under high-pressure, high-temperature conditions using the ReactorSTM[11, 25].

Although the ReactorSTM bridges the *pressure gap*, it can only operate on conductive samples, usually in the form of metal single crystals. To bridge the *materials*

gap, a different scanning probe technique is needed: Atomic Force Microscopy (AFM). STM uses an electrical current to probe the sample, whereas AFM uses the interaction force between tip and sample and is independent of the conductivity of the sample. The typical, more realistic, model catalyst that can only be imaged with AFM would consist of a flat oxide substrate, for example a single crystal of $\alpha-Al_2O_3$ or quartz, with metal particles on top with a diameter of 1-100 nm of some catalytically active material, for example a pure metal or an alloy.

This chapter introduces the *ReactorAFM*. It is based on the proven design of the ReactorSTM, but its capability to image supported nanoparticles adds unique value for in-situ catalysis research. Some other variable pressure AFMs have been reported in literature. The easiest approach is to operate a standard AFM in an environmental chamber[26, 27], but this severely limits the operating temperature range and choice of gases (e.g. no corrosive gases). A more advanced approach uses a high-pressure flow cell that is separated from the piezo of the AFM scanner by a flexible membrane, to operate up to 423 K and 6 bar in liquids[28], or up to 350 K and 100 atm in supercritical CO_2[29]. These two instruments are limited to static AFM (i.e. contact mode) and constant temperature (long equilibration times), but could in principle be applied to catalytic systems. The *ReactorAFM* uses a similar concept with a high-pressure cell that is separated from the scanner, but has superior characteristics for catalysis research.

2.2   Design specifications

The purpose of the *ReactorAFM* is to image heterogeneous catalytic processes, with gaseous reactants and model catalysts consisting of nanoparticles on a flat substrate under conditions relevant for industrial applications. The design specifications described here are a delicate balance between high-resolution imaging, realistic operating conditions and technical feasibility.

The catalytic reactions in the *ReactorAFM* must take place under conditions similar to those used in industry, which can be characterised by temperatures ranging from 400 to 1000 K and pressures from 1 to 100 bar. We limit ourselves to the low side of this pressure regime, and to a maximum sample temperature of 600 K, to allow the use of elastomers to seal off the high-pressure cell. In this way, a very compact design can be made for the reactor and scanner, which has distinct advantages related to mechanical stability, thermal management and gas handling, as will be discussed in section 2.3.

Under any of these operating conditions, the AFM scanner must be able to resolve nanoparticles supported on flat surfaces with sufficient detail: the minimal requirements are a lateral resolution of 1 nm and a vertical resolution of 0.1 nm, with a range of at least 1 μm in each direction. Ideally, atomic resolution on flat surfaces

should be achieved, corresponding to one order of magnitude improvement in lateral and vertical resolution.

The AFM scanner should be sufficiently stable to allow uninterrupted imaging of a single feature on the surface for at least 1 hour during high-temperature, high-pressure conditions. This places constraints on the thermal drift of the scanner and the thermal drift of the force sensor. In particular, the drift in the lateral directions must be less than 50 nm/min and the vertical drift per hour must be less than the vertical piezo range of 1 μm. After a temperature change of more than 25 K a thermalisation period of at most 30 minutes is acceptable to stabilise the force sensor.

To interpret atomic-scale microscopy images of catalytic processes, it is essential that the starting situation is known in great detail, i.e. the structure and composition of the freshly prepared sample needs to be controlled down to the atomic scale. This requires standard surface-science techniques that operate in UHV. In addition, the gases and catalyst materials must have the highest available purity (impurity level typically 1-100 parts per million), and the sample cannot be transferred through air once it has been prepared in UHV. Thus, the high-pressure reactor and scanner must be embedded in a UHV system equipped with sample preparation and analysis tools. For some samples exposure to air might not be a problem, so it should be possible to transfer the sample out of the UHV system to use external preparation or characterisation techniques.

Highly relevant for catalysis is the correlation of the surface structure of the catalyst with the activity and selectivity of the process, i.e. the rate of formation of the reaction product(s). To do this with high sensitivity and time resolution, the reactor needs to be operated in a flow configuration and the gas stream leaving the reactor has to be analysed continuously. The gas manifold that feeds the reactor needs to allow independent control over flow and pressure, to be able to mix several gases over a wide range of mixing ratios. To allow time-resolved experiments, any change in parameters must be performed with a transition time shorter than 5 seconds.

For accurate reactivity measurements it is important to avoid spurious catalytic activity on components of the reactor, so all components that are exposed to the high-pressure gases must be inert under the conditions to which they are subjected during normal operation. This means for example that stainless steel is an acceptable material for the capillaries of the gas handling system, which is at room temperature, but not for a reactor wall that will become hot during operation.

In summary, the requirements are:
- Imaging: Height-resolution of 0.1 nm on flat surfaces and supported nanoparticles, lateral resolution of 1 nm, under high-pressure, high-temperature conditions, e.g., at 1 bar and 450 K. Acquisition time of 1 minute per frame.

- High-temperature operation: Sample temperature from room temperature up to 600 K. Thermal drift below 1 μm/h (piezo range) in z and below 50 nm/min in x and y, after an initial thermalization period of 30 min.
- High-pressure gas conditions: reactor pressure beyond 1 bar. Arbitrary gas mixtures up to 1:100 ratio. Time constants in gas system (refresh rate of reactor, delay between gas system and reactor, delay between reactor and gas analyser) below 5 s.

2.3   Design

Many of the design specifications are met by the ReactorSTM, an instrument that has been developed in our group and has recently been described in this journal[11]. Most of the supporting infrastructure (UHV system, gas handling, vibration isolation) and the general design of the scanner/reactor (coarse approach, UHV/reactor sealing, sample holder) could be directly used for the AFM, and will not be described in detail here. The AFM scanner however is substantially different from the STM version.

The AFM scanner is based on the piezoelectric readout of a quartz tuning fork (QTF). The miniature design of the reactor of the ReactorSTM (volume 0.5 ml) does not offer optical access to the tip, ruling out the laser deflection techniques that are common in many AFMs. Quartz is chemically inert, and exceptionally high resolution has been reported using QTF-based AFMs[30, 31], making it the ideal choice for the *ReactorAFM*.

2.3.1   UHV system

The UHV system is identical to that of the ReactorSTM, and is equipped with several standard techniques for sample preparation (annealing using electron bombardment or radiation heating to over 1000 K, low pressure exposure to oxygen, hydrogen or other gases, ion bombardment, metal deposition) and characterization (low-energy electron diffraction, Auger electron spectroscopy, and in a later stage also X-ray photoelectron spectroscopy). The system is divided into several compartments, one chamber containing the high-pressure AFM scanner, another chamber for sample preparation, a third chamber for analysis, and a load lock to transfer samples in and out of the system. This configuration separates the tasks and makes it possible to use corrosive gases for sample preparation, as the sensitive components in the other chambers are not exposed to those gases. A base pressure in the low 10^{-10} mbar range is routinely achieved after bake-out, using a corrosion resistant turbo-molecular pump and several ion pumps combined with titanium sublimation pumps.

Samples can be transferred throughout the setup and into the *ReactorAFM* without exposure to air. The sample holders are equipped with 5 electrical connections,

two for a heating filament, two for a K-type thermocouple connection and one to set the sample bias and/or measure (tunnelling) currents. The sample is electrically isolated from the body of the sample holder. The thermocouple is kept outside the high-pressure environment and if possible it is laser spot-welded directly to the side of the sample. For non-metallic samples this is usually not possible, so the thermocouple is welded to a molybdenum backplate that supports the sample. For a weakly heat-conducting oxide substrate this is estimated to limit the accuracy of the temperature measurement to a few tens of K.

The reactor with scanner is isolated from building vibrations by a spring suspension system with eddy current damping. The UHV setup is supported by four laminar-flow air legs and rests on a separate foundation.

2.3.2 Gas system

A computer-controlled gas system mixes up to 5 different gases at ratios ranging from 1:1 up to 1:100, and the mixtures can be made to flow through the reactor (typical flow $5 \, \text{ml}_n/\text{min}$, up to 6 bar). It is equipped with a carbonyl trap consisting of a copper capillary filled with copper braids that is heated to 250°C. A separate UHV system equipped with a quadrupole mass spectrometer (QMS) and pumped by a turbo molecular pump is used to continuously sample the reaction products. The entire gas system is electrically isolated from the main UHV system by the use of PEEK capillaries to reduce interference from the computer and the gas controllers. The system is optimised for minimal unrefreshed volume and in combination with the small reactor volume this results in a response time of several seconds, e.g. when changing the composition of the gas mixture. To achieve high purity gas flows, the manifold is bakeable to 70°C.

2.3.3 High pressure reactor with AFM scanner

Figure 2.1 shows the design of the AFM scanner in the high-pressure reactor cell. The model catalyst sample (typically $10 \times 10 \, \text{mm}^2$, thickness 250 µm to 1 mm) forms the topside of the reactor, and the AFM tip approaches it from below. A Kalrez O-ring forms a leak-tight seal between the sample and the top of the scanner and closes the reactor volume. The sample is heated from the rear by a filament. Kalrez is specified for continuous use up to 600 K, and since the O-ring is in direct contact with the sample, this determines the maximum operating temperature of the scanner.

The scanner, O-ring and sample are pressed together by inflating a bellows with pressurised air. Three spacers limit the compression of the O-ring and define the mechanical loop of the scanner, resulting in a very stiff and compact design.

A lead zirconate titanate (PZT) piezo tube[33] is used for both the coarse approach and the three-dimensional scanning motion, the latter having a lateral range

high pressure reactor volume
flat oxide sample
Kalrez O-ring
zerodur body with gas channels
viton O-ring
reactor wall

sample holder
sapphire spacer
heating filament
sample backplate
sample clamp
sample mounting screws
isolation ceramics
spacer legs

scanner with integrated coarse approach
quartz tuning fork
sliding tip-holder
electrical shielding
ceramic spacers
magnet
tip-holder guidance tracks
piezo tube

Figure 2.1. The AFM version of the scanner/reactor. The Quartz Tuning Fork (QTF) is mounted on a magnetic rod that can slide up and down inside the piezo tube. The sliding rod rests on two tracks and is held in place by a magnet. The small high-pressure reaction cell is defined by the sample surface, two polymer O-rings, the reactor body with gas channels, and the holder for the sliding rod and tracks. The piezo tube and the sample heating filament are outside the reactor volume and remain in UHV.

1mm
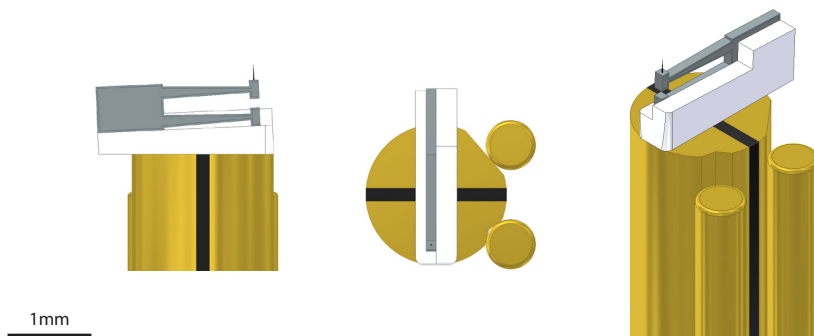
Figure 2.2. Three views of the sliding rod with the QTF. The rod consists of two halves, each in contact with one of the two tracks. The slider has a special shape with a groove and a flat side to have a well-defined contact area with the two rods. The QTF is glued in a QPlus[32] configuration on a ceramic piece that defines a 2.5° tilt to ensure the upper prong is the highest point of the assembly. The two electrodes of the QTF are each connected by thin gold wires to one of the halves of the sliding rod (not shown). The two tracks traverse the reactor wall and are connected by coaxial cables to the preamplifier outside the vacuum system.

of approximately 2 μm and vertical range of 1 μm. The piezo tube is located outside the high-pressure cell to avoid convective heating via the gas phase, which would result in chaotic thermal drift when operating at high temperatures.

The QTF with the AFM tip is mounted on a rod that is magnetically clamped inside the piezo tube. The rod can slide up and down during coarse approach using a stick-slip motion. The rod consists of two halves, and is held against two tracks by a Sm_2Co_{17} magnet located next to the piezo tube. Both the slider and the tracks are made of machine steel and are gold-coated. With this coating, the static friction between the slider and tracks is sufficient to ensure that the slider does not move during normal scanning motion, but low enough to allow the stick-slip motion during coarse approach.

The tracks supporting the slider are mounted on a capped cylinder made of polyetherimide (PEI), which is located in the piezo tube. An additional cylinder made of aluminium between the PEI component and the piezo tube provides electrical shielding from the high piezo voltages. The PEI cylinder also forms part of the reactor wall, so the piezotube is not exposed to the high-pressure gases to avoid chemical and thermal stability issues.

The two tracks are also used as feedthroughs for the two electrical signals of the QTF through the PEI reactor wall. Each track is in contact with one of the two halves of the slider. The tracks traverse the (insulating) PEI component and are connected by coaxial cables to floating-shield BNC feedthroughs on the UHV flange of the scanner.

2.3.4   Tuning fork and tip

The quartz tuning fork is a commercial miniature crystal with a resonance frequency of 32.768 kHz, type number CM8V-T1A from Micro Crystal AG, that has been shortened by wafer cutting such that the prong length is reduced from 1.6 mm to 1.15 mm without altering its electrode topology. After modification, the overall dimensions of the tuning fork are $1.9 \times 0.5 \times 0.12$ mm^3 and the fundamental resonance frequency is about 96 kHz.

The tuning fork is mounted using Stycast 2850 epoxy (with catalyst 24 LV) on the slider in the QPlus configuration[32], i.e. the lower prong is completely fixed in glue and the upper prong acts as a single piezoelectric cantilever. After gluing, the Q-factor of the first resonance at ambient conditions is $3 \cdot 10^3$. A ceramic (Macor[35]) spacer is used to tilt the tuning fork to an angle of 2.5° to ensure that the apex of the upper prong is the first part to come in contact with the sample surface. The resulting assembly is shown schematically in figure 2.2, and in figure 2.3.

On the apex of the upper prong of the tuning fork a micrometre-sized tip is grown using Electron-Beam Induced Deposition (EBID) of platinum using a Scanning Electron Microscope (SEM). This is done at room temperature in a FEI
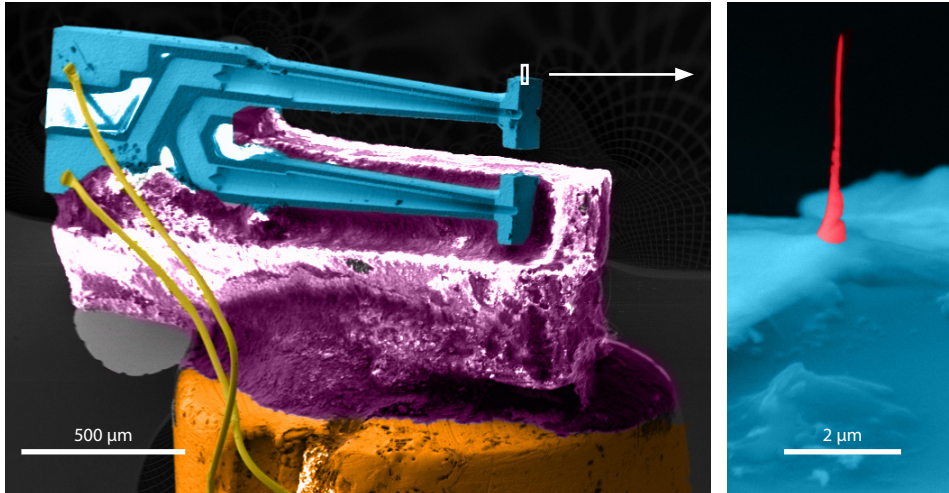
Figure 2.3. Scanning Electron Microscopy images with false colours for enhanced contrast of the QTF glued on a ceramic spacer which is glued to the slider, with a close-up of the apex of the upper prong. The tip is grown using electron-beam-induced deposition of platinum from a $MeCpPtMe_3$ precursor[34].

Nova NanoSEM 200 with $MeCpPtMe_3$ as precursor[34], resulting in a structure consisting of 16 atom% platinum, the remainder being amorphous carbon[36]. Typical growth parameters are 15 keV electron energy, beam current of 1.4 nA, beam focused to a single spot of 5 nm, pressure $3 \cdot 10^{-5}$ mbar, for 2-5 minutes. This results in a tip with a length of 2-5 μm and a diameter of 0.1 μm. The radius of curvature of the tip apex is 30 nm. The tip is positioned on one of the electrodes of the tuning fork, but the conductivity is too low to measure tunneling currents. The tip is mechanically stiff enough for AFM measurements, but it can easily be wiped off with a tissue and replaced with a new one if needed.

The electrical connections from the tuning fork electrodes to the slider are made by ball bonding using 25 μm diameter gold wires. The electrical path continues via the tracks that support the slider, followed by coaxial cables to the UHV feedthroughs.

2.3.5 Electronics

The AFM operates in a mode known as Non-Contact (NC) or Frequency-Modulation (FM), a technique that has been demonstrated to even give sub-atomic resolution and quantitative force measurements for sufficiently sharp tips[37]. In this mode, a cantilever is oscillated at resonance (frequency typically tens to hundreds of kHz) with an amplitude in the range of 10 pm to 100 nm. When the tip is near the surface, the tip-sample interaction force gradient will influence the effective spring

coefficient of the mechanical oscillator and this results in a shift of the resonance frequency. In the case of dissipative forces, there is also a decrease of the amplitude and an additional phase shift. The resonance frequency is measured using a phase-locked loop. The output signal of the phase-locked loop is used as the input for the height feedback loop of the AFM scanner in order to trace the surface at constant frequency shift. A separate feedback system adjusts the drive amplitude to keep the oscillation amplitude constant, thereby ensuring that the surface of constant frequency shift corresponds to a surface of constant force gradient. The drive signal of this amplitude feedback loop is recorded in a separate channel and can be used to derive the dissipative force.

The tuning fork motion is controlled via an excitation/detection circuit located directly outside the UHV system. It is based on a circuit introduced by Grober et al.[38], which compensates for the stray capacitance of the tuning fork, and measures the (oscillating) current through the tuning fork with an I-V convertor when it is driven at resonance by an external oscillator voltage source. The I-V converter is based on the OPA657 operation amplifier from Texas Instruments and has a gain of 1 V/nA and a bandwidth of 100 kHz.

A Zurich Instruments HF2LI lockin amplifier with phase-locked loop detects the shift in resonance frequency of the QTF and supplies the oscillating drive voltage at resonance. The height feedback and scanning is performed using high speed SPM electronics from Leiden Probe Microscopy[39].

2.4 Performance

2.4.1 Imaging

Due to limitations of the SPM control electronics it was not possible to systematically characterise the performance of the *ReactorAFM* using force-distance curves. Instead, monoatomic terraces and steps on the (111) surface of a silver crystal have been imaged, in UHV and in flows of ethylene (figure 2.4). These images show a lateral resolution of 5 nm and a vertical resolution of 0.05 nm, as determined from the line profiles. The lateral resolution is presumably limited by the sharpness of the EBID tip.

A catalytically more relevant demonstration is the imaging of palladium nanoparticles on a single crystal of $\alpha-Al_2O_3$. Figures 2.5 and 2.6 show these particles at 425 and 475 K in two mixtures of carbon monoxide, oxygen and argon at 1 bar. This sample has been produced ex-situ by a spark-discharge method[40]. Ex-situ sample preparation gives additional flexibility, for example this spark-discharge method produces particles with a well-defined size, but it adds the risk of introducing contaminations during sample transfer. Even though the lateral dimensions of the images of the particles are influenced by the shape of the tip — a common
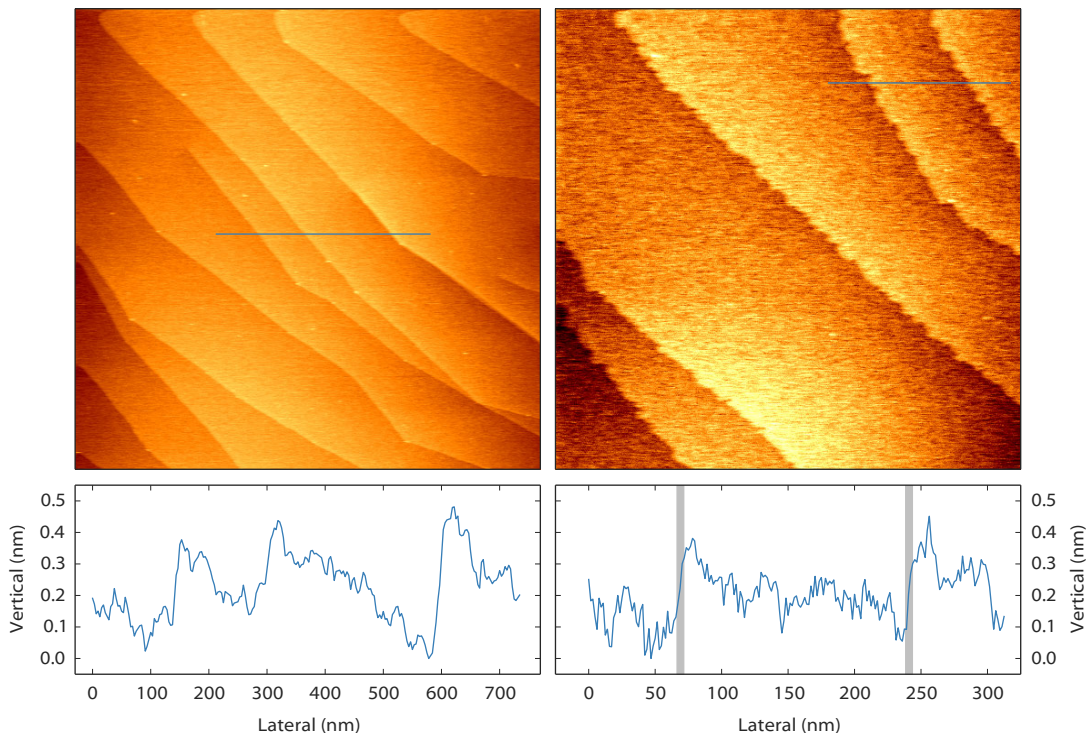
Figure 2.4. Mono-atomic steps on a Ag(111) single crystal at room temperature. No post processing has been performed except for line-by-line background subtraction. Left panels, in UHV, image size $1.6 \times 1.6\,\mu m^2$, frequency shift +18 Hz, 1.0 nm oscillation amplitude, acquisition time 524 s. Right panels, in a flow of $2\,ml_n/min$ of 120 mbar ethylene gas with sulfur impurities, image size $800 \times 800\,nm^2$, frequency shift +21 Hz, oscillation amplitude 1.0 nm, acquisition time 262 s. Under these conditions, the surface shows roughening of the steps, and structures with sub-ångstrom height on the terraces. To estimate the lateral resolution, the broadening of atomic steps has been measured and was typically 5 nm, the grey lines in the height profile mark this width (the lateral resolution in the left panels was limited by the scan speed).
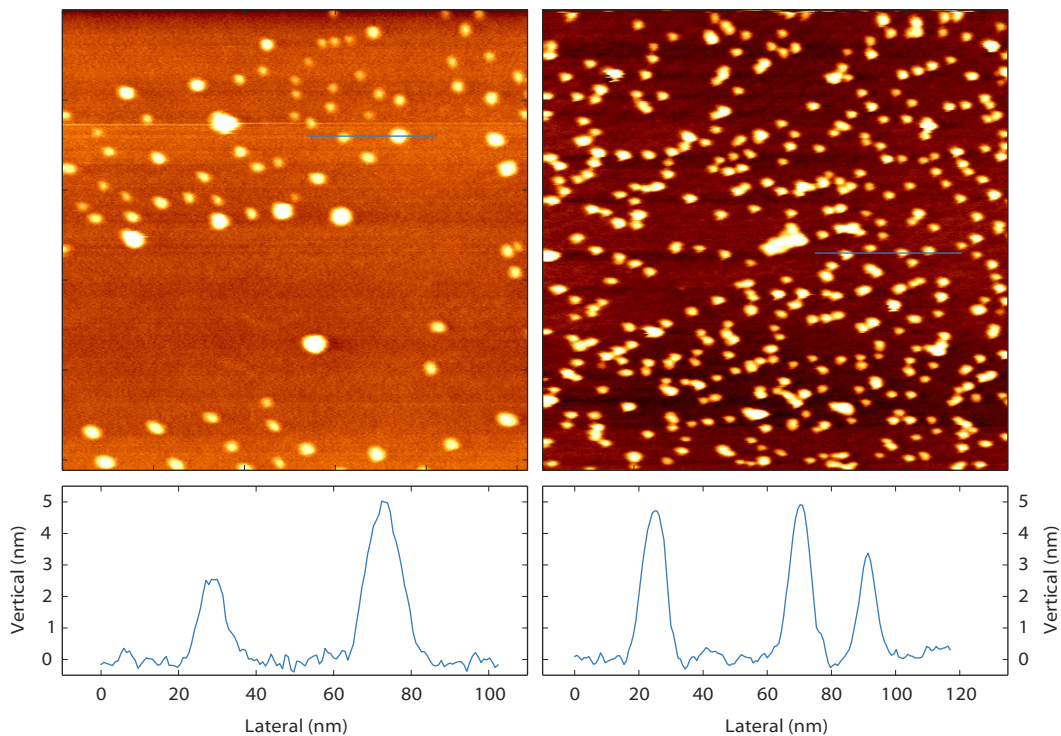
Figure 2.5. Palladium nanoparticles on $\alpha-Al_2O_3$, image size $700 \times 700\ nm^2$, frequency shift setpoint +5 Hz, oscillation amplitude 5 nm, acquisition time 131 s per frame. No post processing has been performed except for planar background subtraction. Left panels, 425 K, 1 bar 1:1:20 Ar:CO:O_2 mixture, total flow 5.5 ml$_n$/min. Right panels, 475 K, 1 bar 10:1:30 Ar:CO:O_2 mixture, total flow 4.1 ml$_n$/min.
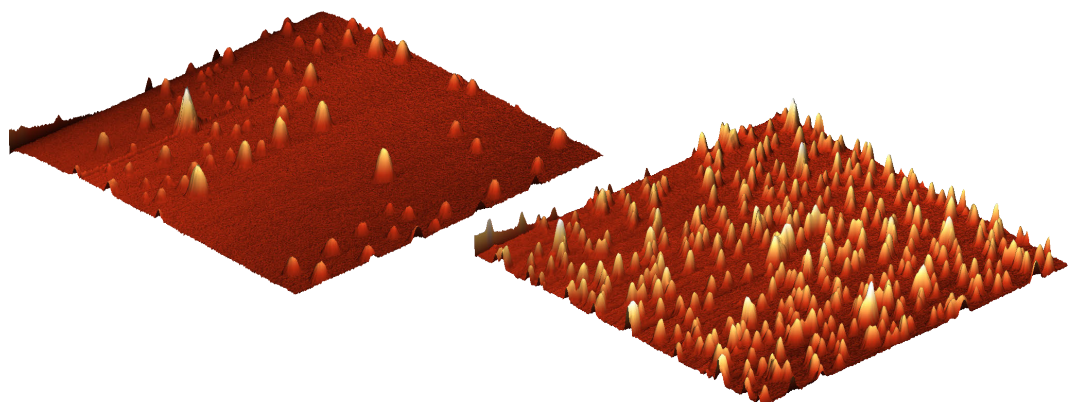
Figure 2.6. A three-dimensional view of the images in figure 2.5.

problem with AFM[41] — these images directly give unique information on the particle morphology and size distribution under catalytic conditions.

2.4.2 Influence of environment on QTF

Quartz resonators can be employed to measure temperature and several fluid properties (density, viscosity and derived quantities)[42, 43]. These sensor applications use the resonance frequency or the damping of the oscillator to detect changes in the environment. Unfortunately, the same parameters are used to perform the height feedback in a NC-AFM configuration. Since the "parasitic" influences of the environment can be dominant over the effects "of interest" of the tip-sample interaction, a brief discussion is in place on the influence of the gas environment and the temperature.

The density and viscosity of the surrounding fluid influence the damping of the QTF, but this is easily compensated for by the amplitude feedback, and at high Q it only results in a small change in resonance frequency. More problematic is that the fluid adds to the effective mass of the resonator[43], thereby further affecting the resonance frequency. For the *ReactorAFM*, filling the reactor with 1000 mbar argon starting from low vacuum (< 10 mbar) leads to a frequency shift of -50 Hz and a drop in Q-factor from $1 \cdot 10^4$ to $3 \cdot 10^3$.

When using mixtures of gases such as oxygen, carbon monoxide, nitric oxide, carbon dioxide, nitrogen and argon, only limited total pressure variations can be tolerated because of these gas effects on resonance frequency and damping, but partial pressures can be changed freely since the fluid properties of these gases are sufficiently similar. However, when using mixtures of light gases such as hydrogen or helium together with a heavy gas, care needs to be taken not to change the total density and viscosity too much while scanning. This can be achieved by adjusting the total pressure or by compensation of the mixture by adding an appropriate amount of a heavy inert gas such as argon or xenon. In addition, the resonance frequency of the QTF is sensitive to temperature. This derives from the anisotropic thermal expansion of the crystal lattice. Since our particular QTF is designed as a reference oscillator and not as a temperature sensor, the orientation of the lattice is optimised for frequency stability at its standard operating temperature, 25°C. However, in the *ReactorAFM* the sample can be heated to 600 K, and even though the QTF will not reach this temperature, it will have an effect on the resonance frequency. In this case, the resonance frequency typically shifts by 150 Hz when heating from RT to 423 K in 120 mbar argon in the first 45 minutes, during which scanning should be avoided, followed by a continuous drifting of 30 Hz per hour, which is attributed to the long-term thermalization of the scanner. While scanning, it is convenient to operate the sample heater at constant power (i.e. without temperature feedback) to keep the drift (both spatial and resonance frequency) monotonous.

A further complication can be introduced by combined effects of the fluid properties with temperature: changing the gas mixture changes the thermal conductivity of the gas in the reactor and this results in a change of temperature of the QTF. Additionally, the viscosity of a fluid is strongly dependent on temperature, and this in turn influences the damping. These effects however are minimised using the precautions mentioned here.

2.5   Conclusion and outlook

The *ReactorAFM* combines a UHV system with a high-pressure reactor and allows in-situ investigations of model catalysts. The scanner uses a miniature quartz tuning fork with a micrometre-sized tip, operates in non-contact mode and fits in the 0.5 ml reactor. Nanometre resolution is demonstrated under high-temperature, high-pressure conditions on a sample of supported metal nanoparticles. This instrument establishes an essential step to bridge the *pressure gap* and *materials gap*.

The sharpness of the EBID tip is currently the limiting factor for the lateral resolution of the instrument. Tests with a micromanipulator are in progress to attach various prefabricated tips to the QTF, e.g. an etched metal wire (as commonly used in STM and NC-AFM) or a tip from a standard AFM silicon cantilever. Another development in progress is the modification of the *ReactorAFM* to enable NC-AFM with simultaneous tunneling current measurements (STM), by adding a separate electric path to the tip. In addition, preliminary experiments have been performed with a version that fits onto the high-pressure flow reactor for surface X-ray diffraction (SXRD) and grazing incidence small angle X-ray scattering (GISAXS) developed by Van Rijn et al.[22]. This instrument will allow higher operating temperatures and it opens the way towards the direct correlation of real-space observations with reciprocal-space measurements.
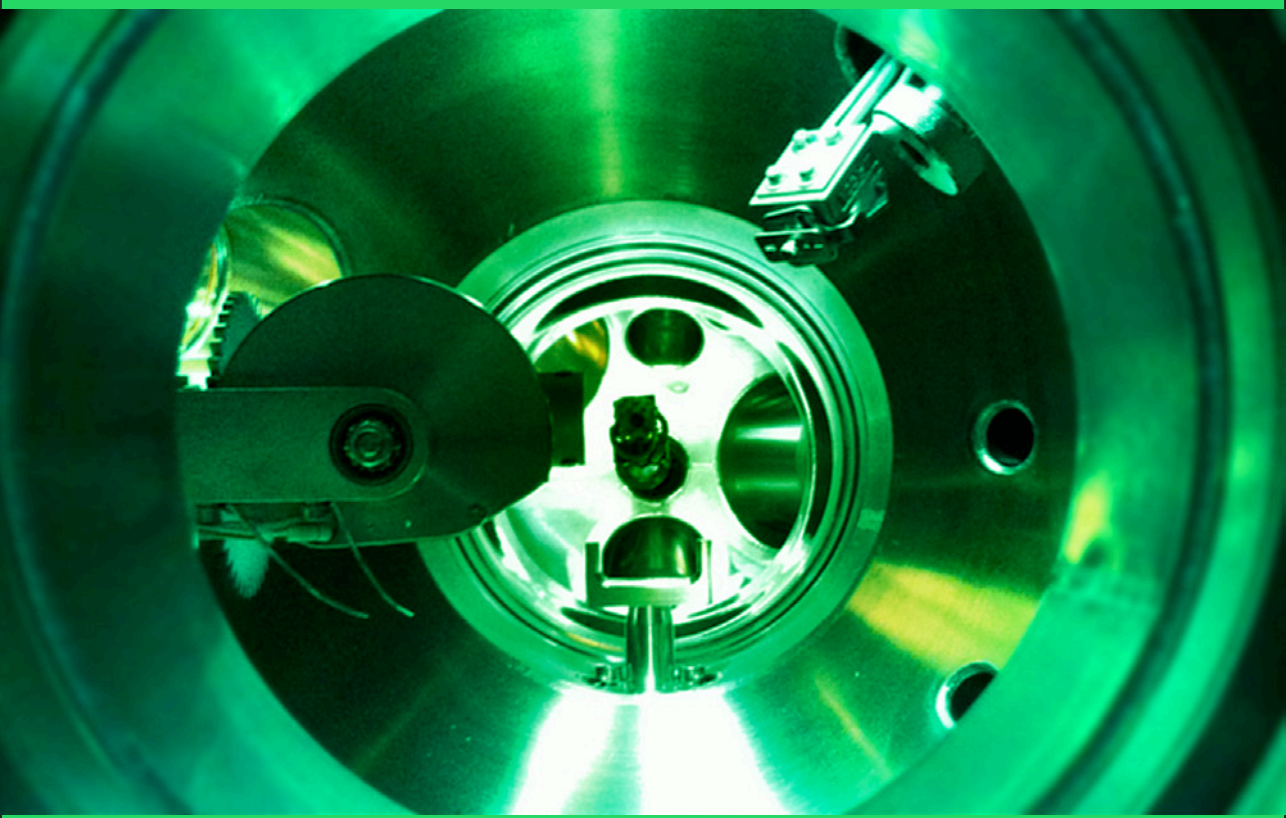
Chapter 3

Spacetime: analysis software for microscopy data of dynamical processes

With the continuing advancement of imaging techniques along the whole spectrum of photon-, electron-, ion- and scanning probe microscopes, it has become increasingly common to apply such techniques for real-time, *in-situ* studies of dynamical systems. When analysing data from such experiments it is essential to correlate the images to parameters that have been changing during the experiment, either spontaneously or intentionally. *Spacetime* is open source software to aid in this analysis by providing a single, unified view on heterogeneous datasets from *in-situ* microscopy studies.

3.1   Introduction

Some 400 years after the invention of the first microscope[44], the field of microscopy is still expanding and evolving. A recent development is the application of (sub)nanometre-resolution electron- and scanning probe microscopes for *in-situ* investigations of dynamical systems, that used to be limited to static ex-situ microscopy investigations or macroscopic measurements on large ensembles. These microscopy studies usually involve one or more global parameters that are varied or measured while the microscope is used to image a very small, local region of the specimen, in order to unravel structure-function relationships.

Examples are catalytic studies using a scanning tunneling microscope (STM) and atomic force microscopy (AFM) inside a flow reactor[11, 45, 46], or using micromachined nanoreactors in transmission electron microscopy (TEM)[23] or scanning X-ray microscopy[47]. In the field of materials science, *in-situ* TEM studies have been published on the hydrogenation of palladium[48] and electromigration in platinum electrodes[49]. In addition there are electrochemistry studies involving STM during deposition[50, 51].

The power of these studies lies in the correlation of the spatial microscopy data with the external parameters that either influence the system or are influenced by it. In a typical laboratory environment these external parameters are recorded from a variety of sources by specialised hardware or software. With the increasing complexity of such experiments, it becomes a non-trivial task to present this heterogeneous dataset, consisting of several different data types and file formats, together for analysis. For this purpose, dedicated software has been developed called *Spacetime*.

3.2   Features

Spacetime aims to give a unified view on the spatial microscopy data together with any time-dependent parameter related to the dynamics of the system under investigation. It supports highly heterogeneous datasets, both in character (e.g. spatial data acquired in a single shot, spatial data acquired by a scanning technique, or purely time-dependent data) and in data format (ranging from standard image formats and plain text files to several vendor-specific formats or extensions). The emphasis is on browsing through datasets and searching for correlations to identify which subsets need to be analyzed using conventional image- or data analysis software. If desired, *Spacetime* exports the originally heterogeneous dataset into a simple homogeneous format for analysis with other tools.

Spacetime has a modular design and uses a separate module for each supported data format. The user typically selects two or more modules, and configures each of
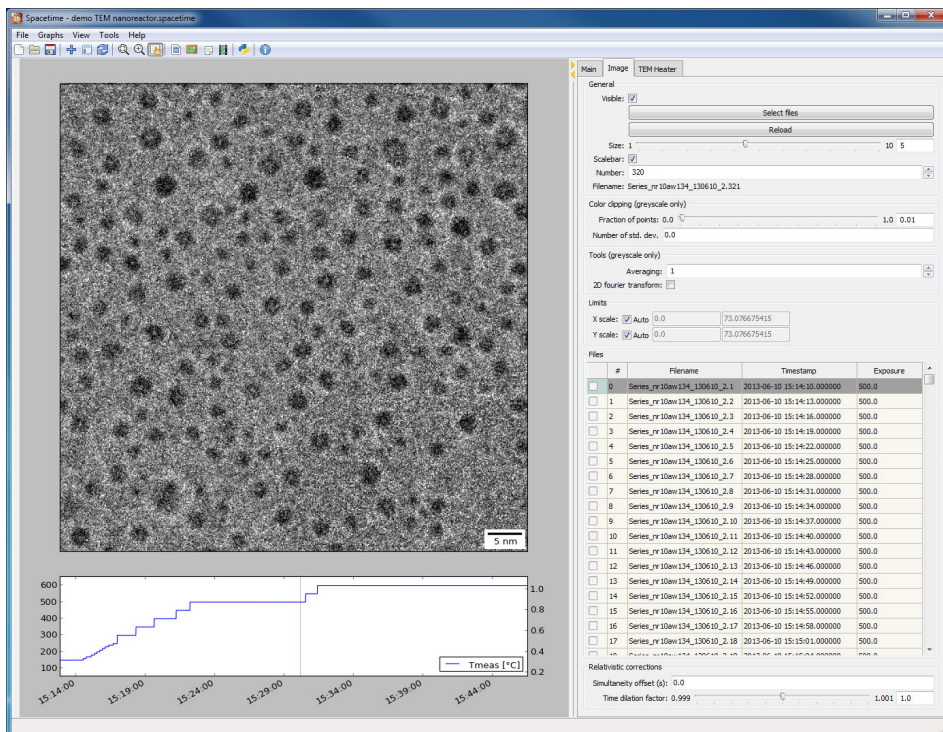
Figure 3.1. An *in-situ* Transmission Electron Microscopy (TEM) experiment with screenshots from *Spacetime*. The left part of the window shows the experimental data, the right panel allows detailed control over the display. Pt nanoparticles have been heated in a 1 bar H_2 atmosphere in a TEM nanoreactor[23]. The lower panel shows a trace of the sample temperature as a function of time and the vertical line indicates the point in time at which the image was acquired. The grey band in these panels indicates the time window during which the image was measured.

them by selecting the data files and possibly defining other settings. Each module has a specific way of presenting its data. Time-dependent quantities can be plotted in graphs, showing the values versus time, while microscopy images are displayed together with a marker indicating the acquisition time and duration. The modules share a single time axis, which can be presented as an absolute date and time, or in the form of the time relative to a user-defined time origin. If needed, the timing of individual modules can be adjusted to correct for improperly synchronised clocks or propagation delays of a physical observable. The precision of the time axis is as good as 10 μs, even though many data formats have a time resolution of only 1 s.

Combined data can be exported to various raster and vector image formats, and can be animated and saved as a movie. For presentation purposes *Spacetime* features a split-screen presentation mode, where the projector shows the selected combination of experimental data while the control interface remains on the computer/laptop screen.

3.3   Implementation

Spacetime has been written in Python, a general-purpose programming language that is becoming increasingly popular in the scientific community[52]. *Spacetime* uses various open-source libraries, including NumPy[53] (numerical computation), Matplotlib[54] (plotting) and the Enthought TraitsUI toolkit[55] (graphical user interface or GUI). This makes *Spacetime* fully platform-independent so that it runs on e.g. Windows, Linux and Mac OS X.

The code is modular and easily extensible. The description of the GUI, the plotting logic and the data handling code is fully separated for each of the supported file formats. This means that when adding a new file format, only the actual file handling code has to be written, the plotting code, and GUI can be reused from other modules. Similarly, there can be multiple different graph types for a single file format.

At the time of this writing, the following file formats are supported: basic image formats (including PNG, JPEG, TIFF and BMP), basic plain text formats (CSV and tabulated), Leiden Probe Microscopy[56] Camera RAW files for scanning probe microscopy, Gatan DigitalMicrograph 3[57] (DM3) images and stacks for transmission electron microscopy, TVIPS[58] extensions for TIFF images for transmission electron microscopy, and various mass spectrometer formats from Pfeiffer Vacuum[59], Stanford Research Systems[60] and MKS Instruments[61].

Figures 3.1 and 3.2 show two screenshots taken from *Spacetime* demonstrating its flexibility.
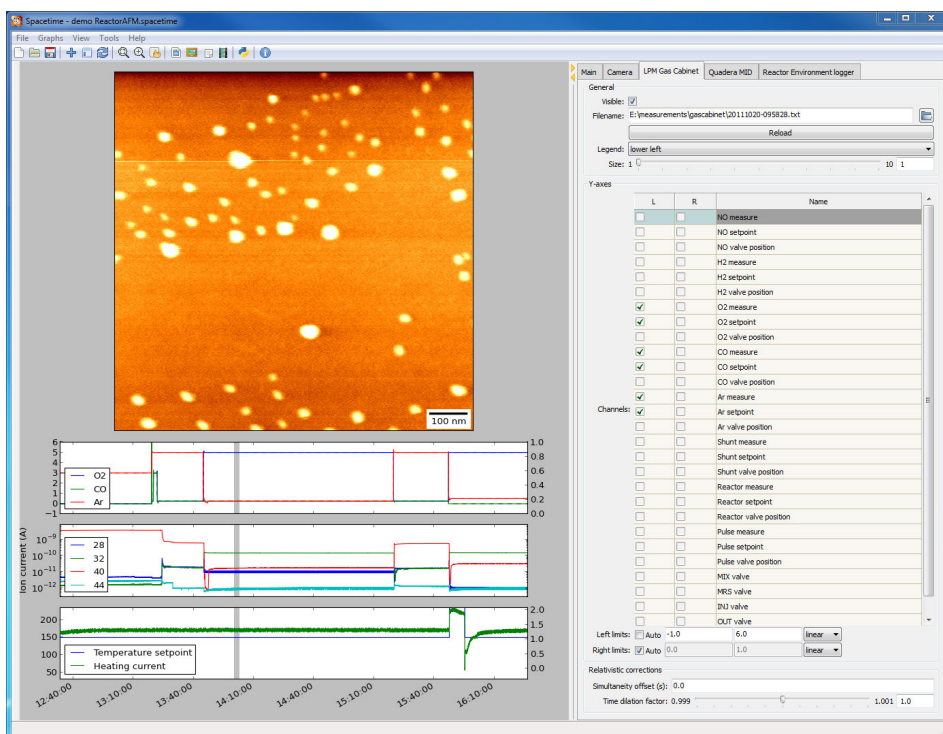
Figure 3.2. Another screenshot from *Spacetime*: Pd nanoparticles on α-Al$_2$O$_3$ during an *in-situ* catalysis experiment on the reaction $CO + \frac{1}{2}O_2 \longrightarrow CO_2$, with a high-pressure high-temperature non-contact atomic force microscope (AFM) (chapter 2). The three panels below the AFM image correspond to: gas flow into reactor, mass spectrometry analysis of reaction products, sample heating. The grey band in these panels indicates the time window during which the image was measured.

3.4 Outlook

Spacetime is a flexible tool for exploring the heterogeneous datasets typically acquired during microscopy studies of dynamical processes, but can be used with any dataset combining two-dimensional images with time-dependent data. Future plans include arbitrary transformations of the time-axis using mathematical expressions or measurement data and expanding the number of supported file formats. *Spacetime* is available for download[62] as open source, free software under the terms of the GNU General Public License[63].
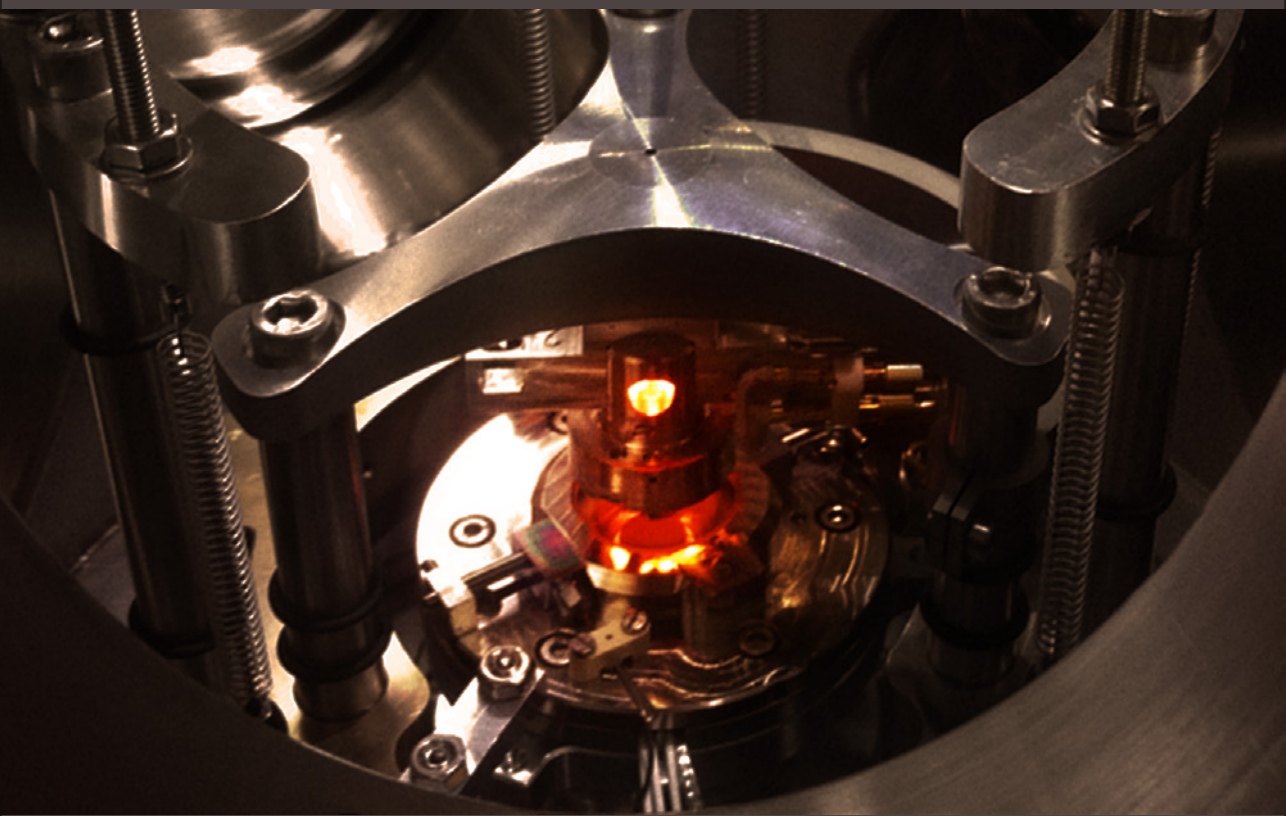
Chapter 4

BINoculars: data reduction and analysis software for two-dimensional detectors in surface X-ray diffraction

BINoculars is a tool for data reduction and analysis of large sets of surface diffraction data that have been acquired with a 2D X-ray detector. The intensity of each pixel of a 2D-detector is projected onto a 3-dimensional grid in reciprocal lattice coordinates using a binning algorithm. This allows for fast acquisition and processing of high-resolution datasets and results in a significant reduction of the size of the dataset. The subsequent analysis then proceeds in reciprocal space. It has evolved from the specific needs of the ID03 beamline at the ESRF, but it has a modular design and can be easily adjusted and extended to work with data from other beamlines or from other measurement techniques. This chapter covers the design and the underlying methods employed in this software package and explains how *BINoculars* can be used to improve the workflow of surface X-ray diffraction measurements and analysis.

The work presented in this chapter has been performed together with Willem Onderwaater.

4.1   Introduction

Over the last decade there have been several developments that have radically changed data acquisition in X-Ray Diffraction (XRD) experiments. The primary development is that nearly all point detectors have been replaced by 2D-detectors, such as the MAXIPIX detector[64], that collect spatially resolved information from a region in reciprocal space in a single shot. Secondly, by synchronising the data acquisition with the actuation of the diffractometer motors, it is now possible to perform continuous scans during diffractometer movements. Even though this has been demonstrated already 50 years ago[65], it has only recently become routine practice[66]. Thirdly, the high photon flux at 3rd generation synchrotrons[67] allows integration times in the order of tens of milliseconds rather than seconds, thus enabling time-dependent observations of dynamic processes rather than the slow acquisition of static information.

The result of these developments is that the data acquisition rate has increased by six to seven orders of magnitude, from typically 1 point per second to millions of points per second, so the amount of data collected during one experiment increased dramatically. Today's computer hardware can keep up with that increased demand, but the development of software to analyze these large datasets has been lagging behind, which has kept most users from exploiting the full potential of modern surface diffraction beamlines. *BINoculars* aims to fill this gap by taking a novel approach to data reduction in Surface X-Ray Diffraction (SXRD) experiments.

Currently, data reduction is typically performed by integrating a region of the image from a 2D-detector, sometimes coupled with another integration to determine the background level, and then basically treating the data as if it would have come from a point detector. Compared to a traditional point detector the advantages are mostly qualitative: the large acceptance angle of the detector, in combination with its good angular resolution, is very convenient during diffractometer and sample alignment, and makes it possible to visually identify peaks by their shape (i.e. one can easily distinguish between a powder ring, a crystal truncation rod or a region of diffuse background). *BINoculars* improves on this by treating every pixel of a 2D-detector individually, rather than to reduce the 2D-detector to an expensive point detector.

BINoculars takes a series of images from a 2D-detector, calculates for each pixel the corresponding reciprocal lattice coordinates $(h\,k\,l)$, and reduces the image collection to a single dataset by averaging the intensities of pixels taken at identical $(h\,k\,l)$ positions (within a user-specified resolution). This transformation and averaging is illustrated in figure 4.1. To allow online analysis during data acquisition, *BINoculars* can run on a high performance cluster to process large datasets. For example, the result of a full hour of continuous scanning, adding up to a total of approximately 10^{10} pixels, can be processed in a matter of minutes. In addition,
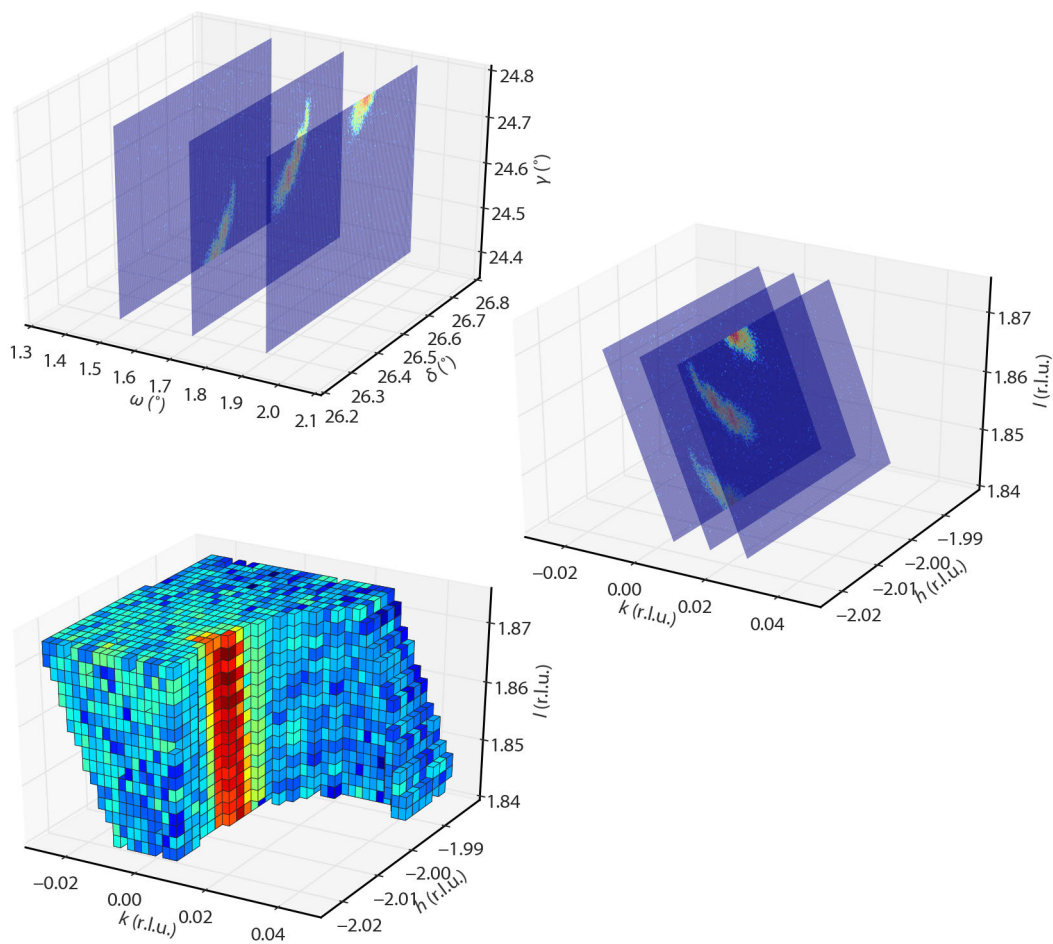
Figure 4.1. A graphical overview of the process performed by *BINoculars*. The data displayed here are a rocking scan through $(h, k, l) = (-2, 0, 1.85)$ the diffraction pattern from a Pt(110) surface. Upper panel, raw data acquired by the 2D-detector with the corresponding angles ω, δ, γ from a six-circle diffractometer[68]. Middle panel, the diffractometer angles are mapped onto reciprocal space coordinates $(h\,k\,l)$. Lower panel, the averaged intensity of pixels on a regular grid of volumetric bins (voxels) is calculated. Part of the bins are removed for clarity. Note that the data in reciprocal space in the lower panel are constructed from a series of images over a larger range and with a denser sampling in ω than shown in the other panels.

BINoculars provides tools to further process the data, including visualisation, curve fitting, and crystal truncation rod integration. The latter can be seen as an implementation of the reciprocal-space integration method, recently described by Drnec et al[69]. As a whole, *BINoculars* can be seen as a N-dimensional generalisation of PyFAI[70] and xrayutilities[71], optimised for (but not limited to) surface X-ray diffraction.

4.2   Implementation

BINoculars has been written in Python, an open source scripting language that is very suitable for scientific software, thanks to its powerful and clear syntax and the extensive support for numerical calculations via the Numpy and Scipy libraries[52].

   BINoculars has been designed to process large datasets, and its operation is usually cpu-bound. An ordinary desktop computer can easily take many hours to deal with a dataset obtained in one hour (e.g. 10^{10} pixels with 16 bit per pixel). To allow online analysis during data acquisition at a beamline, *BINoculars* can use a computing cluster to distribute the load over multiple computers.

   To keep *BINoculars* modular and flexible, the workflow for processing data is separated into four modules: the *dispatcher* is in charge of the whole process and handles job parallelization and distribution, the *input* class gathers the experimental data, and the *projection* class converts the raw data into the coordinates of choice. Finally, the processed data is binned on a discrete grid and stored in a *space* class, which provides generic tools for further analysis. The specific behaviour of the *dispatcher*, *input* and *projection* modules can be changed independently. For these modules, the user can choose from several different implementations, each having a different set of features.

   The *input* class collects the raw 2D-detector images and assigns metadata to each individual pixel. This metadata is used later on by the *projection* class to make the conversion to the desired coordinate system (e.g. $(h\,k\,l)$ for a typical SXRD experiment). The *input* class is specific to a certain experimental setup. As an example, for the ID03 beamline at the ESRF[72], a separate class has been written for each of the experimental hutches. In many ways the two experimental hutches are identical, for example the same numbering scheme is used for the images taken by the X-ray cameras, but one of the diffractometers operates at constant detector-sample distance while the other does not. The *input* class takes care of all these technicalities, and writing a new *input* is the most important task when adding support for another experimental setup. In addition, the work done by the *input* class is often the most computationally intensive step in the entire process of *BINoculars*.

   The next step is performed by the *projection* class, which converts the data collected by an *input* class into the appropriate coordinate system for binning. For
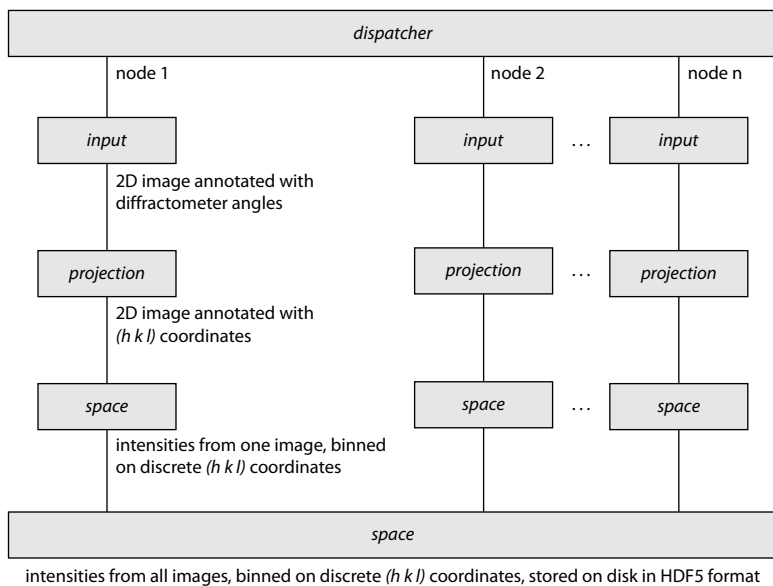
Figure 4.2. Block diagram of the process performed by *BINoculars* for a typical dataset from a diffraction experiment. The *dispatcher* distributes the load over multiple nodes from a computing cluster. The *input* class gathers the experimental data and calculates the diffractometer angles for each pixel. The *projection* class converts the angles to $(h\,k\,l)$ coordinates. The intensities are binned on a discrete grid by the *space* class, and finally the intermediate results from each node are combined into a single *space*.

an SXRD experiment, the *input* class will typically return a series of detector images with corresponding diffractometer angles for each pixel, and the *projection* class will convert the angles into reciprocal space coordinates $(h\,k\,l)$ for each image. In some cases, there are several projections that are useful. For example, for the ID03 beamline it is sometimes necessary to project onto the scattering angle 2θ rather than $(h\,k\,l)$ coordinates (although an alternative route would be to perform a coordinate transformation afterwards to convert the $(h\,k\,l)$ *space* into a 2θ *space*).

Once the data has been gathered and projected on the desired coordinate system, the binning operation is performed by a class called *space*. This class represents an *n*-dimensional regular grid: it is a discrete subset of a vector space, where each dimension has a fixed step size. Many mathematical operations can be performed with *spaces*, including addition, subtraction, slicing, projections, and coordinate transformations. To bin an image, the $(h\,k\,l)$ coordinates of each pixel of the image are mapped onto the nearest discrete *space* grid location. Then the pixel intensities are accumulated at every discrete grid location, using the histogram-operation *bincount* from Numpy. In addition, the number of contributions per coordinate is stored in order to calculate the mean intensity per bin rather than the integrated intensity. This binning operation is the essential data reduction step performed by *BINoculars*, hence the name of the program.

The *dispatcher* orchestrates the entire process: it asks *input* for the sequence of images from the 2D-detector, delegates it to the appropriate *projection* and performs the binning operation by feeding the projection result into a *space*. Two *dispatcher* implementations are currently present: one for local processing using multiple processor cores on a single computer, and one that distributes tasks over a high performance cluster managed using OAR[73]. Support for other types of clusters can easily be added. When running on a computing cluster, the *dispatcher* gathers all intermediate spaces calculated by the individual nodes (for example using a shared filesystem) and they are added together to form the final resulting *space*. *Spaces* are stored on disk using the HDF5 file format[74].

After a *space* has been created, the size of the dataset has typically been reduced by a factor 10 to 100, and further analysis can usually be performed on a standard workstation. However, loading a high-resolution large-area 3D dataset can require several GB of memory, and for some operations it is required to have several copies in memory. If this is a problem, it is also possible to work with a subset of the data, either by selecting a smaller region, or by reducing the resolution, or by reducing the dimensionality.

BINoculars provides various tools for analysis, including mathematical operations, plotting and exporting. For ultimate flexibility it is possible to directly manipulate a *BINoculars* space from a Python script, but in many cases the standard tools are sufficient. In addition, a fitting and integration tool is available to calculate

the structure factors of a crystal truncation rod to be directly inserted into the fitting program ROD[75]. It takes as input a reciprocal mesh which it slices by a user-specified resolution and the resulting data are either fitted (typically with a 2D lorentzian) using a least-squares optimization, or simply integrated. The error is estimated from equation (4.2), as will be described in more detail in the next section.

4.3   Binning and error handling

BINoculars calculates the average intensity of multiple contributions, originating from different pixels and/or detector positions, to a single reciprocal space bin. This operation is similar but not identical to averaging a series of repeated measurements taken by a point detector at a fixed position. This section discusses the implications of the binning operation for the background intensity and the estimation of statistical errors.

When using a point detector, the typical surface diffraction experiment is set up such that there is a unique detector position for each set of reciprocal space coordinates $(h\,k\,l)$. In practice, this means reducing the degrees of freedom of the diffractometer to three, e.g. by working with a constant surface normal and a fixed angle of incidence. When taking series of repeated observations at a certain reciprocal-space location, the systematic error in each measurement can be assumed to be constant (after the usual correction for variations in the total beam intensity), and the only variation is given by the shot noise of the incoming photons.

Using a 2D-detector, the spatial extent of the detector introduces two more degrees of freedom, meaning there is no longer a unique detector position for a given reciprocal space coordinate. This is usually solved by selecting one pixel of the detector to correspond with "the detector position", and ignoring the fact that the other pixels are at a slightly different position. However, *BINoculars* does take the spatial extent of the detector into account, and calculates the average intensity at each location in reciprocal space, regardless of the detector position.

This means that multiple measurements, even when spaced closely together in time, exhibit variations not only due to the statistical nature of the process, but also due to a systematic error possibly resulting from different detector positions. This error is caused by differences in background originating from scatterers other than the sample, as is illustrated in figure 4.3. Flight tubes and slits between the sample and the detector can be used to reduce this background, but they also decrease the aperture of the 2D-detector. This reduces the range of $(h\,k\,l)$-locations over which data can be collected in one acquisition. This means that a careful trade-off needs to be made between acquisition speed and background suppression.

In some cases it is possible to subtract the background I_b, either by measuring
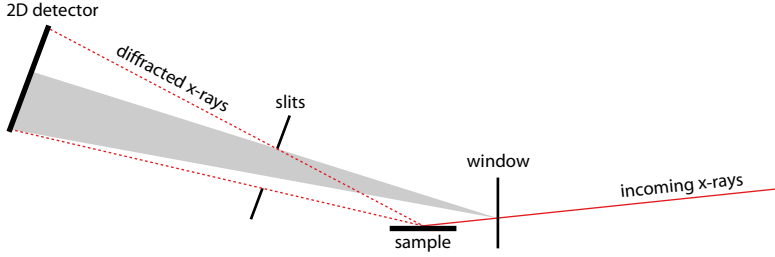
Figure 4.3. The wide opening angle of the slits, which is required to capture a region in reciprocal space with a 2D-detector, results in a non-uniform background across the detector (indicated in grey in the figure). This background originates from scatterers other than the sample, for example a beryllium window. This means that when taking two images at slightly different detector positions such that there is some overlap between the two captured regions, the background intensity in the overlapping region is not constant.

it directly when the sample is not in the beam, or by estimating it from the dataset itself in regions in reciprocal space where the sample only weakly contributes to the total observed intensity. The latter approach will be explored in more detail in section 4.4.

The remaining error reflects the counting statistics in the number of detected photons and is typically assumed to obey Poisson statistics[76]. For a single observation of I counts, the standard deviation σ is estimated using $\sigma = \sqrt{I}$. With N independent observations I_i in a single bin, each with its own $\sigma_i = \sqrt{I_i}$, the average intensity is

$$I = \frac{1}{N} \sum_i I_i, \tag{4.1}$$

and the variance can be estimated under the assumption of normality (N or I_i sufficiently large) using

$$\sigma^2 \approx \frac{1}{N^2} \left(\sum_i \sigma_i^2 \right) = \frac{I}{N}. \tag{4.2}$$

Assuming we have a separate estimate of the background intensity I_b in this bin with a corresponding variance σ_b^2, the the variance σ_s^2 of the signal $I_s = I - I_b$ is now given by

$$\sigma_s^2 = I/N + \sigma_b^2. \tag{4.3}$$

Of course, if the background was also obtained by averaging N measurements, σ_b^2 would also take the form I_b/N.

4.4   Demonstration

Four different examples will be discussed to show the capabilities and limitations of *BINoculars*.

Figure 4.4 shows a high-resolution (0.0002 reciprocal lattice units or r.l.u.), large-area (hk)-surface in reciprocal space, covering the first reciprocal unit cell of a Au(111) surface, submerged in an electrochemical cell filled with sulphate containing electrolyte (pH 7) and kept at -800 mV vs. Ag/AgCl reference electrode. The gold surface exhibited the so-called herringbone reconstruction[77], which is a regular structure with a ($22 \times \sqrt{3}$ periodicity) that is organised into a zigzag pattern on an even larger scale. The ($22 \times \sqrt{3}$) superstructure peaks originating from this reconstruction[78, 79] are well-resolved in the scan. The differences between this diffraction pattern and the pattern reported in literature for the same surface in ultrahigh vacuum are not fully understood, however it is likely due to the sample preparation procedure in the electrochemical cell. The dataset was acquired in just 111 minutes.

Figure 4.5 shows a dataset that is strongly affected by background intensity. Like figure 4.4, the dataset is built up from a series of ω-scans and in this case those scans are clearly visible as arcs after processing by *BINoculars*. The problem is that the background intensity not only depends on the position of a pixel, but also on the position of the camera. In other words, when moving the camera by only a small amount, such that a certain feature remains in the field of view (in this case a move in γ between the consecutive ω-arcs), the contribution of the background intensity to that feature can change significantly, as illustrated in figure 4.3.

This particular dataset has been obtained using the high-pressure flow reactor setup at ID03[22], which has a beryllium dome around the sample. The dome acts as a strong X-ray scatterer only 14 mm away from the sample. It is not possible to lower the resulting background intensity using slits without dramatically reducing the aperture of the detector. However, for this sample it proved possible to estimate and subtract the background level, the result of which is shown in the middle panel of figure 4.5. For each pixel of the detector, the background was estimated as the average intensity of that pixel in all images in a single ω-scan. The average is calculated by fitting a Poisson distribution, as this turned out to give better rejection of outliers (which are in fact the diffraction peaks) than a simple mean or median calculation. This process was then repeated for each ω-scan, resulting in an estimate of the background intensity that was subtracted from the raw data.

The background subtraction procedure described here is not generally applicable as powder rings are treated as background. In addition, the amount of background is strongly dependent on the experimental setup, and the other datasets shown here did not need any background correction. Therefore this procedure is currently not part of *BINoculars*, although it is likely to become part of the ID03-specific *input*
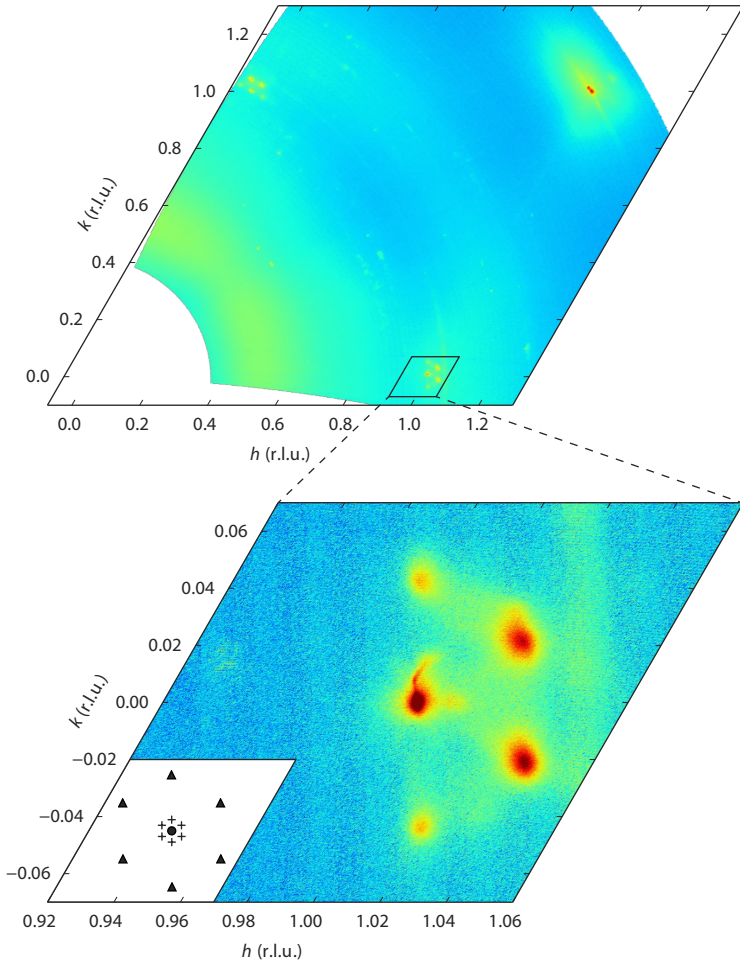
Figure 4.4. A large-area survey (upper panel) in reciprocal space of the herringbone reconstructed Au(111) surface, taken at l = 0.3. The dataset has been obtained in 111 minutes using a series of continuous-acquisition ω-scans. A zoom-in (lower panel) around the $[1\,0\,l]$ crystal truncation rod (indicated by the circle in the inset) shows the satellite peaks caused by the $22 \times \sqrt{3}$ unit cell (indicated by triangles), and those originating from the longer range ordering of the zigzag domains (indicated by crosses). Loading this dataset requires 1 GB of memory.
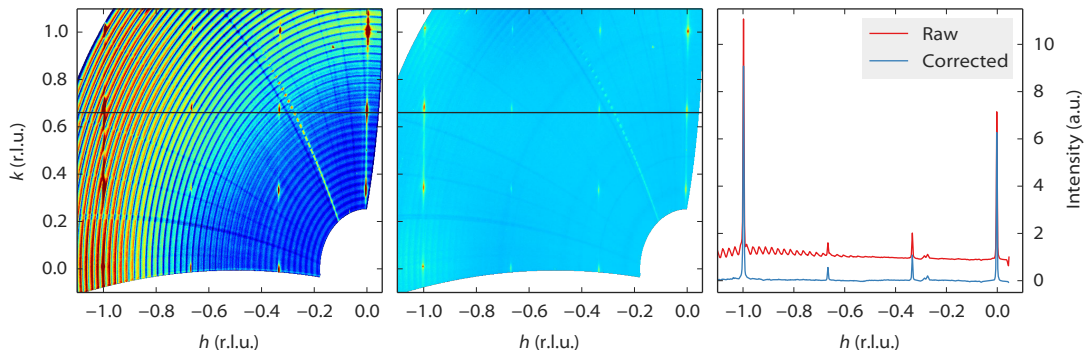
Figure 4.5. Some datasets require further processing to remove the curved background artefacts. This figure shows the $l = 0.5$ plane from a Pt(110) sample in the high-pressure flow reactor setup at ID03. The surface exhibited a (3×3) reconstruction (which has not been described before in literature) during high-temperature, high-pressure exposure to NO and H_2. The setup had a relatively high diffuse background that could be corrected for by estimating the background level for each pixel of the detector, once per scan in ω. The left panel shows the raw data, the middle panel the data after background correction. The right panel shows the intensity profiles along the line $k = 0.66$ for a direct comparison between raw and corrected data. The small peaks at $h = 0.3$ originate from scattering from the Be dome, this is also visible in the left and middle panel as a diagonal line.

module in the near future.

The third example, figure 4.6, shows the output of the crystal truncation rod (CTR) fitting module. The original dataset is a single l-scan along the CTR. After processing by *BINoculars*, during which the *input* module also takes care of the polarization correction factor necessary to obtain the structure factors[68], the three-dimensional rod can be visualised in reciprocal space. The dataset is then segmented into small intervals along l. Each section is analysed separately by a numerical integration algorithm to calculate the structure factors as a function of l. This method has recently been described by Drnec and co-workers[69].

At lower l the detector is more perpendicular to the surface, and for some samples it might be useful to augment the l-scan with rocking scans at low l. *BINoculars* can easily deal with such a hybrid dataset, since it starts by processing the data into the three-dimensional rod, after which the integration procedure (taking place in reciprocal space) is performed completely independently of the original character of the raw data.

The fourth example demonstrates that BINoculars can be used with other coordinate systems than $(h\,k\,l)$. Figure 4.7 shows the reflected intensity from a $(PbSe)_{4+\delta}(TiSe_2)_4$ sample. It is constructed from images taken at different incidence angles that are projected onto $q_\parallel$ and q_z, the in-plane and out-of-plane momentum transfer. This two dimensional projection allows detailed analysis of

45
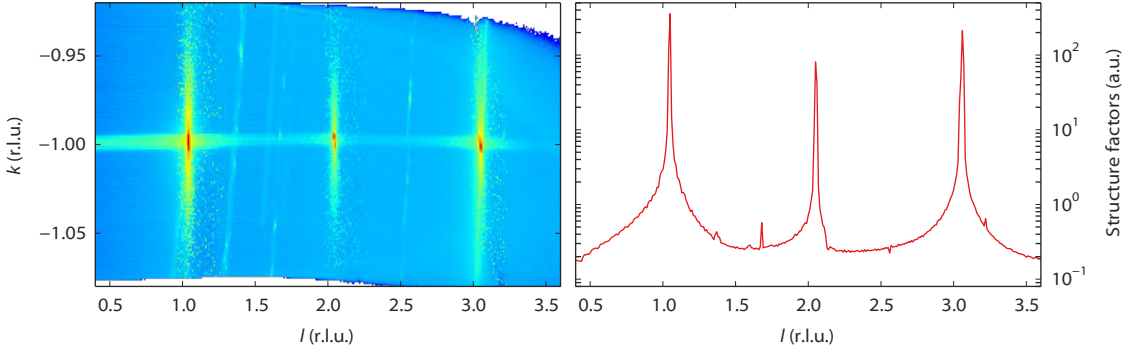
Figure 4.6. The left panel shows an l scan along the $[0\bar{1}l]$ crystal truncation rod of a SrTiO$_3$(100) surface[80] projected on the kl plane after processing by *BINoculars*. A series of 2D-Lorentzians has been fitted to slices at constant l (corresponding to small hk surfaces), which has resulted in the structure factors shown in the right panel.
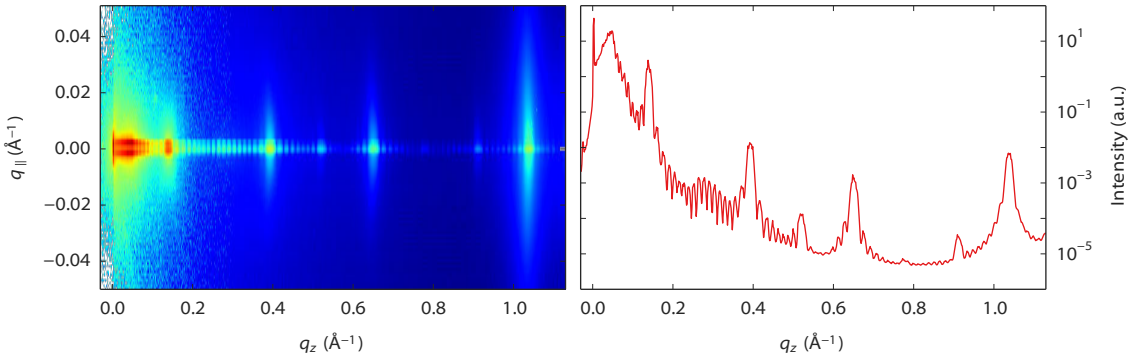
Figure 4.7. Reflectivity scan of $(PbSe)_{4+\delta}(TiSe_2)_4$, a telluride misfit layer compound[81]. This sample has a multilayer structure with well-defined out-of-plane stacking but rotational disorder between layers. This gives rise to oscillations in the reflectivity curve, combined with broad in-plane scattering. The left panel shows the projection of the images taken at different incident angles onto $q_\parallel$ and q_z. The right panels shows the specular rod obtained by integration along $q_\parallel$ from -0.005 to 0.005 Å^{-1}.

the in-plane X-ray scattering that cannot easily be obtained by conventional methods. In addition, the integration to obtain the specular rod ($q_\parallel = 0$) can be easily performed.

4.5   Conclusion

BINoculars brings SXRD into the 21st century by unlocking the full visual power of two-dimensional surface diffraction patterns, something that was previously only achievable with LEED in UHV conditions, or by increasing the X-ray energy and sacrificing k-space resolution and dynamic range[82], or by taking an impractical amount of time. In addition, *BINoculars* simplifies structure determination by providing a quick, easy, and accurate method to integrate crystal truncation rods.

BINoculars is open source under the terms of the GNU General Public License[63] and is available online[83].

Part II

High-pressure experiments
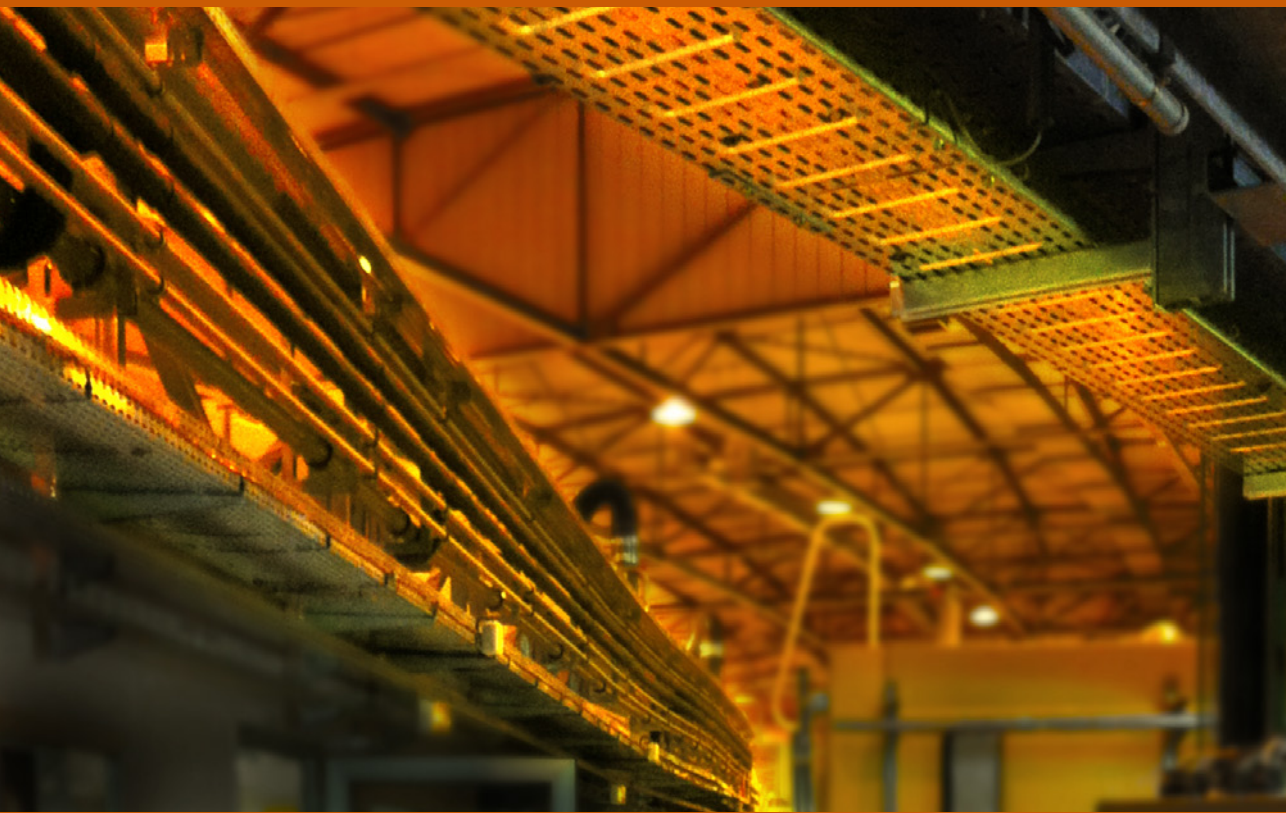
Chapter 5

NO reduction by H$_2$ over Pt(110) studied by SXRD

This chapter describes the results of a 144-hour measurement campaign at the ID03 beamline of the ESRF. It was devoted to an exploratory investigation of the surface structure of a Pt(110) single-crystal surface during high-pressure, high-temperature NO and H$_2$ exposure. Here, we report the two main observations, namely (i) the appearance of a wide variety of surface reconstructions, and (ii) extensive faceting of the surface. The precise conditions under which these effects occur will need to be investigated more systematically in future experiments.

5.1   Introduction

The catalytic conversion of nitrogen oxides (NO_x) is one of the three processes taking place on the three-way car catalyst[84, 85]. This chapter concerns the reaction between nitric oxide (NO) and H_2 over platinum, which is a model reaction for this process. In this case, the formation of nitrogen via

$$2\,NO + 2\,H_2 \longrightarrow N_2 + 2\,H_2O \qquad (5.1)$$

leads to the desired, non-toxic reaction products, however the selectivity for this reaction is very low on platinum[86]. Instead, the reactions that lead to the formation of ammonia (NH_3) and nitrous dioxide (N_2O) are dominant. For application as a car catalyst these products need to be avoided, and typically rhodium is added to aid the NO removal.

There have been many UHV studies on the $NO/H_2/Pt$ system. NO adsorbs molecularly on platinum surfaces with the nitrogen atom bound to the surface[87]. The (100) surface binds NO more strongly than the (111) and (110) surfaces, and is also more active for dissociation of the molecule[88]. On the (110) surface, NO lifts the missing-row reconstruction[87]. It preferentially sits on the bridge sites of the atom rows at low coverages and moves to the top sites at high coverages[89–91]. Hydrogen prefers the bridge sites on the (1×2) atomic rows and competes with CO adsorbed on the top sites[92]. When the Pt(100) surface is co-exposed to H_2 and NO, the quasi-hexagonal reconstruction of the clean surface is lifted, depending on the NO coverage[93]. In combination with the difference in turnover rate between the reconstructed and the non-reconstructed surface, this can give rise to kinetic oscillations under certain conditions[94, 95]. As for the high-pressure regime, we have not found any literature on high-pressure surface-science experiments on the reduction of NO by H_2 on Pt(110).

5.2   Methods

The experiment was performed at the ID03 beamline of the ESRF with 18 keV X-rays using the high-pressure Surface X-Ray Diffraction (SXRD) flow reactor[22]. This setup allows UHV sample preparation followed by in-situ high-pressure, high-temperature gas exposure, during SXRD or Grazing Incidence Small Angle X-ray Scattering (GISAXS) measurements simultaneous with reactivity measurements by a quadrupole mass spectrometer.

The Pt(110) sample was cleaned at the beginning of the experiment by repeated cycles of argon ion bombardment and annealing in UHV, resulting in a (1×3) missing-row[96] reconstructed surface, exposing narrow (111) facets (figure 5.1). The (1×3) structure was probably stabilised by carbon segregated from the bulk[97], which was not fully removed because the sample was not annealed in oxygen.
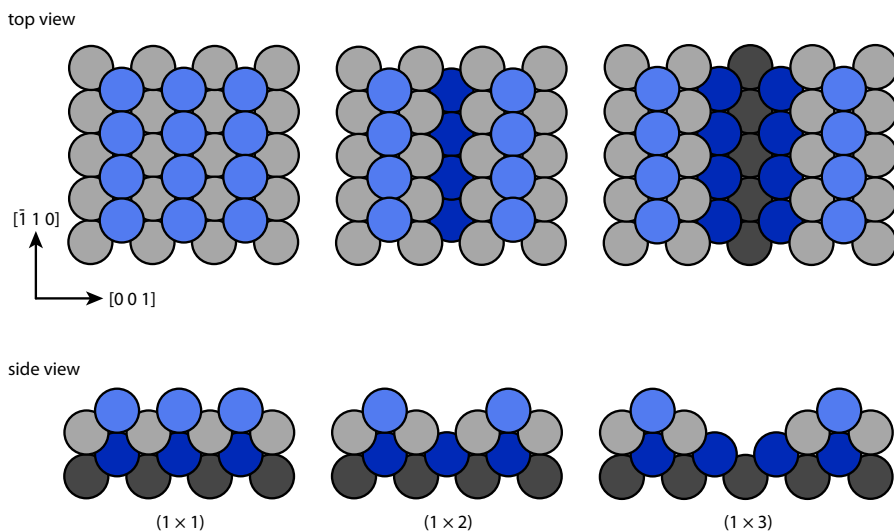
Figure 5.1. Ball models of the surface structure of Pt(110), without a reconstruction (left) and with the (1×2) and (1×3) missing-row reconstructions (middle and right)[96]. The h-axis of reciprocal space is chosen to correspond to the closed-packed $[\bar{1}10]$ direction and k to the open $[001]$ direction.
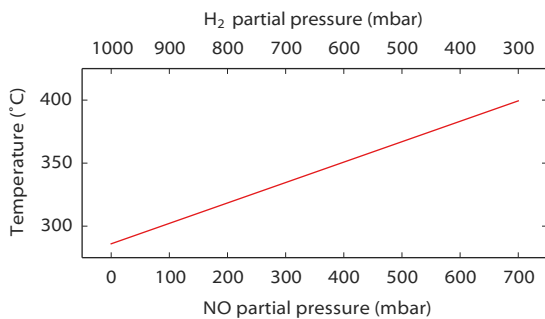
Figure 5.2. Sample temperature as a function of gas composition (mixture of NO and H_2 at 1000 mbar total pressure) for all measurements in this chapter. The sample heater was operated at constant power, but the difference in thermal conductivity between NO and H_2 results in a 100°C temperature difference between the higher and lower H_2 partial pressures used in this experiment.

unreconstructed

(1 × 3)

(3 × 3)   } 300–400°C

(4 × 3) and (4 × 2)

(4 × 3), (in)commensurate in K

(0.22 × 1)   100–150°C

faceting   300–400°C

0   100   200   300   400   500   600   700

NO partial pressure (mbar)
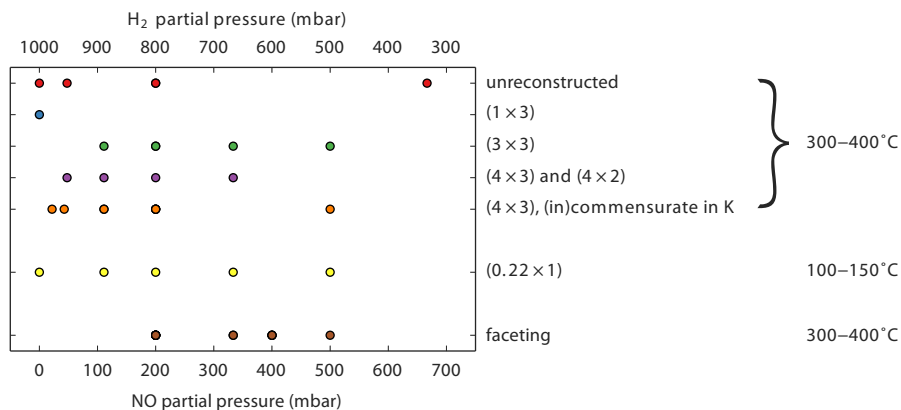
Figure 5.3. Observed reconstructions (periodicities) on Pt(110) as a function of gas composition (mixture of NO and H$_2$ at 1000 mbar total pressure). The sample temperature was in the range 300–400°C and can be found in figure 5.2, except for the "0.22" reconstruction which has been observed at approximately 100–150°C. The faceting always coincided with the presence of the (in)commensurate (4 × 3) reconstruction and is analysed in detail in figures 5.8–5.11. Figure 5.4 shows the scans along h and k corresponding to the reconstructions.

During high-pressure exposure the sample was heated at constant power, resulting in a temperature of 300–400°C depending on the gas composition (figure 5.2). At these temperatures, the ammonia production is problematic, with the ammonia signal in the mass spectrometer rising to values corresponding to tens of mbar in the reactor. Due to the low pumping speed for these molecules it was not possible to keep their partial pressures at a constant and low level throughout the experiment. Since these molecules also affected the leak rate of gas from the reactor to the mass spectrometer, and eventually completely inhibited the leak, their presence could not be monitored with any accuracy during the experiment. In addition, as the experiment progressed, the UHV pressure deteriorated, at some stage making it impossible to perform further sputter/anneal cycles to regain a clean sample.

5.3   Results and discussion

Many different surface structures have been observed on the platinum surface depending on the conditions. They can be classified in two groups: surface reconstructions, requiring modest rearrangement of platinum atoms, and faceting, corresponding to massive material transport along the platinum surface.
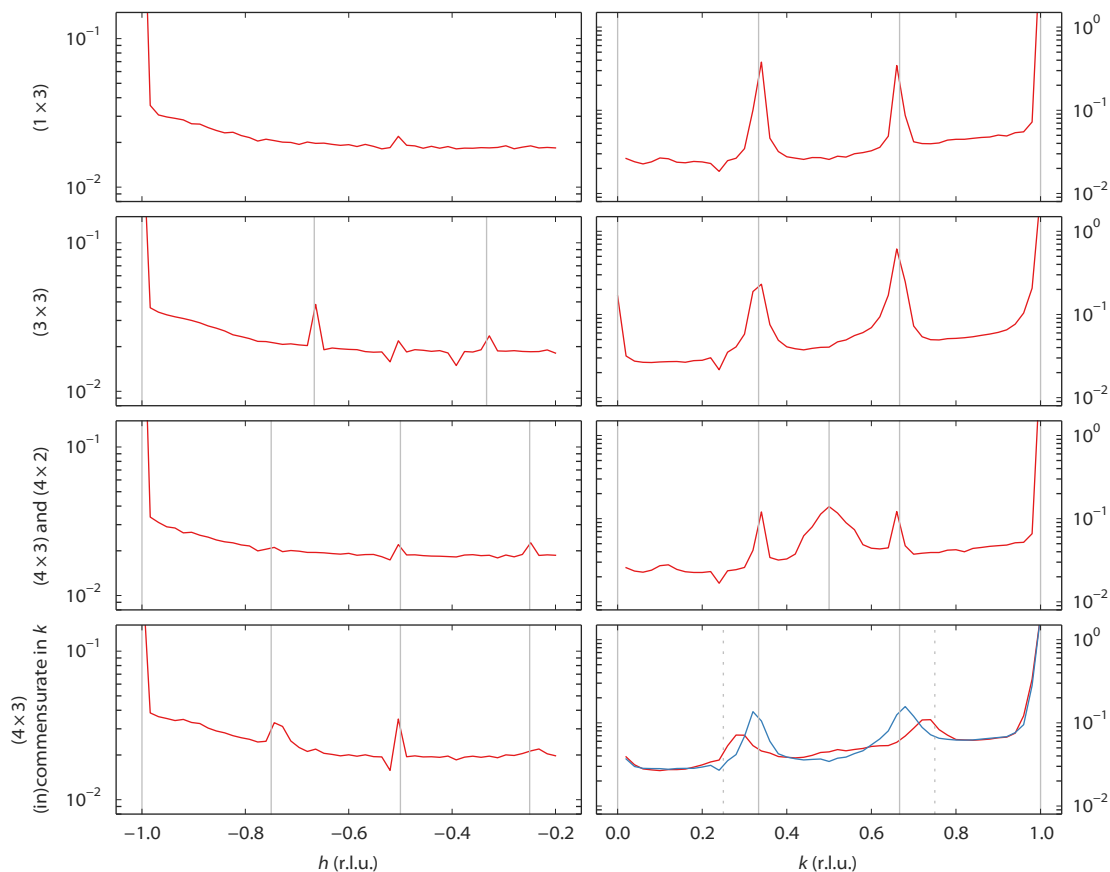
Figure 5.4. Observed reconstructions on the Pt(110) single crystal surface. See figure 5.3 for the conditions. Left column contains scans along $[h\,0\,0.5]$ in reciprocal lattice units (r.l.u.), right column along $[-1\,k\,0.3]$. The y-axes show intensity in arbitrary units. The solid vertical lines indicate the periodicity of the pattern. The lower right panel shows an incommensurate periodicity (red) that becomes commensurate (4×3) with time (blue). The dotted vertical lines mark $k = 0.25$ and $k = 0.75$.
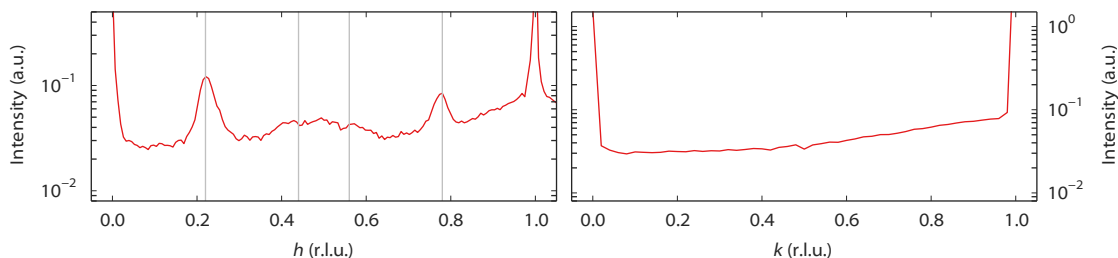
Figure 5.5. The "0.22" reconstruction observed at 100-150°C (see figure 5.3 for the gas composition where this reconstruction occurs). Left panel contains a scan along $[h\,1\,0.3]$, right panel along $[-1\,k\,0.3]$. There are peaks at 0.22 r.l.u. from the Bragg peaks along the h-direction, and a hint of the second order peaks as well, as indicated by the vertical lines in the left panel.

5.3.1 Surface reconstructions

When the partial pressures of NO and H_2 are varied, several reconstructions of the Pt(110) surface have been observed at 1 bar total pressure and at 300–400°C. Figures 5.3 and 5.4 indicate the appearance of the (1×3), (3×3), (4×3) periodicities plus some variations. At lower temperatures (100–150°C), another reconstruction appeared (figure 5.5), with peaks at 0.22 reciprocal lattice units (r.l.u.)[1] away from the Bragg peaks in the h-direction.

The (1×3) reconstruction observed in H_2 is likely the same missing-row reconstruction observed on the freshly prepared sample, but all the others have not been identified before. Few $(n \times 2)$ and $(n \times 3)$ reconstructions of (110) surfaces, formed under the influence of adsorbates at low pressures, have been reported, and they differ considerably in character. The H-induced (5×2) structure on Ni(110) consists of a zigzag pattern formed by short (2 atoms long), alternating pairings of the atom rows[98]. On the other hand, the O-induced c(6×2) structure on Cu(110) consists of a checkerboard-pattern of isolated copper atoms decorated by oxygen[99]. In this structure, the occupancy of metal atoms in the two upper layers is much lower than in the unreconstructed surface and there are no closed-packed rows. Finally, two N-induced (2×3) structures on Cu(110) are of the missing-row type[100], having one every three atom rows missing in the upper layer. These two structures differ by the number and position of the nitrogen atoms in the (2×3) unit cell. The l-scans along the superstructure rods of the (3×3) reconstruction

---

[1]In SXRD, the directions in reciprocal space are labeled by h, k and l, and coordinates are usually given in units of the basis vectors of the reciprocal lattice (i.e. reciprocal lattice units or r.l.u.). This concept is closely related to the Miller indices used to label lattice planes in crystals. For simple crystals, this ensures that Bragg peaks always have integer coordinates. By convention, the h and k directions are parallel to the surface, whereas the l direction is perpendicular to the surface and points outwards. See also figure 5.1 for the precise choice of h and k for a (110) surface.
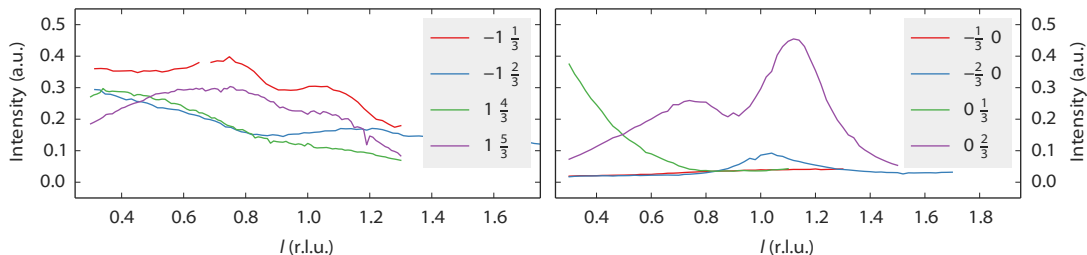
Figure 5.6. l-scans along some superstructure rods. The legends show the h and k values of each scan. The left panel shows the (1×3) reconstruction in UHV, with periodicities in l similar to those reported for the (1×3) missing row reconstruction by Robinson and co-workers[97]. The right panel shows the (3×3) reconstruction in a mixture of 200 mbar NO and 800 mbar H_2 at 320°C. A comparison with the left panel and the data from Robinson suggest that the (3×3) is a (1×3) missing row with additional periodic structure along the atom rows.
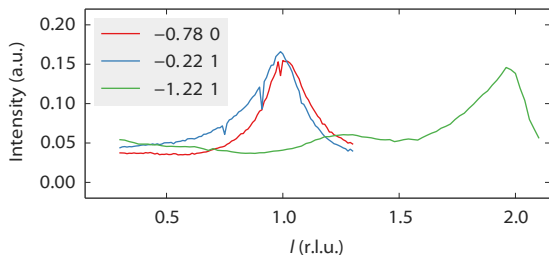
Figure 5.7. l-scans along the superstructure rods for the "0.22" reconstruction, taken at 150°C in pure NO at a total pressure of 200 mbar. The legend shows the h and k values of each scan. The intensity peaks strongly at integer l-values, meaning that the periodicity matches that of the bulk Pt lattice, suggesting that the reconstruction is some structure of Pt.

observed in our experiments (figure 5.6) suggest that it is a variation on the (1×3) missing row structure, with additional periodicity along the atom rows.

We have observed the incommensurate (4×3) structure on several occasions and it always transformed into a commensurate (4×3) structure with time. The incommensurability could be due to mixtures of (4×4) and (4×3) structures. Similar effects have been reported for variable fractions of (1×2), (1×3) and (1×5) missing-row reconstructions on Pt(110) induced by C segregation[101], and also for mixtures of (1×2) and (1×3) missing-row reconstructions of H- or Au-covered Pd surfaces[102, 103]. No l-scans have been obtained for the (4×3)-related structures, however, we suggest it could also be a variation on the (1×3) missing row. The "0.22" reconstruction, which is also incommensurate, seems to be completely different. It appears to be completely stable in time, and l-scans (figure 5.7) suggest that the

intensity derives from a significant restructuring of the Pt surface rather than an adsorbate overlayer pattern, but a more detailed structure analysis has not been performed.

As figure 5.3 indicates, there is no clear separation between the different structures as a function of gas composition. For the clean Pt(110) surface it is known that the free energies of the various $(1 \times n)$ missing-row reconstructions are very similar[104], with the consequence that small changes in conditions (for example the presence of small amounts of adsorbates from the gas phase or segregated impurities from the bulk) can easily push the system from one phase into another. A similar mechanism could be at play for the variety of reconstructions observed here, under high-pressure, high-temperature conditions.

5.3.2   Faceting

Near the end of the experiment, under conditions already probed before in this measurement session, the surface started faceting (see figure 5.3 for the conditions). This was observed by taking two-dimensional cuts perpendicular through a crystal truncation rod (CTR). A CTR is a scan along l connecting Bragg peaks of the crystal. Its shape is defined by the crystal termination, i.e. the precise configuration of atoms in the transition from the regular lattice in the crystal bulk to the empty space above it (vacuum or gas phase)[105]. The profile of a cut through the CTR contains information on the height variations on the surface. In our case, the two-dimensional cuts were constructed from a collection of continuous scans along the diffractometer angle ω[68] that were stitched together using *BINoculars* (chapter 4). The cuts in figure 5.8 reveal the appearance of satellite peaks, whose distance to the main peak is proportional to the distance Δl to the nearest Bragg peak. In other words, the extra peaks correspond to extra CTRs, tilted with respect to the [110] normal of the average surface. Indeed, sufficiently well-defined facets will give rise to an extra set of tilted truncation rods through every Bragg peak, as explained in figure 5.9. The angle of these facet rods directly corresponds to that of the surface normal of the facet. The full width at half maximum (FWHM) then gives a measure for the definition of the facet. The faceting angle was determined by a fitting procedure (figure 5.10) of which the combined results are shown in figure 5.11.

The facets are tilted by 8 to 12 degrees away from the (110) surface in the $[\bar{1}10]$ direction. The facet angle seems to be negatively correlated to the NO partial pressure, higher NO pressures resulting in smaller angles. Figure 5.11 also suggest that not all data points have been taken with the system in equilibrium. Especially for NO partial pressures above 300 mbar, the right panels indicate the response to be slow, on the time scale of the measurements. The FWHM of the CTR is a measure for the roughness of the crystal surface, and this shows, as expected, a clear
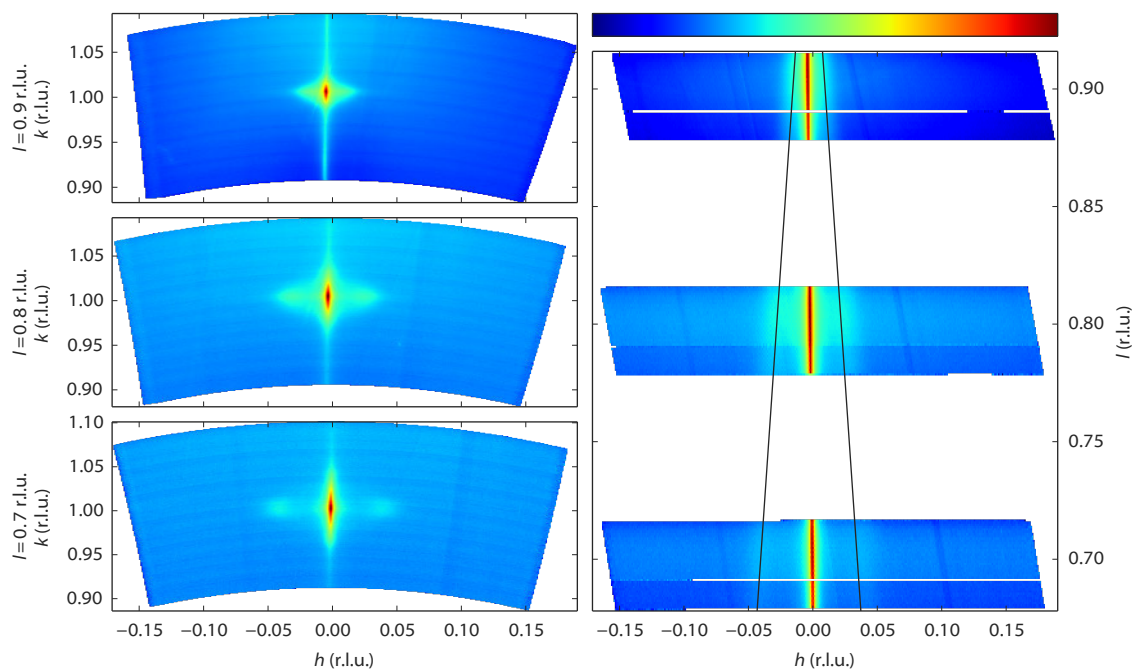
Figure 5.8. Faceting of the Pt(110) surface has caused the appearance of satellite peaks close to the crystal truncation rods (CTRs). The left panels show three (hk)-cuts at constant l, intersecting the $(10\,l)$ CTR at three values of l, obtained during exposure to a mixture of 400 mbar NO and 600 mbar H_2 at 350°C. The right panel is a projection of a subset of these data onto the hl plane, showing that the satellite peaks line up into two tilted CTRs that pass through the Bragg peak at $l = 1$. Therefore they can be interpreted as the CTRs of two sets of well-defined facets, and their directions correspond to the surface normals of the facets. The intensity ranges corresponding to the logarithmic colour scale (shown above the right panel) are for the lefts panel, from top to bottom, $[9.4 \cdot 10^{-6}, 1.7 \cdot 10^{-1}]$, $[3.0 \cdot 10^{-6}, 1.8 \cdot 10^{-2}]$, $[2.6 \cdot 10^{-6}, 5.1 \cdot 10^{-3}]$, and for the right panel, from top to bottom, $[3.1 \cdot 10^{-5}, 2.4 \cdot 10^{-2}]$, $[6.7 \cdot 10^{-6}, 4.4 \cdot 10^{-3}]$, $[5.7 \cdot 10^{-6}, 1.9 \cdot 10^{-3}]$.
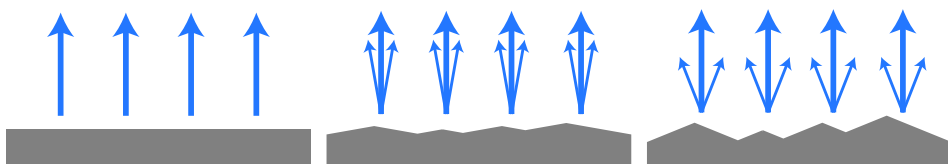
Figure 5.9. The surface termination of a flat surface gives rise to crystal truncation rods (CTRs) along the surface normal (left panel). The presence of facets on the surface results in the appearance of titled truncation rods (middle and right panel).
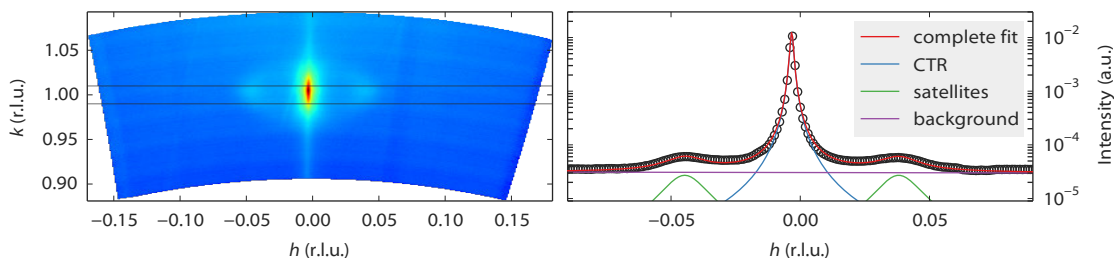
Figure 5.10. The region indicated in the left panel was used to further analyse the faceting. The position of the satellite peaks has been fitted using a least-squares optimization of three Lorentzians plus a sloped background. The satellite peaks were assumed to be symmetrically positioned on either side of the rod, and to have identical peak widths.

correlation with the faceting angle. The FWHM of the facet rods took some time to reach a constant value, indicating that the facets were growing in average size, at least until measurement 10, which was acquired 4 hours after measurement 1.

The tilt of approximately $10°$ implies that the facets typically have the (320) structure (figure 5.12), a crystal plane that makes an $11.3°$ angle with the (110) plane. The higher index orientations (430) and (540), having a similar structure as (320) but with 4 and 5 atoms per terrace and tilts of 8.1 and $6.3°$ respectively, are likely to be present as well, especially at higher NO pressures.

Faceting of the Pt(110) into mainly (320) has been observed with CO and O_2 exposure in the 10^{-4} mbar regime[106, 107]. In this case, the presence of both reactants is required to create the facets, and the mechanism is suggested to be related to the strong binding of oxygen on step sites, and material transport induced by switching between the (1×2) missing row reconstruction and the unreconstructed surface due to CO coverage fluctuations. The reactivity of the (320) plane is higher than that of the (110) plane and under some conditions this gives rise to kinetic oscillations[108].

In the case of the NO and H_2 exposure, a comparable mechanism could be responsible for the faceting, causing the free energy of the (320) and similar orientations to reach a lower value than the free energy of the (110) surface. As in the case of CO and O_2 exposure, it could be due to an adsorbate binding strongly to the steps, and in this case NO, H_2O, NH_3, or atomic oxygen are likely candidates.

However, there is an alternative explanation that is supported by DFT calculations by Reuter and co-workers[109]. They show that the surface stress of a Pt(110) surface is dramatically influenced by adsorbed NO molecules due to the strong repulsive interaction between NO molecules at higher coverages. Their calculations show that the surface stress in the $[1\bar{1}0]$-direction changes from $3.0 \, \text{N/m}$ (tensile) for the clean surface to $-3.0 \, \text{N/m}$ (compressive) for a 1 ML coverage of NO. The change along the $[0\,0\,1]$-direction is less dramatic, the surface stress being $-0.2 \, \text{N/m}$
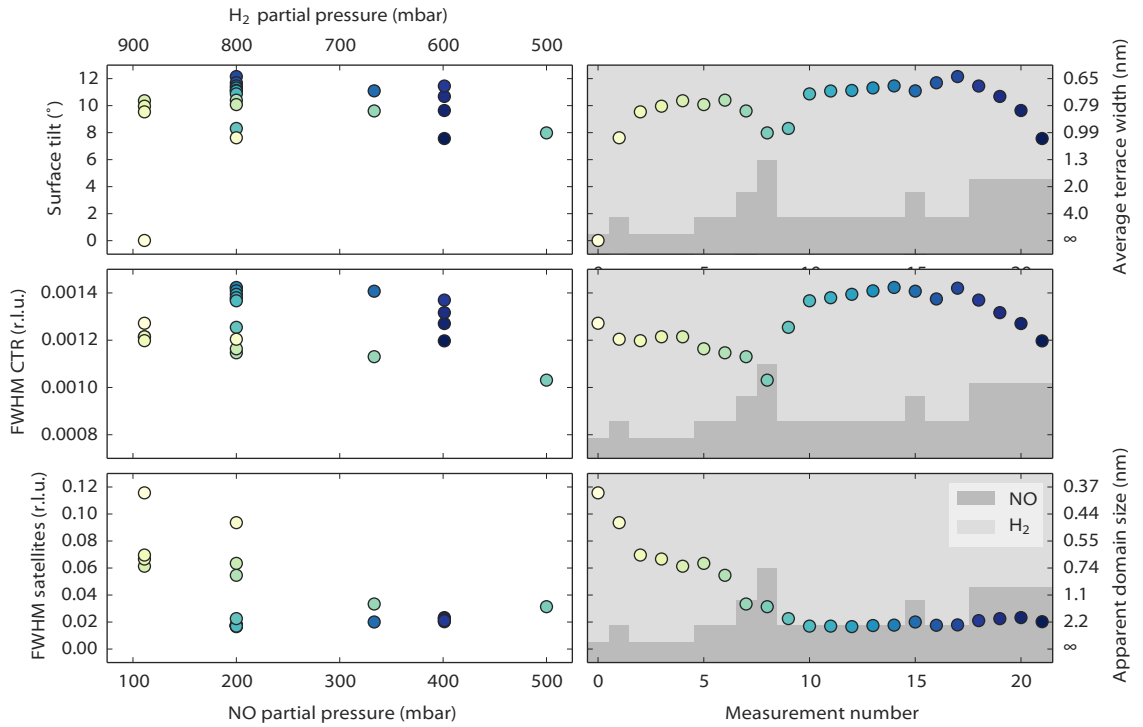
Figure 5.11. Combined results of the fitting procedure described in figure 5.10. The panels on the left represent fit parameters as a function of gas composition (NO and H_2 mixtures at a total pressure of 1 bar), the panels on the right show the same parameters as a function of measurement number, with the fractional gas composition indicated by the shades of grey in the background. See figure 5.2 for the sample temperature. The upper panels contain the angle of the surface normal of the facets and the corresponding terrace width (right axis), which is calculated from the position of the satellite peaks. The middle panels correspond to the full width at half maximum (FWHM) of the main rod, while the lower panels show the FWHM of the facet rods, both in reciprocal lattice units (r.l.u.). For the satellite peaks the FWHM has been converted into the apparent domain size (right axis). This calculation is only valid in the unlikely case that no other effects contribute to the FWHM, and must therefore be considered a lower bound for the domain size.

top view

[0 0 1]

[ī 1 0]

side view

[1 1 0]

[ī 1 0]
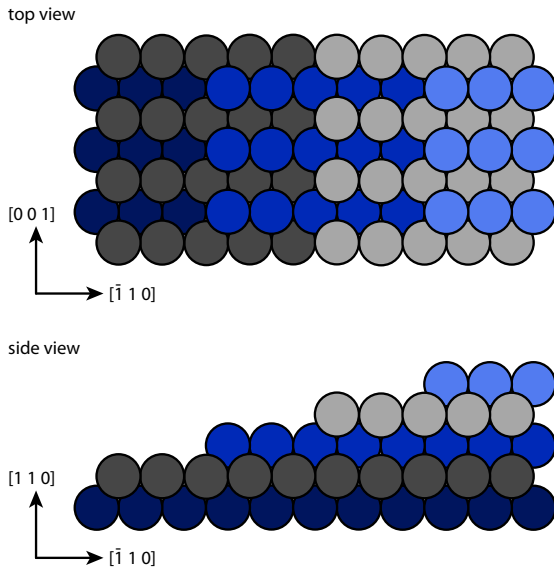
Figure 5.12. Ball model of the stepped Pt(320) surface having its surface normal titled 11.3°
away from the [110] orientation.

for the clean surface and 1.4 N/m for the NO covered surface. Within the accuracy
of the DFT calculations, the chemical potential required for 1 ML NO coverage
matches that of the high-pressure, high-temperature NO exposure described in this
chapter. The faceting in the [1 1̄ 0]-direction could be a way for the surface to cope
with a large change in surface stress in this direction. This concept is supported
by literature. Hanesch and co-workers report morphology changes on mesoscopic
length scales of Pt(110) surfaces induced by surface stress[110]. Adsorbate-induced
surface stress has been measured on Ni surfaces, in particular for CO on Ni(100)
and (111)[111], and for various atomic species on Ni(100)[112]. Given the fact that the
DFT calculations show a large change in stress in the direction where the faceting
occurs, we suggest that the NO-induced surface stress drives the faceting, rather
than enhanced NO adsorption at steps.

5.4   Outlook

Pt(110) shows a variety of surface structures during exposure to mixtures of NO and
H_2. The appearance of many reconstructions indicates the sensitivity of the surface
to adsorbates. The precise conditions leading to each of the observed reconstructions
warrant further investigation. Combining surface X-ray diffraction with a real-space
microscopy technique such as STM should make it easier to determine the structural

details of the observed reconstructions. For a next round of experiments it would be preferable to start with the proper (1×2) missing-row reconstruction of the genuinely clean Pt(110) surface. This requires annealing the Pt sample in O_2. In addition, it would be better to set the gas composition and temperature independently. Longer waiting times (in the order of hours) at each set of conditions are also necessary to ensure that the observed structures reflect true equilibrium. In addition, the presence of the ammonia needs to be avoided or suppressed, or its role should be studied systematically.

For the faceting it is important to understand why it only occurred after prolonged exposure, near the end of the experiment, and not earlier when the same conditions where applied to the sample. Possible explanations could be (again) the presence of ammonia or a contaminant from the crystal bulk or the gas phase. DFT calculations on stepped Pt(110) surfaces could provide the definitive answer to the mechanism driving the faceting, but calculations on stepped surfaces are still challenging due to the large unit cell required. In addition, the influence of the facets on the activity and selectivity of the Pt(110) surface for NO reduction by H_2 is a relevant topic for further work, both experimentally and using DFT.

Apart from these suggestions for follow-up experiments, there is another, perhaps even more challenging direction, in which research on the interaction of NO with platinum should proceed, namely to go beyond flat surfaces and study the effect of NO and H_2 on supported nanoparticles, a more realistic model catalyst. The next chapter describes this step.
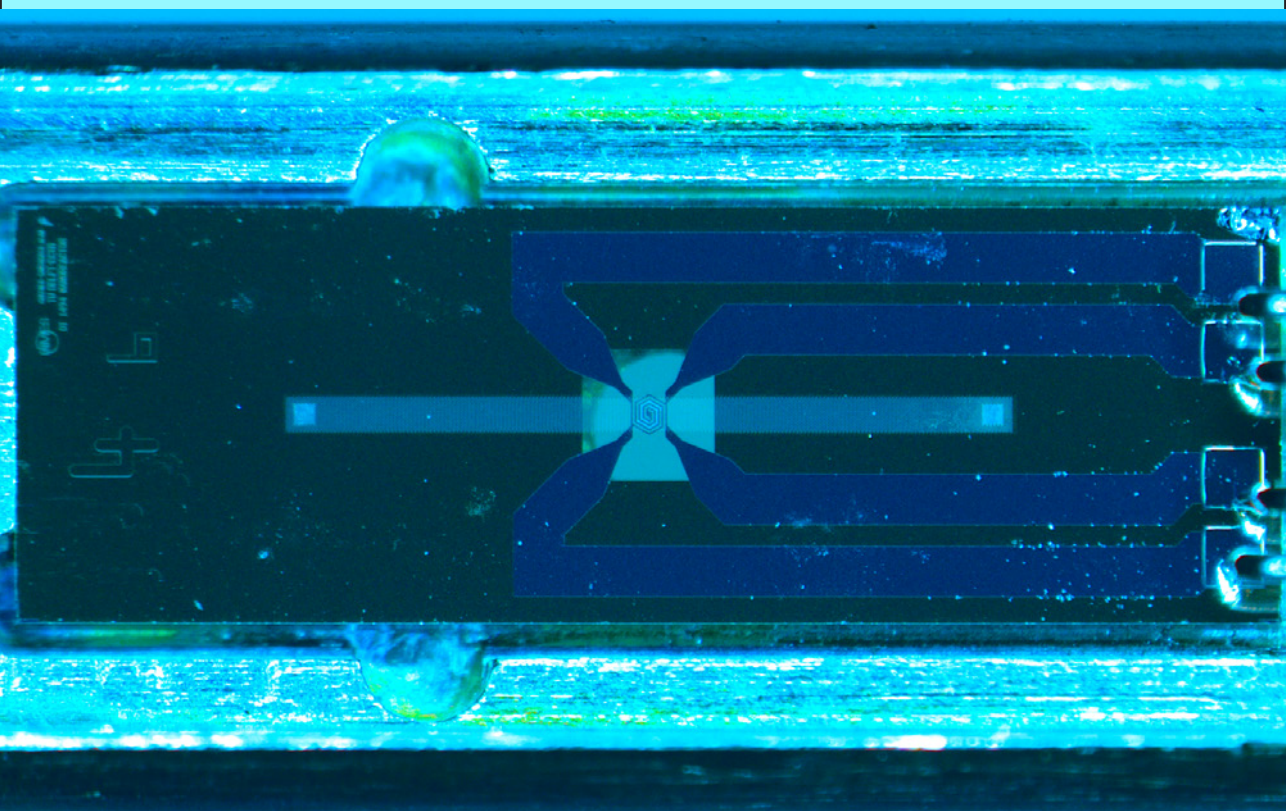
Chapter 6

NO reduction by H$_2$ over Pt nanoparticles studied by TEM

Where the previous chapter described an experiment in which we overcame the pressure gap for a simple catalytic reaction, the current chapter goes one step further and simultaneously overcomes the materials gap. The exposure of platinum nanoparticles to mixtures of nitric oxide (NO) and hydrogen (H$_2$) has been studied by *in-situ* Transmission Electron Microscopy (TEM). Similar to the faceting observed on the flat surface, we observe how material is transported and the particles change their morphology, depending on the gas composition. The particles have a faceted shape in hydrogen-rich environments, but lose their sharp corners in NO-rich environments and become more spherical.

6.1   Introduction

In the chemical industry a catalyst is never a flat surface, but rather a complex material that needs to be described at several different length scales, ranging from nanometres to at least millimetres[3]. In this chapter the smaller length scale is considered, namely that of the individual metal nanoparticles. Catalysis on small particles can be different from that on flat surfaces due to a variety of effects[6]. For example, on a small particle, there is a larger variety of adsorption sites and there are more undercoordinated metal atoms. Furthermore, spill-over effects can occur, both between the nanofacets on the particle and between the particle and support[8]. In addition, the electronic structure of the small particle can differ from that of the extended surfaces of the same material. Similarly, the interaction between the particle and the support can lead to further electronic effects[113].

The equilibrium shape of a crystalline particle is determined by the relative free energies of the terminating surfaces[114]. When the particle is in a gas environment, these are, in fact, the interfacial free energies between the metal surface and the gas phase and these depend heavily on the gas species present, on their partial pressures, and on temperature. The faceting of a platinum (110) surface into (320) and similar orientations, as described in the previous chapter, can be seen as a flat-surface analogue of this effect.

We have not found any publications describing *in-situ* studies on the interaction of platinum nanoparticles with NO. The closest are measurements on palladium particles during CO and NO cycling, where EXAFS, infrared spectroscopy, and mass spectrometry have been used to acquire indirect information on the particle shape, based on the observation that the palladium coordination is lowered during CO exposure and recovers in NO[115]. However, a later X-ray diffraction study proved this change in coordination to be caused by carbon dissolution from dissociated CO[116]. Similarly close is an environmental TEM (ETEM) study on CeO_2-supported platinum particles exposed to 1 mbar of CO, air, N_2 or O_2[117]. Whereas the platinum particles have a strongly faceted shape in vacuum and in N_2, the particles become somewhat rounded in O_2, and even more spherical in CO. A recent *in-situ* TEM study on the oscillatory behaviour of CO oxidation on platinum particles shows similar refaceting depending on the CO partial pressure[118].

6.2   Methods

Our TEM experiments have been performed with a micromachined nanoreactor[23, 119]. We have employed the latest generation of these devices, integrated on a single die[13]. It consists of a 0.5 μm deep gas channel etched in a silicon die, with electron-transparent windows that allow for in-situ TEM measurements of metal particles in
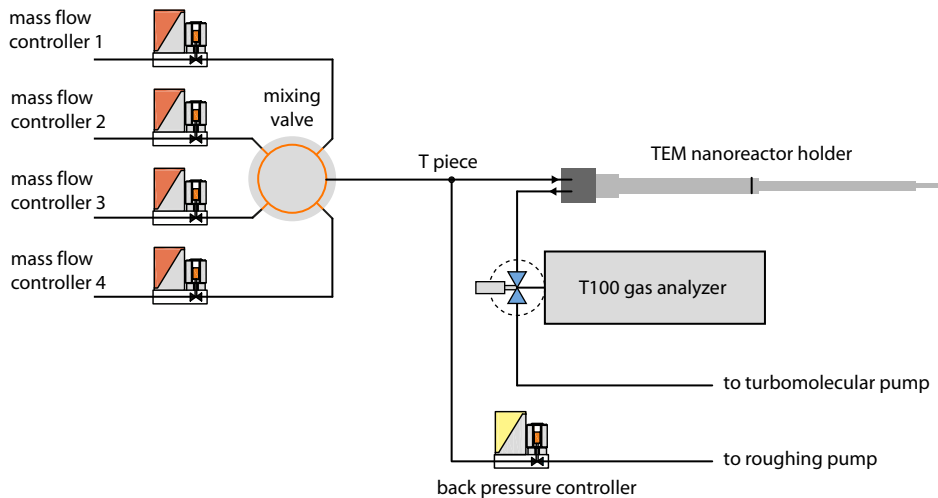
Figure 6.1. Schematic of the gas system to operate the nanoreactor in a flow configuration. The main flow path leads from the mixing valve via the T-piece and the back pressure controller to the rouging pump. Only a small fraction flows from the T-piece through the small nanoreactor channel and into the T100 analyzer[120]. When working at pressures beyond 1 bar (as set by the back pressure controller), the flow through the nanoreactor exceeds the maximum flow into the mass spectrometer of the T100 analyzer, and a turbomolecular pump is used to pump away the excess gas. This does not affect the time-resolution for gas detection thanks to the small volume of the inlet of the T100 analyzer. Note that the mixing system shown here is simplified and does not include the carrier gas.

a gas environment up to 14 bar and up to 800°C. The electron-transparent windows consist of a 15 nm amorphous silicon nitride film, and this film also coats the interior of the other parts of the channel, to ensure chemical inertness. Two viton O-rings connect the gas channel to a pair of capillaries in a dedicated TEM sample holder. A platinum heater is embedded in the nanoreactor directly above the gas channel and heats a small region around the electron-transparent windows, while simultaneously allowing temperature sensing by use of a calibrated resistance measurement.

The nanoreactor is operated in a flow configuration as shown in figure 6.1. Since the channel through the nanoreactor is extremely small (the reactor volume is 0.4 nl), the flow cannot be controlled by commercially available flow controllers. Instead, a certain gas pressure is set at the inlet, and the outlet is fed directly into a turbomolecular pump. To get a reasonable response time when changing the composition of the gas mixture, a gas flow is set up through a T-piece that is connected as close as possible to the inlet of the reactor and to a pressure regulator, backed by a vacuum pump. Most of the gas only flows through the T-piece and the pressure regulator, and only a small fraction flows through the reactor. The volume of the
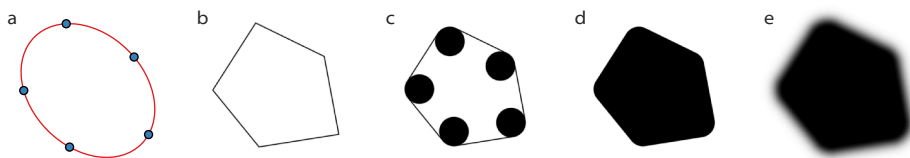
Figure 6.2. Construction of a polygon on a discrete grid, having rounded corners and a fuzzy boundary. (a, b) The corner points are defined by polar coordinates w.r.t. the center of the ellipse. (c) The inscribed circle is drawn at every corner. (d) The interior is filled using a hole-filling algorithm. (e) The edges are drawn with a gaussian intensity profile.

capillary between T-piece and reactor is large compared to the flow in this region, resulting in refresh times in the order of minutes. The gas stream is supplied by a gas mixing system[11, 56] that allows composing arbitrary mixtures of up to four gases plus a carrier gas at pressures up to 6 bar with a typical flow of 10 ml$_n$/min.

The outlet of the reactor is connected directly to a differentially pumped mass spectrometer (T100 gas analyzer[56]). The pressure drops entirely over the length of the nanoreactor since the gas channel in the nanoreactor is small compared to the diameter of capillaries leading to and from the reactor. The geometry of the nanoreactor is fully symmetric so it is assumed that the pressure in the central region of the nanoreactor (with the windows and heater) is half the pressure at the inlet. Since all gas from the reactor is pumped into the mass spectrometer (via the differential pumping stage), the sensitivity of the mass spectrometer is independent of the reactor pressure. The delay between an event in the reactor and detection by the mass spectrometer is approximately 30 s.

A platinum nanoparticle catalyst is loaded into the nanoreactor as a solution of tetraamine platinum nitrite in water or ethanol, which is left to dry in air, followed by calcination and reduction. In this process, the salt decomposes and the result is a dispersion of platinum nanoparticles with sizes ranging from 5 to 50 nm, inhomogeneously distributed in clusters along the entire nanoreactor gas channel.

The main conclusion reached in the present study is that Pt nanoparticles change their shape in response to the gas composition. As we will see, the most prominent feature is the sharpness of the edges and corners of the particles. Although it is relatively easy to recognise changes in the sharpness when visually inspecting sequences of TEM images, it takes effort to capture these variations in a robust, systematic, and quantitative way. We have developed a new method especially for this purpose, based on the least-squares fit of a 2D model, which is illustrated in figure 6.2 and described in detail in appendix 6.A in this chapter.

6.3 Results and discussion

Figures 6.3, 6.4 and 6.5 show an ensemble of Pt particles that we followed during its first exposure to NO after sample preparation. Starting from 1 bar pure H_2 at 150°C, the inlet gas composition was first changed to NO. As explained above, the low refresh rate of the gas in the capillary leading to the nanoreactor inlet translated to a gas composition change in the reactor starting after a delay of 2 minutes and with a transition time of another 2 minutes. Two dramatic effects are immediately visible in the TEM images. The number of nanoparticles has decreased and the remaining particles have become rounder in the NO atmosphere.

The number of Pt particles started decreasing as soon as the NO partial pressure in the reactor was increasing (figure 6.4) from t = 200 s. The TEM images obtained during the next two minutes show that small particles were shrinking. Although the bigger particles showed no clear change in size, they probably accommodated the Pt lost from the smaller particles. These observations indicate that individual atoms were diffusing over the support between the Pt nanoparticles, resulting in a net flux from the smaller to the larger particles. This mechanism is known as Ostwald ripening[121]. The alternative mechanism of Smoluchowski ripening in which entire nanoparticles diffuse and merge[122], can be ruled out. Since the process is not reversible, a systematic study of the effects of gas composition on the ripening rate and mechanism was not performed in the context of this first in-situ experiment on the effect of high-pressure H_2 and NO atmospheres on Pt nanoparticles. The dramatic increase of the ripening rate of Pt particles induced by NO has been reported by Lööf and co-workers[123]. They found that the effect of NO is stronger than that observed for O_2, which already enhanced the ripening compared to H_2 and Ar. They suggest that an NO-containing Pt complex is the mobile species responsible for the fast ripening.

The second effect observed in the experiment is the reversible change in the particle shape depending on the gas composition. This effect could be reproduced repeatedly in two different nanoreactors loaded with Pt particles. In order to substantiate our visual impression of systematic variations in particle shape with gas composition, we have quantitatively analyzed the shapes of some of the larger particles in the ensemble using the fitting procedure described in appendix 6.A of this chapter. Figure 6.5 shows the result. The lower panel displays the best-fit values of the corner rounding radius as function of time. Although the rounding radius is noisy, a correlation with the NO partial pressure is visible: higher NO pressures correspond to more rounded particles. There are two reasons for the noise on the radius. One is the low contrast between particle and background, resulting from the necessity to work with a low electron dose. The other is the spatial inhomogeneity of the amorphous SiN nanoreactor windows, which makes the background noisy. As a result, the fitting procedure did not always converge reliably. For some parameters,
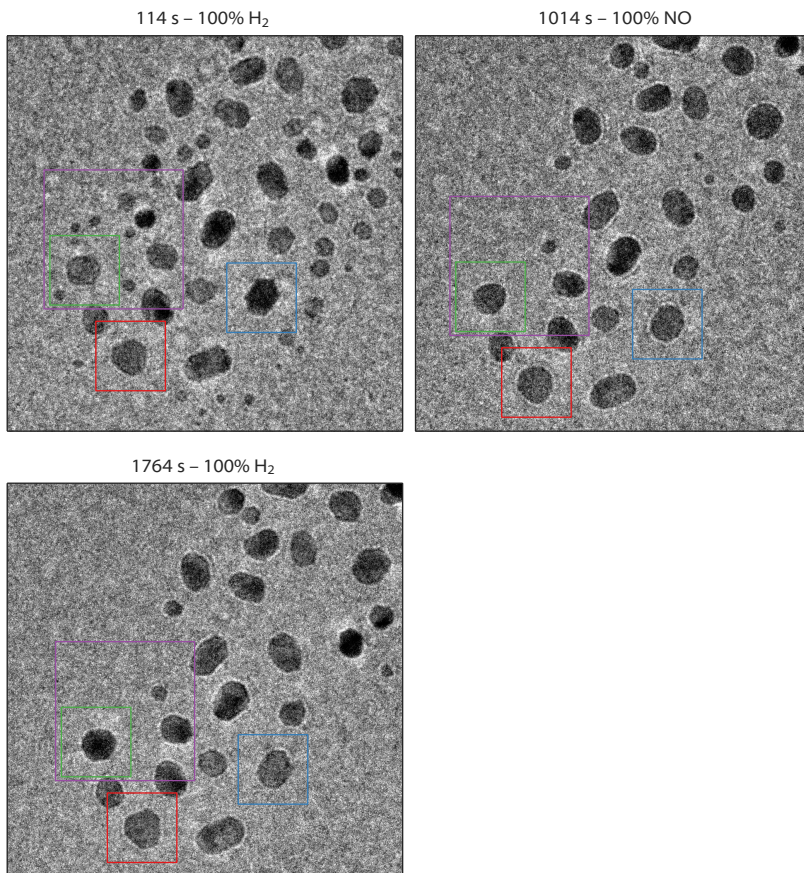
Figure 6.3. Shape variations of Pt particles while the gas composition was varied from pure H_2 (upper left panel) to pure NO (right panel) and back (lower panel), at 1 bar and 150°C. An ensemble of particles has been imaged every 3 seconds with an acquisition time of 1 second per frame. The imaging started at $t = 0$ in pure H_2, see the lower panel of figure 6.5 for more detail on the timing of the gas changes. The sample was continuously exposed to an electron dose of 300 e/Å^2s at 300 keV. The size of the images is 92×92 nm^2. Three particles, indicated with red, blue and green rectangles, are analyzed in more detail in figure 6.5. Note the sintering taking place between the left and middle panels (purple rectangle), which is shown in more detail in figure 6.4.
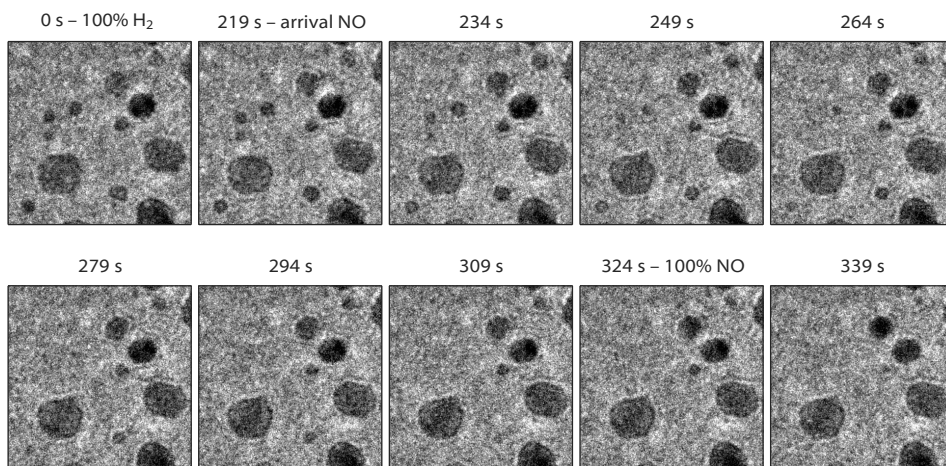
Figure 6.4. Rapid ripening took place at 150°C when NO was flowed through the reactor. The initial hydrogen atmosphere did not result in any noticable evolution, but once the NO partial pressure started increasing (from t = 219 s), the particles changed in size. Small particles shrank and disappeared on a time scale of tens of seconds, larger particles seemed unaffected, within the resolution of the images. This indicates that the mechanism of the process is Ostwald ripening. The images correspond to 32×32 nm^2 cutouts of the larger images, such as those in figure 6.3.
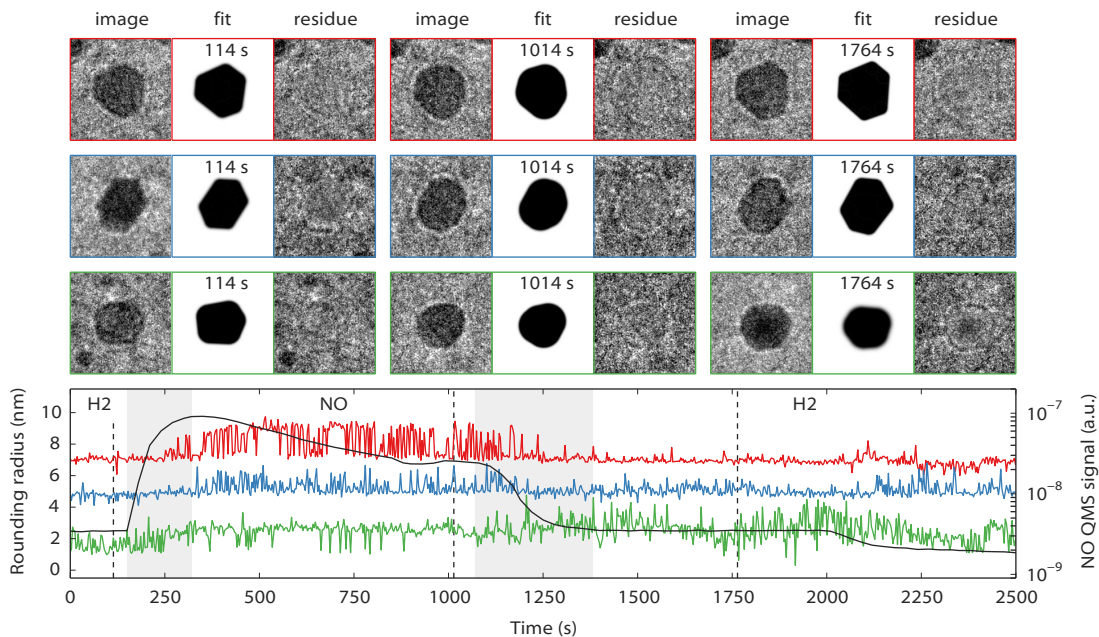
Figure 6.5. Three particles from the ensemble of figure 6.3 that have been analysed with the fitting procedure (upper panel / red, middle panel / blue, and lower panel / green), each image corresponds to 16×16 nm^2. The graph in the lower panel shows the rounding radius of the corners, as determined by the fit (offset from zero by 6 and 4 nm for red and blue respectively). The gas composition is indicated by the labels and the black curve in the lower panel, the two grey sections correspond to transitions from one gas to another. Note that the sensitivity of the quadrupole mass spectrometer (QMS) to NO reduced in time, due to the gain of the electron multiplier being affected by the gas in the QMS chamber. For each particle, the raw data, the fit as determined by the least-squares optimization, and the residue (raw image minus fit) are shown at three different points in time, corresponding to the vertical dashed lines in the graph. The model does not incorporate the Fresnel scattering on the edges of the particles, and this causes the boundaries of the particles to remain visible in the residue. Note the correlation between the presence of NO and the rounding radius, both in value and noise level.

especially the rounding radius, the final value strongly depends on the initial values. The two-level character of the rounding radius is caused by the upper limit of the rounding radius (approximately the particle radius) that was enforced by the fitting procedure.

6.4   Conclusion

In our high-pressure TEM observations we have witnessed two effects of the presence of NO in the gas mixture on ensembles of Pt nanoparticles. NO leads to a rapid ripening of the ensemble, with smaller particles shrinking and disappearing, i.e. Ostwald ripening. Furthermore, the particles become more rounded in the presence of NO. The latter effect can be viewed as the particle analogue of the break-up of the Pt(110) surface into vicinal orientations, that was discussed in the previous chapter. The explanation hypothesized there, namely that the adsorption-induced surface stress on the low-index terraces is reduced by the introduction of a high density of steps, could also be at play at the (111) and (100) surfaces, thus reducing the size of all facets and introducing larger vicinal regions, the rounded corners, on the nanoparticles. Since the steps that are introduced via the adsorption-induced stress scenario provide strongly coordinating adsorption sites with potential catalytic benefits, this mechanism may be of direct practical relevance for the performance of catalytic nanoparticles under high-pressure conditions.

6.5   Outlook

It would be interesting to determine the dependence of the rounding on the NO pressure, or rather on the chemical potential. In the previous chapter discussing the Pt(110) surface we reported that different NO partial pressures seem to induce different vicinal surfaces, e.g. (320) or (540). This suggests that the precise roundness of the nanoparticle will depend sensitively on the NO pressure. Assuming that only the chemical potential of the adsorbate species plays a role and not kinetics, this could be similar to what Yoshida and coworkers reported for CO on Pt particles[117]. They found that when exposing initially faceted Pt particles to 1 mbar CO at room temperature, the particles become round, and when increasing the temperature to 200°C this effect weakens.

Thus, repeating the experiment at lower NO pressures would be a logical next step. With the nanoreactors it is difficult to probe the mbar regime and below, but this is the regime where the use of ETEM is well established, so it is possible to cover several orders of magnitude in pressure. A higher signal-to-noise ratio of the TEM images than shown in this chapter is needed to capture the fine details in the shape of the particles. Since there are no dynamic processes that need to be followed, this

is feasible without increasing the electron beam intensity to avoid beam effects, by using longer exposures, or preferably averaging series of short-exposure images to avoid resolution loss due to drift.

Appendix 6.A   Particle shape analysis

When exposing the platinum particles to varying ratios of NO and H_2 mixtures it became clear that it was desirable to quantify changes in particle shape. We have developed a new fitting method that quantifies the degree to which the corners of a faceted nanoparticles are rounded. This method does not rely on edge detection, contrary to other methods for analysing TEM images of particles described in literature[117, 118]. In those methods, the precise location of the contour of a particle is established, and a curve fitting procedure is used to obtain the optimal fit of a 1D curve in a 2D space. The weak element in these methods is the edge detection, which is a non-trivial operation, contrary to what is implied in these publications. In addition, the edge detection fails if the signal-to-noise ratio is low, as is the case in the dataset at hand in the present chapter. In this case the low signal-to-noise ratio is caused by the electron-transparent nanoreactor windows that give a speckled background pattern, and the low electron dose required to minimise beam effects. We use a least-squares optimization to fit a 2D simulated particle silhouette to a TEM image, or equivalently, fit a 2D surface in a 3D space, thus avoiding edge detection completely.

We first describe the geometrical construction of the rounded polygon and then show how this is translated into a matrix of greyscale values on a discrete grid, matching the pixels of a TEM image.

The number of corners of the polygon N is assumed to be fixed and not a fit parameter. The degrees of freedom for the corner positions should be limited, e.g. to avoid concave polygons. Therefore it is assumed that all corners of the polygon are located on an ellipse, as is shown in figure 6.2a. The ellipse is described by two radii (a, b), the center coordinates (x_0, y_0), and an orientation angle ϕ of the major axis. The position of the corners can then be specified as a list of angles $(0 \leq \alpha_1 < ... < \alpha_N < 2\pi)$.

In the absence of rounding, the polygon is simply formed by the N straight lines connecting neighboring corner points (figure 6.2b). Rounding is introduced via a single corner radius r for all N corners of the particle, as illustrated in figure 6.2c. The straight line segments then terminate at the tangent points to the inscribed circles at each corner. Next, the interior of the rounded polygon is filled (figure 6.2d). At this stage, the silhouette has sharp edges whereas the TEM images show edges that are somewhat blurred. This aspect needs to be taken into account. There is a second reason for blurring the sharp edge, namely to translate the mathematical shape of

figure 6.2d in to a non-jagged grid representation that evolves continously under variations in the corner position and corner rounding radius (even for variations smaller than the size of a pixel). For this purpose, we make the pixel greyscale values for pixels outside the silhouette drop off with the distance to the nearest point on the contour of the rounded polygon according to a Gaussian with a width σ (figure 6.2e). This approach ensures continuity of the least-squares error χ in all parameters when σ is not much smaller than the pixel size.

The result of figure 6.2e is scaled and an offset is added to match the background and foreground intensities of the TEM image. The entire procedure has $9 + N$ parameters and results in a least-squares error χ that is not only continuous but also differentiable with respect to these parameters, with the exception of the rounding radius parameter r, which clips at an upper limit depending on the particle size. This upper limit is given by the radius of the largest inscribed circle (at every corner) that fits within the enclosing polygon and this approximately matches the particle radius.

We use a least-squares optimization procedure based on a steepest-descent algorithm from Scipy[52]. Due to the low signal-to-noise ratio in the dataset in this chapter, the procedure did not always converge to a shape that properly describes the particle, and manual tuning of the starting values was required. This can likely be improved by tailoring the optimization algorithm to this particle model and its choice of the parameters, but this has not been attempted. The fit procedure typically takes up to one minute on a 2.8 GHz Intel Core i7 CPU to converge for a 80×80 pixel image.
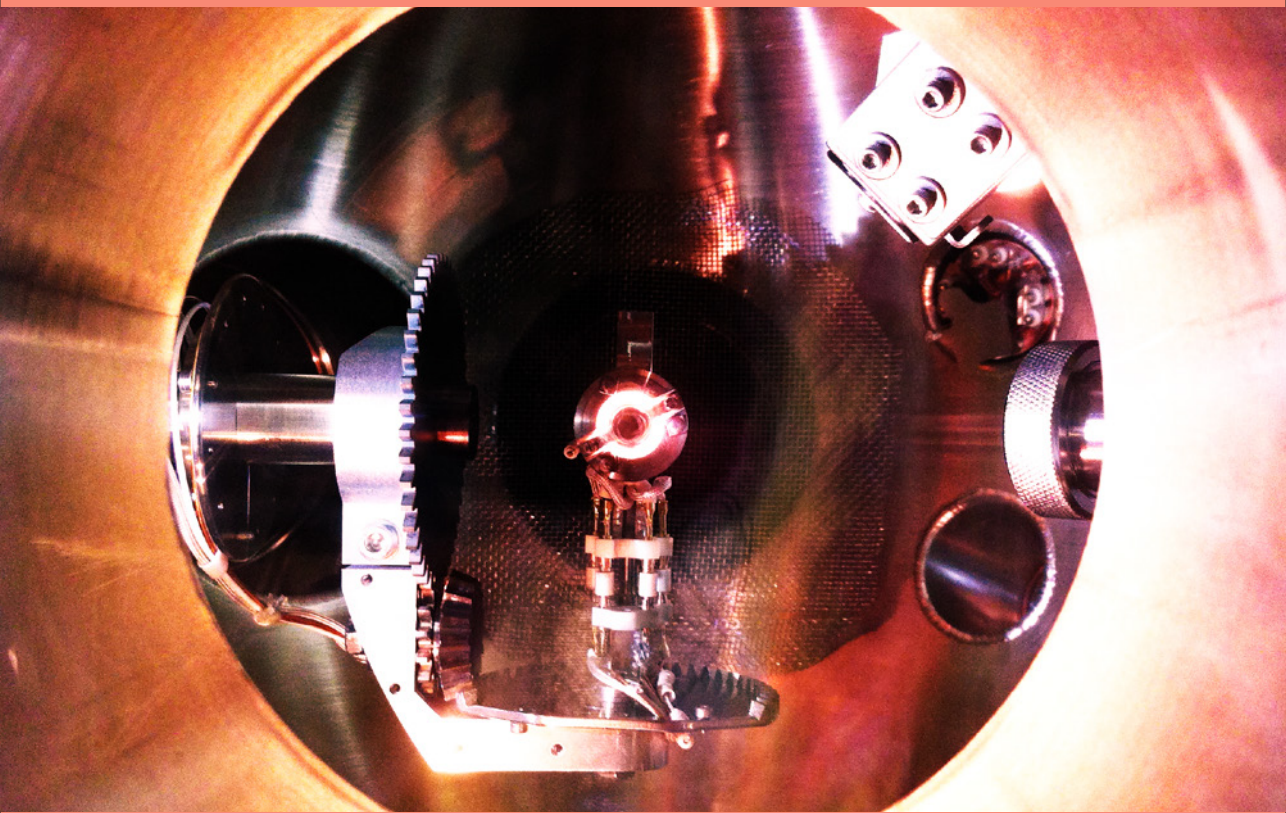
Chapter 7

Oxide shell formation during spontaneous oscillations in the catalytic oxidation of CO on palladium nanoparticles

Spontaneous reaction oscillations on palladium nanoparticles during the catalytic oxidation of CO have been investigated by a combination of in-situ microscopy techniques and X-ray scattering. The oscillations are identified as sequences of switches between a high- and a low-reactivity phase and vice versa. The high-reactivity phase is accompanied by the presence of a 1 nm thick palladium oxide shell that encapsulates the metallic core of each particle. Based on this observation, a mechanism is proposed for the oscillations that involves the catalytic activity and the stability of the palladium oxide.

7.1   Introduction

Spontaneous reaction oscillations have been observed for many heterogeneous catalytic systems, ranging from single-crystal model systems in ultrahigh vacuum [124], to thin films[125], supported nanoparticle systems[126], and even up to commercial reactors such as automotive catalytic converters[127]. Only for a few single-crystal model systems, atomic-scale mechanisms for reaction oscillations have been studied in detail[94, 128–131]. In this chapter, spontaneous oscillations during CO oxidation on Pd nanoparticles, supported on flat substrates, are investigated with a variety of techniques. The measurements suggest that the oscillation mechanism on the particles could be similar to that on Pd single-crystal surfaces.

In previous work on the Pd(100) surface[131], a high-pressure mechanism has been identified that features a refined interplay between variations in the step density or surface roughness, the stability of the PdO surface oxide (which depends on the surface roughness and the local gas composition), and the catalyst activity (which in turn depends on the state of the surface). A full cycle of the oscillation on Pd(100) proceeds as follows. The reaction takes place under conditions that are so oxygen-rich that the smooth metal surface is unstable with respect to oxidation. As a consequence, a thin surface oxide is formed. The oxidised surface is more reactive than the metal, causing a higher consumption of CO and thus a drop in CO partial pressure as soon as the formation of the surface oxide starts. This locally accelerates the oxidation and makes it synchronise across the whole surface. In the oxide phase, the reaction follows the Mars-Van Krevelen mechanism[132]: CO adsorbs on the surface oxide, and reacts with this oxide to form CO_2. In this process, some of the Pd atoms get reduced and become mobile, diffusing out on top of the oxide until they get re-oxidised, thereby increasing the surface roughness. Eventually, this roughness destabilises the surface oxide and the systems switches back to a rough metallic surface. The reason for this is thought to be that the CO binds even more strongly to the step sites on the metal surface than to terrace sites. This increasingly favours the metal surface as roughening on the oxide progresses. The lower activity of the metal surface makes the CO partial pressure increase again, now further stabilizing the metal surface. The high surface mobility of the metal surface leads to a swift smoothening. This removes the binding advantage of CO to the step sites and makes the metal surface instable again, causing the whole process to start over again.

Oscillating nanoparticle catalyst systems have been reported, but there have been few attempts to systematically investigate the precise oscillation mechanisms. Detailed mass spectrometry analysis of oscillations during CO oxidation on platinum particles by Jensen and co-workers[133] suggested that the surface-transition mechanism described above for Pd(100) could also apply to these nanoparticles. However, the roughness of an extended surface is a property that is difficult to

translate to a nanoparticle, and such a "translation" has not been performed in ref. [133]. Also on Pt particles, in an in-situ Transmission Electron Microscopy (TEM) study[118], particle morphology variations have been observed that correlate with the oscillations. By employing mass transport simulations and DFT, the conclusion was drawn that the oscillations are the result of a bistability in the Langmuir-Hinselwood kinetics.

The interaction of oxygen with palladium nanoparticles has been studied on Fe_3O_4 substrates[134–136], on Al_2O_3[137, 138], and for epitaxially aligned particles on MgO[139], both at low and high O_2 pressures, and also in the context of CO oxidation. Nevertheless, oscillations in the CO oxidation rate on Pd nanoparticles have not been reported before.

7.2   Methods

In order to acquire as much structural information as possible, under actual, high-pressure, high-temperature conditions, we have employed a combination of four complementary structurally sensitive techniques, each under operando conditions.

High-pressure X-ray Diffraction (XRD) experiments have been conducted in the special, 17 ml flow-reactor setup that has been installed at the ID03 beamline of the European Synchrotron Radiation Facility (ESRF), especially for surface X-ray diffraction under catalytic conditions[22]. These experiments reveal which structural components, e.g. metal or oxide, are present. The same setup has been used to perform Grazing-Incidence Small-Angle X-ray Scattering (GISAXS) measurements on the Pd particles, which provides information on the average spatial arrangement of individual particles and is sensitive to the presence of e.g. core-shell structures[140].

A direct, real-space view of Pd nanoparticles under reaction conditions has been obtained with two in-situ microscopy techniques. We have conducted in-situ, non-contact Atomic Force Microscopy (AFM) experiments, using the new *ReactorAFM* setup with its 0.5 ml reactor volume, described in detail in chapter 2 and ref. [46]. These observations give information on the irreversible changes, such as ripening or sintering, and on reversible changes in the shapes and heights of the nanoparticles during reaction oscillations. The AFM observations have been complemented by extensive high-pressure TEM observations, where we have made use of the especially developed nanoreactors, which we also used in chapter 6 and which are described in refs. [13, 23]. The experiments were performed at 300 keV using an FEI Titan microscope at Delft University of Technology.

For the X-ray and AFM experiments, the nanoparticles had to be supported on a flat substrate. Samples with well-defined densities, ($100/\,\mu m^2$ for the AFM, $700/\,\mu m^2$ for the X-ray experiments), of size-selected Pd particles generated using

a spark discharge method (average diameter of 6 nm for AFM and 15 nm for the X-rays) supported on a flat $\alpha-Al_2O_3$ substrate, were kindly provided by Dr. M.E. Messing and Prof. K. Deppert and co-workers from Lund University in Sweden[40]. For the TEM experiments the nanoreactor was loaded with palladium nitrate salt. After oxidation with O_2 at 300°C and reduction by H_2 at 500°C, Pd nanoparticles had formed with sizes ranging from 5 to 50 nm.

Like the X-ray flow-reactor setup, the *ReactorAFM* operates in flow mode using a combination of mass flow controllers and back pressure controllers, typically operating with residence times of 5 to 20 seconds. The X-ray flow reactor has an adjustable leak to the UHV system which also contains the quadrupole mass spectrometer (QMS), resulting in gas composition measurement without any delay. For the *ReactorAFM*, the gas analysis is performed downstream by a (QMS-based) T100 analyser from LPM[120]. This configuration introduces a delay of a few seconds, but does not suffer from a loss in time resolution, thanks to the small volume of the input stage of the T100 analyser. However, the flow through a TEM nanoreactor is too small to be controlled with a commercial flow regulator, and the nanoreactors have been operated by defining a certain pressure of a gas mixture at the inlet and feeding the outlet directly into the differentially pumped ultra-high vacuum system (UHV) of a T100 analyser. Because of the micrometre-scaled dimensions of the nanoreactor, the pressure drops completely to zero over the length of the reactor, and the flow through the reactor can be handled directly by a turbomolecular pump. The second turbomolecular pump on the UHV system maintains the optimal working pressure for the QMS. The large volume of the capillary from the nanoreactor to the gas analyzer compared to the flow results in a time resolution for gas detection of approximately 30 s.

7.3 Results and discussion

In this section the experimental results are presented. We start with the crystallographic information derived from the XRD experiments. After addressing the particle shapes with TEM and AFM, we analyse the GISAXS patterns to obtain a detailed view of the rearrangement of the Pd nanoparticles during the catalytic reaction oscillations.

Although the different experimental techniques have been applied under different conditions, all data have been obtained close to the metal/surface oxide boundary, as indicated in figure 7.1.

7.3.1 X-ray diffraction

The upper panel of figure 7.2 shows the periodic variations in the CO_2 and CO partial pressures during spontaneous reaction oscillations on size-selected 15 nm Pd
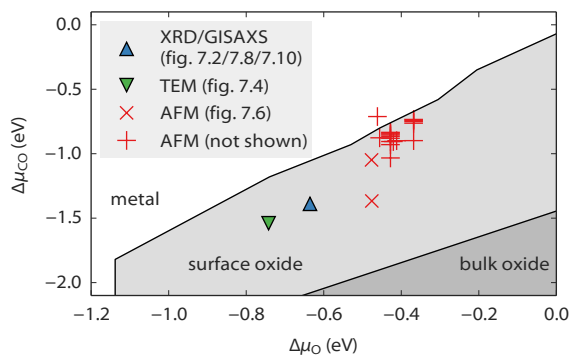
Figure 7.1. Experimental conditions of all experiments reported in this chapter, expressed in terms of the chemical potentials of carbon monoxide and oxygen. The three greylevels indicate three of the phases of a Pd(100) surface in contact with CO and O_2, as calculated using DFT by Rogal et al[141]. Since a nanoparticle exposes multiple different facets, it is to be expected that the phase boundaries for a nanoparticle system will be in slightly different positions. The phase boundaries will also shift and blur because of the CO oxidation reaction itself[142]. The two triangles correspond to observed reaction oscillations, indicating that these points are near a phase boundary, whereas only microscopy images but no reactivity data could be obtained for the cross markers.

particles on $\alpha-Al_2O_3$ in the 17 ml XRD flow cell. The nanoparticles were exposed to a constant gas flow of 60 ml_n/min consisting of CO, O_2 and Ar, at partial pressures of 9, 210, and 281 mbar respectively. The sample was heated at constant power to a temperature of about 588 K. The XRD measurements that were taken simultaneously with the mass spectrometry data exhibited periodic variations in the diffraction intensities at angles corresponding to either the crystal structure of metallic Pd or that of PdO. These variations were out of phase with each other; when the Pd signal was high, the PdO signal was low and vice versa. These oscillations were fully synchronised with those in the CO and CO_2 partial pressures. Figure 7.2 shows that the high-reactivity phase coincided with the presence of the oxide. The sample temperature varied in response to the changes in the turnover rate, since CO oxidation is an exothermic reaction. The oscillations had a period of a few minutes, depending on the temperature, and could be sustained indefinitely within the time scale accessible in our synchrotron experiments. The presence of the X-ray beam only quantitatively affects the oscillations: without the beam the oscillation period is a factor 2 longer and the amplitude of the temperature variations increases by 50%.

In addition to XRD, GISAXS experiments have been performed. Figure 7.2 shows that also the GISAXS signal varied synchronously with the reaction oscillation. These variations will be addressed in more detail in section 7.3.4.
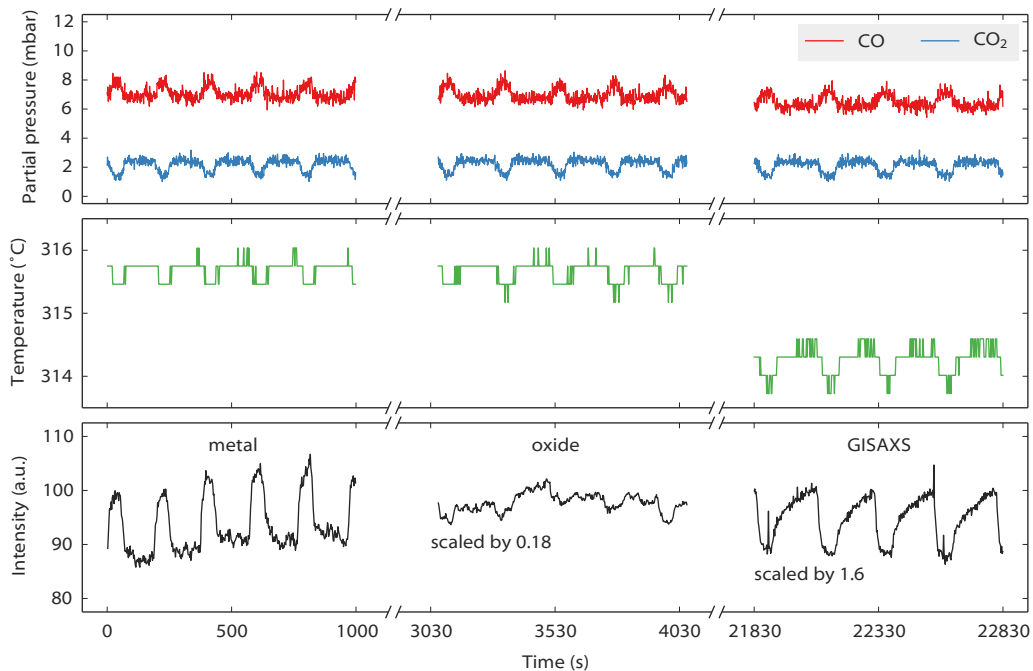
Figure 7.2. Spontaneous reaction oscillations observed using X-ray scattering. The upper panel shows the CO and CO_2 partial pressures as a function of time. The middle panel shows (a low resolution measurement of) the sample temperature. The gas feed was kept constant at 9 mbar CO, 210 mbar O_2, and 281 mbar Ar at a total flow of 60 ml_n/min, and the sample heater was operated at a constant power (its value was adjusted slightly around $t = 20\,000\,s$). Note that the absolute value of the partial pressures of CO and CO_2 contains an error due to varying background level for these gases in the mass spectrometer. The amplitude of the oscillations in these signals is not affected by this. The lower panel shows the periodic intensity variations in three different X-ray signals: the metal Pd peak at the $2\theta = 17.6°$ diffraction angle, the oxide PdO peak at $2\theta = 15°$ (see also figure 7.3), and the integrated intensity from a region in a series of GISAXS patterns (see figure 7.8). A high metal intensity is correlated with a low turnover rate, whereas a high oxide intensity correlates with a high turnover rate. Also the changes in the GISAXS signal are synchronised with the reaction oscillations.
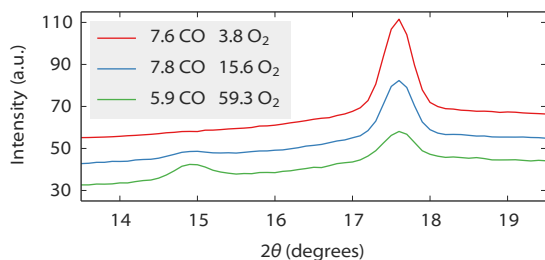
Figure 7.3. X-ray diffraction patterns of the Pd nanoparticles in three different mixtures of O_2 and CO at a total pressure of 200 mbar and a temperature of 375°C. The CO and O_2 partial pressures in mbar are indicated in the legend, the rest of the atmosphere consisted of argon. The patterns are offset by 10 a.u. for clarity. The peak at $2\theta = 17.6°$ corresponds to the (111) reflection of metallic Pd, $2\theta = 15°$ corresponds to the (101) reflection of the oxide PdO.

7.3.2 Transmission electron microscopy

In-situ TEM has been used to obtain a direct view in real space of Pd nanoparticles during oscillations in CO oxidation at atmospheric pressures and elevated temperatures.

In the employed configuration of nanoreactor gas lines, QMS system and vacuum pumping, the residence time of gas in the 0.4 nl reactor was less than 1 ms, and the sensitivity of the reaction product detection was sufficient to measure CO conversion, although the time resolution was only about 30 s, due to diffusive mixing of the gases between reactor and mass spectrometer. In addition to reactivity measurements, the TEM nanoreactor allows sensitive calorimetric measurements with a time resolution of 0.5 s, and this was our primary detection method for the oscillations. The reactor was operated at constant temperature using an electronic feedback circuit, and since the CO oxidation reaction is exothermic, the high-reactivity regime corresponded to lower power input from the sample heater, while the low-activity regime corresponded to higher heating power.

When operating at elevated temperature, there were large temperature gradients in the region around the electron-transparent windows that need to be taken in consideration. Measurements on an earlier version of the nanoreactor[143] and simulations on the current version[118] showed that when operating the heater at a setpoint of 723 K, the center of the heated region was typically 50 K hotter, while the electron-transparent windows, which are situated near the edge of the heated zone, were typically 100 K colder than the value measured from the resistance of the heater.

The nanoreactor was loaded with 5 to 50 nm nanoparticles, as described in section 7.2. When exposing these particles to a mixture of 33 mbar CO and 217 mbar O_2 at temperatures near 400°C, spontaneous reaction oscillations occured as can
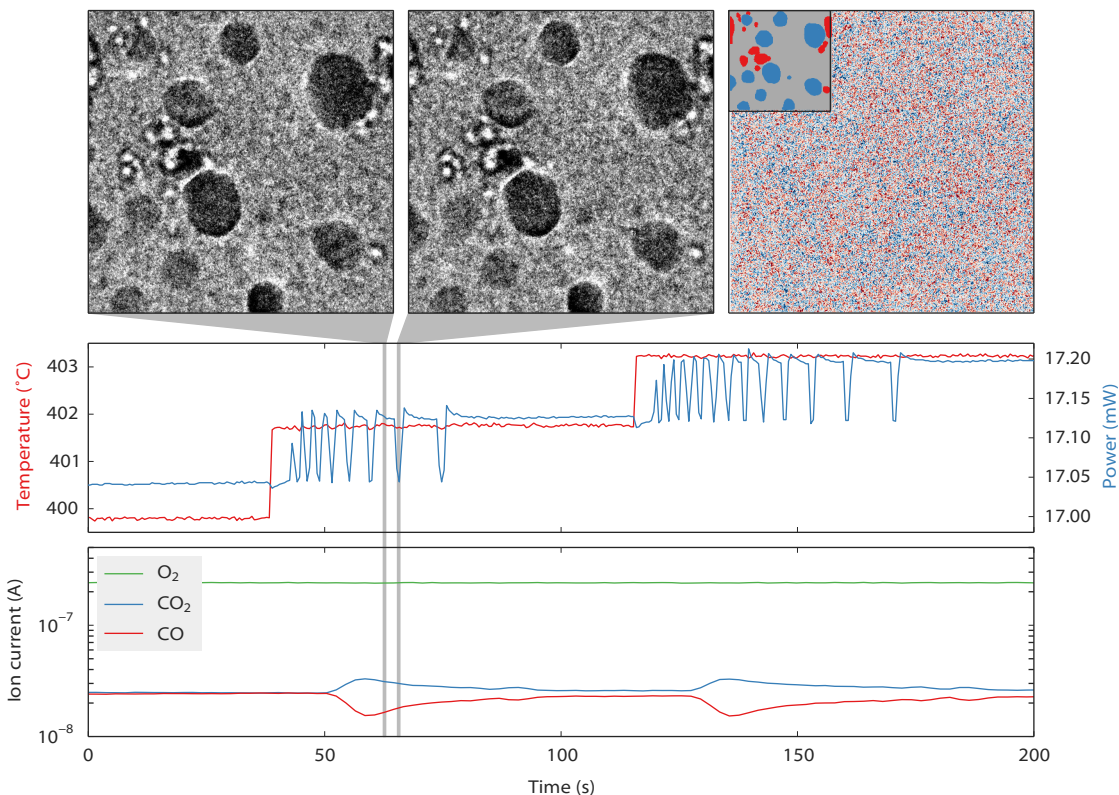
Figure 7.4. (Upper panels) TEM observations during reaction oscillations, 98×98 nm^2 field of view. The first image was taken in the low-reactivity regime, and the second image, which was taken 3 s later than the first, was taken in the high-reactivity regime. The third image shows the difference image (after drift correction) between the first and second image, with the inset indicating in blue the particles that were in focus, and in red the particles on the other window of the nanoreactor that were out of focus. (Middle panel) Sample temperature and required heating power. After both temperature steps, the system exhibited a finite number of reaction oscillations, as can be read off from the heating power variations. (Lower panel) Mass spectrometry signals. The time resolution of the gas detection system was not good enough to resolve the oscillations, even though the partial pressures of CO and CO_2 do reflect the average effect of a burst of oscillations, at $t = 40$ and $t = 120$ s.
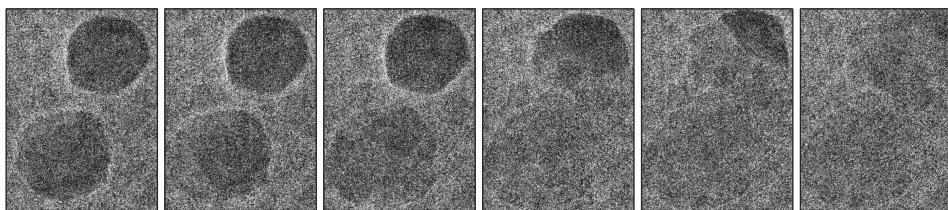
Figure 7.5. Bulk oxidation of Pd particles in 250 mbar O_2 at 400°C, imaged with 30 e/Å^2 s. A single oxidation front passed through both particles. Note the reduced contrast after oxidation due to the lower density of PdO with respect to that of pure Pd. Each image measures 33×44 nm^2.

be seen in the time dependence of the heater power shown in figure 7.4.

In contrast to the X-ray experiments, the oscillations could not be sustained for prolonged times. After the oscillations started, either spontaneously or triggered by a small temperature increase in the order of 1 K, the system continued oscillating for at most several minutes. Typically, the period of the oscillations continuously increased from 2 to 15 seconds over the course of 10 to 100 periods, before coming to a halt in the low-reactivity regime. We attribute the shorter period and the reduced lifetime of the oscillations compared to those in the SXRD reactor to the higher temperature in the TEM experiments, as the processes that determine the time scale of the oscillations (for the Pd(100) surface these were the roughening and annealing), are likely to take place at a faster rate at the higher temperature. Also the wider particle size distribution could play a role, as these processes might come to a halt earlier on small particles causing the system to switch to the other regime.

Figure 7.4 shows two TEM images of Pd particles in a downstream window, taken in consecutive low- and high-reactivity phases. The difference image shows absolutely no features above the noise. This shows that the TEM images cannot resolve any changes in the particle morphology. Due to the low signal-to-noise ratio of the particles on the speckled background (from the amorphous SiN nanoreactor windows), and due to the Fresnel scattering halo around each particle perimeter, the effective resolution in our images was limited to values not better than 0.5 nm for metallic Pd, and 1 nm for PdO, due to its lower density.

The images in figure 7.4 have been taken with an electron flux of 30 e/Å^2 s. Higher current densities have been observed to inhibit bulk oxidation of Pd, but we have verified that at the current density of our experiment the Pd particles could oxidise completely in pure oxygen (figure 7.5).

Due to the existence of large temperature gradients in the reactor, it is possible that the region imaged in these experiments was actually not participating in the reaction oscillations. The central hot region might have been oscillating, while the particles downstream of the hot zone and (which experience nearly the same

gas conditions but are at 100-150°C lower temperature), might have behaved differently. Unfortunately, there were no electron-transparent windows in the hot zone. Also, no difference has been observed between particles in windows upstream and downstream of the hot zone.

7.3.3   Atomic force microscopy

Whereas TEM gives high-resolution cross-sectional information on the nanoparticles, height information is mostly inaccessible. In addition, the Pd particles in the nanoreactor were supported on the SiN windows, while Al_2O_3 has been used as the support for the Pd particles in the XRD and GISAXS measurements. We have used the *ReactorAFM*, introduced in chapter 2, to obtain in-situ real-space observations on a sample of Pd particles similar to the one used for the XRD and GISAXS measurements, but with a smaller particle diameter of 6 nm and lower coverage of 100 particles/ μm^2. Unfortunately, due to this low Pd coverage it was not possible to measure the turnover rate with mass spectrometry. Calorimetry was also not possible because of the large thermal mass of the sample and sample mounting structure compared to the heat of reaction. Therefore, we cannot be sure whether the reaction was oscillating under the conditions of our AFM observerations.

Figure 7.6 shows an ensemble of Pd particles imaged by non-contact AFM in two different atmospheres and at high temperatures, in both cases close to the phase boundary between metal and surface oxide (figure 7.1). For these images, the rms-roughness of the line profiles on the Al_2O_3 substrate was taken as a measure for the vertical resolution, and this was found to be 0.2 nm. Within this margin, the particle heights did not change when the atmosphere was changed. The horizontal resolution was limited due to convolution of the particle contours with the tip shape, therefore a systematic analysis of the lateral particle shape has not been attempted.

Summarizing the real-space observations of TEM and AFM, it can be concluded that the particles remained largely unchanged. In particular, we can conclude that the particles did not get fully oxidised under reaction conditions. Neither have other effects such as fragmentation, clustering, or particle migration been observed as a direct consequence of the switch from one gas composition regime to the other.

7.3.4   Grazing incidence small angle X-ray scattering

The GISAXS data have been obtained at the ID03 beamline of the ESRF operating at 18 keV using a Maxipix 2D-detector. To optimise the signal-to-noise ratio the GISAXS data have been averaged in the following way. GISAXS patterns have been acquired continuously during several consecutive periods of the reaction oscillation. Each period has been manually segmented into 12 sections, based on the phase of the oscillation using the CO_2 signal as reference and on the intensity in a 20-pixel region
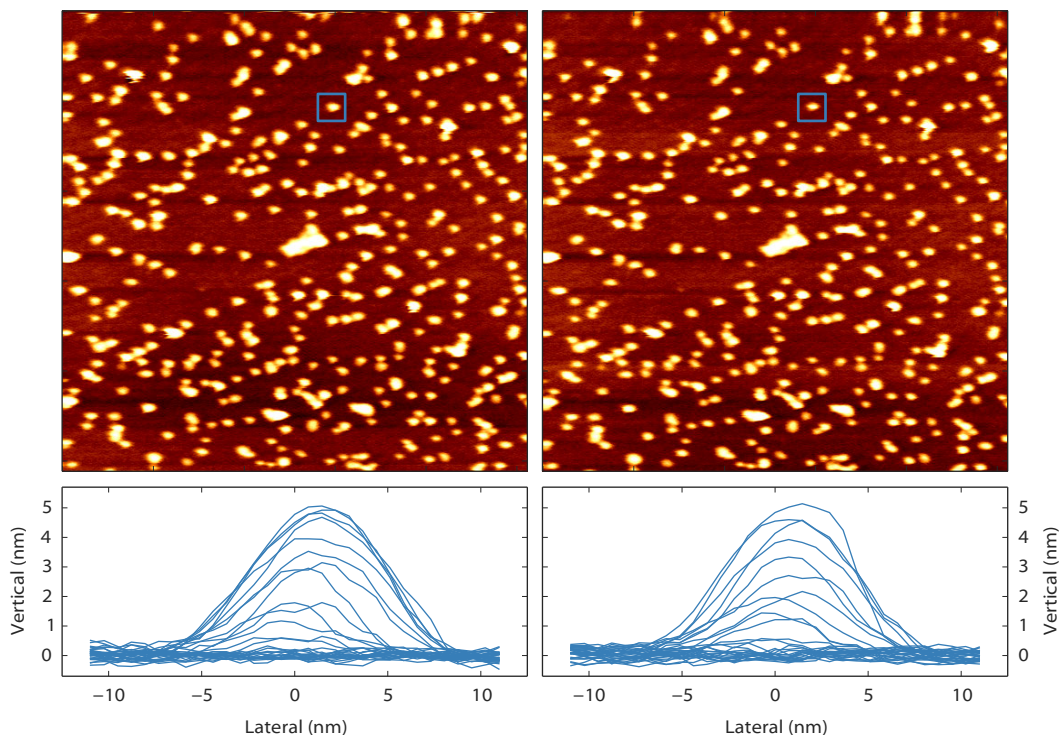
Figure 7.6. The upper panels show $700 \times 700 \ \text{nm}^2$ non-contact AFM images on size-selected Pd particles supported on $\alpha-\text{Al}_2\text{O}_3$, obtained at 475 K and a total pressure of 1 bar. The coverage is about 100 particles/ μm^2, but the particles are distributed inhomogenously over the surface, giving rise to a higher coverage in the region imaged here. The left panels have been obtained in a 1:3 Ar:O_2 mixture, the right panels in a 10:1:30 Ar:CO:O_2 mixture. The AFM was operating in frequency modulation mode with a frequency shift setpoint of +5 Hz and an oscillation amplitude of 5 nm. The lower panels each show 30 horizontal line profiles from the regions indicated by the blue rectangles in the images, proving that the particle height did not change. The cross-sectional particle shape has not been analysed in detail, as it is formed by the convolution of the tip shape with the particle shape.
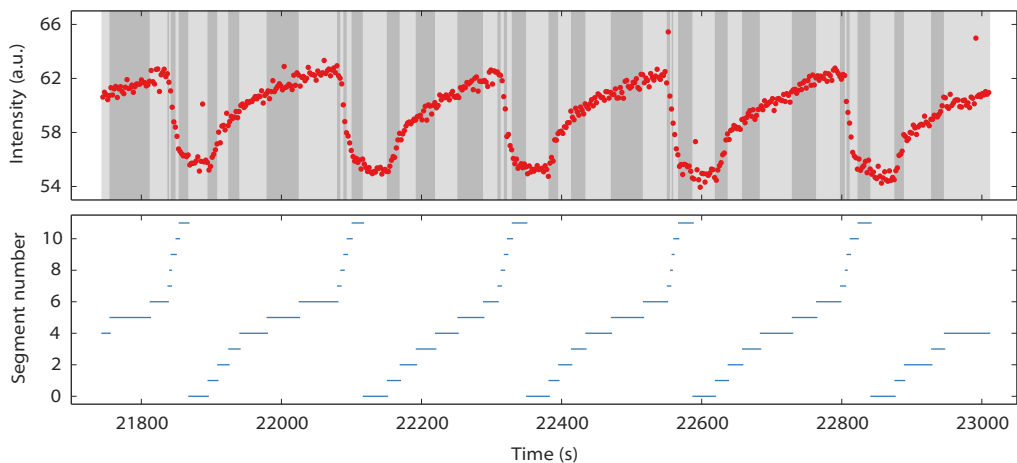
Figure 7.7. The upper panel shows the GISAXS intensity integrated from a small region near the Yoneda peak (see figure 7.8 for details) versus time during five full oscillation cycles. The lower panel and the grey bands in the upper panel show how we have manually classified all GISAXS data into 12 epochs, 6 for the parts of the oscillation cycle during which the GISAXS intensity increased, and 6 for the decreasing parts. In this way, the full data set with multiple oscillations was averaged into a combination of 12 GISAXS patterns, with good signal-to-noise characteristics, together covering the complete oscillation cycle. These 12 patterns were used for the subsequent analysis.

close to the center of the Yoneda peak in the GISAXS pattern. This segmentation is illustrated in figure 7.7. All data within each segment (irrespective of the period it belonged to) was taken together and averaged. Two horizontal lines from the 2D-detector (each line has a width of 0.05 mrad) that cut through the Yoneda peak (as indicated in figure 7.9) were used for a detailed analysis as described below.

The GISAXS pattern showed an intensity that was oscillating along $q_\parallel$ in the low-reactivity phase, and a more monotonic profile in the high-reactivity phase (figure 7.9). This change in profile can be interpreted as a change in the abruptness of the electron density profile as a function of radius (figure 7.9). The oscillations are the result of a sharp transition in electron density from metal to vacuum, whereas a broadening of this transition blurs these oscillations. The broadening can be caused by a less compact particle shape (i.e. facets rather than sphere), a wider particle size distribution, or by the formation of a surface layer with a lower electron density. From the GISAXS patterns alone it cannot be concluded which of these three scenarios is at work.
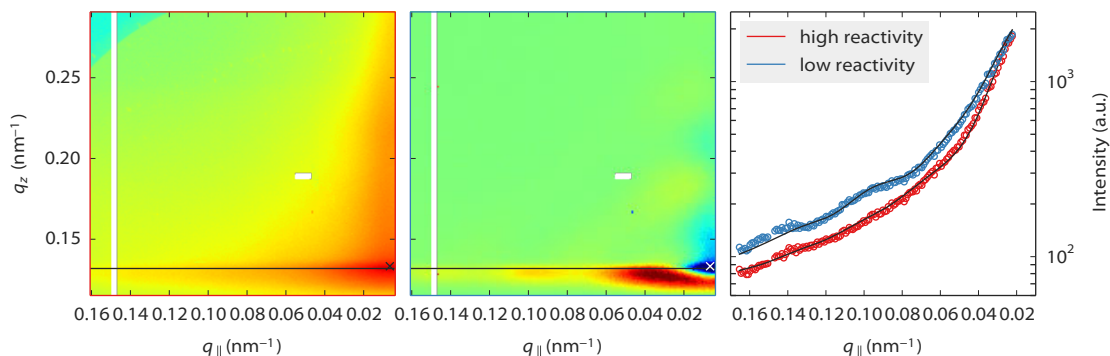
Figure 7.8. GISAXS data after averaging, (left panel) in the high-reactivity regime (logarithmic colour scale), (middle panel) difference signal between the intensity in the low-reactivity regime and that in the left panel, (right panel) linescans through the GISAXS data in the high- and low-reactivity regimes at the location indicated in the left and middle panels. The blue and red curves are the theoretical fits discussed in the text and explained in figure 7.9. The crosses in the lower right of the two GISAXS patterns indicate the location of a 20 pixel ($5 \cdot 10^{-5}$ steradian) region that was integrated to obtain the signal that is shown in figures 7.2 and 7.7.

7.4 Model and interpretation

Having discussed the four sets of experimental data (section 7.3), we now combine all evidence into a consistent model and test this model with numerical fits to the GISASX data in figure 7.8. There were three competing scenarios for the changing electron density profile. A changing particle distribution can be ruled out because the changes were fully reversible (hence the oscillations), and the particle distributions remained also unchanged in the TEM and AFM images. Also faceting is not observed in TEM or AFM. On the other hand, the presence of a PdO oxide was observed in the high-reactivity phase with XRD, in combination with a reduced amount of metallic Pd. The only configuration that is consistent with all these pieces of evidence is one in which an ensemble of relatively compact, metallic Pd nanoparticles is changed into core-shell structures with a Pd core and a thin palladium oxide shell, both under the influence of the deliberate changes in the gas atmosphere (from reducing to oxidizing), and repeatedly during spontaneous reaction oscillations. The electron density of the oxide is lower than that of the metal, hence the blurring of the electron-density profile at the particle-gas interface. When the oxide shell is sufficiently thin, it should be hard to distinguish it in the TEM and AFM images under reaction conditions.

For our numerical fits, we modelled the Pd particles as truncated core-shell spheres on a flat substrate. The core was taken to be metallic (Pd), the shell to be PdO, and the substrate was set to alumina (Al_2O_3). Only three degrees of freedom
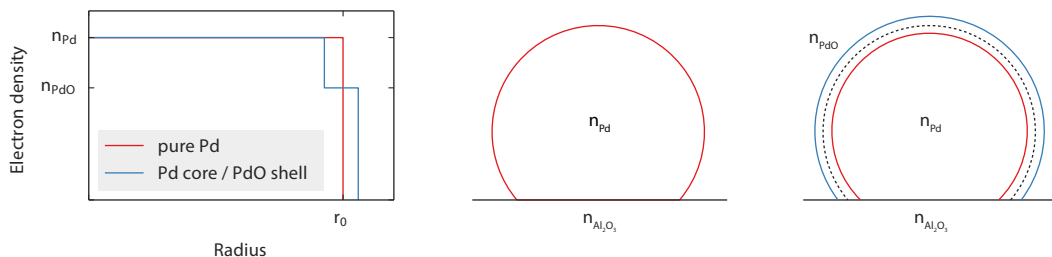
Figure 7.9. The presence of the oscillations along $q_\parallel$ in the line profiles in figure 7.8 correspond to sharp transitions of electron density n from metal to vacuum (as sketched for the pure Pd particle in the left panel). The blurring of these oscillations corresponds to a broader electron density profile. The electron density transition is influenced by particle morphology (e.g. faceted versus spherical shape), particle size distribution, and chemical composition (e.g. $n_{PdO} < n_{Pd}$). The model used to fit the GISAXS patterns is that of a spherical core-shell particle on a flat Al_2O_3 substrate having a Pd metal core and a PdO oxide shell (middle, right panels). The fits have been made assuming all variations in the electron density profile can be attributed to changes in the thickness of the oxide shell, while all other parameters (number of Pd atoms per particle, particle size distribution, truncation of sphere) have been forced to adopt constant values throughout the entire oscillation period.

were left in the fit, namely the oxide shell thickness, the total number of Pd atoms per particle, and the parameter quantifying the truncation of the sphere (figure 7.9).

The GISAXS patterns were computed using a formalism for dilute core-shell nanoparticles on a substrate, based on the Distorted Wave Born Approximation[140]. In this approach, particles are treated individually, i.e. there is no scattering process involving multiple particles. To verify that this approximation is appropriate, scanning electron microscopy (SEM) images have been taken of a sample treated similarly to the one analysed here, but with a SiO_2/Si substrate. From these SEM images, the interference function was calculated and this was found to be sufficiently uniform to treat the particles independently in the GISAXS analysis. The Si substrate is not expected to give rise to a significantly different interference function than a Al_2O_3 substrate, and the latter is difficult to image with SEM.

We have developed special Python code in order to fit multiple GISAXS patterns simultaneously, with several shared parameters. This has enabled us to fit the 12 epochs in the average oscillation period in a single step, in which we only allowed the thickness of the oxide shell to vary from epoch to epoch, while forcing the number of Pd atoms per particle and the truncation of the sphere to adopt constant values throughout the entire oscillation period. In this way, internal consistency was ensured and convergence was facilitated, something that could not be done with previously existing software such as IsGISAXS[144].

Since the nanoparticles were not identical but varied slightly in size, each of the three fit parameters was assumed to follow a Gaussian distribution. These
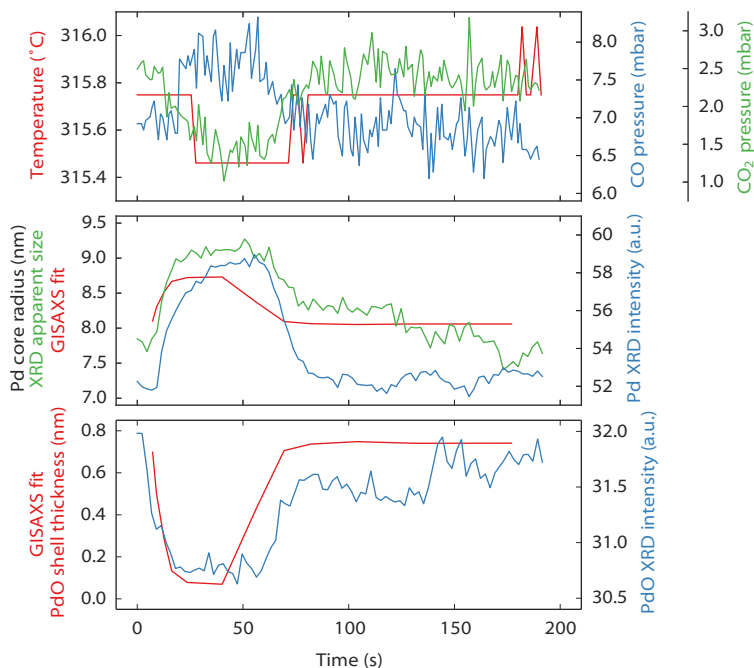
Figure 7.10. Reactivity, GISAXS and XRD data presented over a single oscillation period. Since it was not possible to acquire this complete dataset simultaneously, some curves derive from different periods while the system was oscillating. In particular, the gas composition and sample temperature were measured simultaneously with the Pd metal XRD peak, while the oxide XRD peak and the GISAXS signal were obtained separately. For the GISAXS fit procedure, data from multiple oscillations have been averaged to increase the signal-to-noise ratio (see figure 7.7). To compensate for the slightly different lengths of the periods, the oxide signal has been scaled by 0.978 along the time axis, the GISAXS signal was scaled by 0.789. The apparent particle size from XRD was estimated from the Full Width at Half Maximum (FWHM) of the Pd peak[145], assuming a perfect spherical shape.

distributions were approximated by seven points linearly distributed from $\mu - 2\sigma$ to $\mu + 2\sigma$ and weighted by their relative values of the probability density function. In this way, each simulated GISAXS pattern was constructed as the incoherent sum of 7^3 patterns. A least-squares optimization was then performed on the 28 free parameters (the number of Pd atoms and a sphere truncation parameter, which are kept constant during the 12 phase segments, and a shell thickness for each of the 12 phase segments; all parameters have a mean and standard deviation).

Figure 7.8 shows that the simulated GISAXS patterns obtained with this optimization procedure gave a good fit of the raw data. Figure 7.10 combines the XRD and GISAXS data for an entire period of the spontaneous reaction oscillation. The GISAXS fits are in excellent agreement with the XRD data. Both data sets show that

the high-reactivity phase coincides with the presence of an oxide shell of approximately 1 nm thickness. The corresponding decrease in metal core size, demanded by the fit constraints, matches the decrease in scattering volume corresponding to the reduction in Pd diffraction intensity, while the increase in PdO volume matches the growth in PdO diffraction intensity. Independent confirmation for the reduction of the size of the Pd core during the high-reactivity phase comes from the increase in angular width of the XRD peak from the Pd, which is a direct, inverse measure of the average size over which the metallic component of each nanoparticle extends (figure 7.10, middle panel).

We were unable to get a good fit for the out-of-plane intensity profile of the GISAXS patterns. This could be due to an interface layer between the Pd particle and the Al_2O_3 substrate[138].

7.5   Oscillation mechanism

The periodic formation of the oxide shell seems to indicate a direct analogy to the oscillations observed on the single-crystal surfaces of Pd. However, the observations presented in this chapter provide no information on the feedback mechanism that drives the oscillation on the nanoparticles. Surface roughness played the role of "hidden parameter" on the single crystals, and the roughness-dependent stability of the PdO was the non-linear component required for oscillation. By contrast, TEM and AFM images showed no morphology variations on the nanoparticles. However, roughness on a sub-nm scale, which should be the scale for a nm-thick oxide, would be very difficult to observe, given the resolution of the microscopy images under high-pressure, high-temperature conditions. In addition, roughness can take several forms, ranging from steps on nanoparticle facets (the direct analogue of roughness on single-crystal surfaces), to intermediate surface orientations appearing between the dominant (100) and (111) facets, up to a complete rounding of the particles and a disappearance of the facets. Again, the TEM and AFM images can only be consistent with very modest changes in particle morphology.

Apart from the scenario where roughness is the hidden parameter, we can think of two other candidates for this parameter, although in both cases it is unclear what the non-linear component would be. The first scenario relates to the ongoing discussion about the activity of the PdO, as it is well established that the presence of the palladium oxide correlates with the high-reactivity phase[131, 146], but it is still under debate whether the increased activity should be attributed to the oxide or the oxide should be regarded as a mere consequence of the lower CO partial pressure due to the increased turnover of CO by the metal phase[137, 141, 142, 147–150]. In the latter case, the poisoning of the palladium particles could be the hidden parameter. What speaks somewhat against this scenario is the observation in figure 7.10 that

during the high-reactivity phase neither the thickness of the oxide layer, nor the total amount of PdO seems to increase, which is to be expected for this layer in the self-poisoning scenario. The second possibility for an alternative scenario could be related to the formation of an interfacial PdO layer between the metal particle and the Al_2O_3 substrate[138], which could have a large influence on the activity of the system.

7.6   Conclusion and outlook

Spontaneous reaction oscillations occur during CO oxidation over Pd nanoparticles. These oscillations are accompanied by the periodic formation and reduction of a thin oxide shell on these particles. Further research is required to establish the mechanism of the reaction oscillations. Improved resolution of the in-situ microscopy techniques would be helpful, as this is required to reveal the small morphology variations that probably occur and influence the stability of the oxide. This would establish a key piece of evidence in support of the nanoparticle analogue of the mechanism found for single crystals[131]. Better resolution could be achieved by more stable and sharper tips for the *ReactorAFM*, e.g. made from diamond[151], and by better windows of the TEM nanoreactors, causing less electron scattering, e.g. in the form of 2D-materials such as graphene[152].

   Even though this work adds to the debate on the activity of PdO, it cannot pinpoint the cause of the high activity during the presence of the oxide. Recent theoretical work is close to addressing this question for the flat surfaces[142, 149]. The observations presented in this chapter show that this issue is also relevant for nanoparticles, and thus for more realistic catalytic systems.

De Senaatskamer in het Academiegebouw van de Universiteit Leiden[153].

Samenvatting

Deze samenvatting is toegankelijk voor een breed publiek. Er zijn daarom vrijwel geen bronvermeldingen opgenomen. De wetenschappelijk geïnteresseerde lezer wordt verwezen naar de Engelstalige introductie in hoofdstuk 1.

Aan het begin van de twintigste eeuw raakten twee nieuwe richtingen binnen de natuurwetenschappen in een stroomversnelling. De ontdekking van een proces om kunstmest te maken, het Haber-Bosch proces, markeert de start van de grootschalige chemische industrie. En na de uitvinding van de gloeilamp blijkt dat er nieuwe natuurkunde begrepen moet worden om betere peertjes te kunnen maken. Op het eerste gezicht zijn dit ontwikkelingen die niks met elkaar te maken hebben, maar nu, honderd jaar later, kunnen nieuwe technieken deze twee onderzoeksgebieden samenbrengen. Dit kan verrassende inzichten opleveren, en dit proefschrift draagt daar een steentje aan bij.

In 1909 ontdekte Fritz Haber een manier om stikstof uit de lucht om te zetten in ammonia, een basisingrediënt voor kunstmest. Samen met Carl Bosch schaalde hij dit in een paar jaar tijd op tot een industrieel proces en veroorzaakte daarmee een revolutie in de landbouw. Momenteel is de productie van kunstmest verantwoordelijk voor 1% van het wereldwijde energieverbruik en zorgt het gebruik ervan voor een derde van de wereldvoedselproductie. Het Haber-Bosch proces, vernoemd naar de uitvinders, was de eerste grote toepassing van katalyse, een type chemische reacties waarbij een bepaalde stof (de 'katalysator') meedoet maar niet verbruikt wordt. Tegenwoordig vormt katalyse de basis van bijna alle grootschalige chemische processen, bijvoorbeeld bij de productie van kunststoffen en brandstoffen, en vindt het ook toepassing dichter bij huis in de autokatalysator voor de zuivering van uitlaatgassen.

De opkomst van de gloeilamp zorgde voor een andere belangrijke ontwikkeling. Een gloeilamp bestaat uit een dun draadje, dat zeer heet wordt (2000 tot 3000°C) doordat er een elektrische stroom doorheen loopt. Hierdoor gaat het draadje gloeien en dit geeft licht. In lucht gaat zo'n gloeidraadje direct kapot, doordat het reageert met zuurstof. De innovatie van de gloeilamp is dat je het gloeidraadje beschermt met een glazen bolletje, waar je zoveel mogelijk lucht uit haalt door het vacuüm
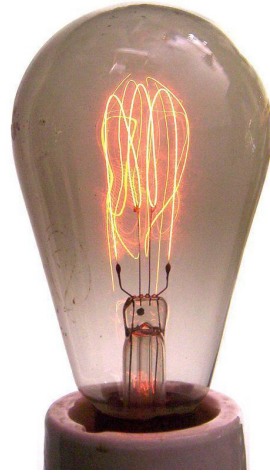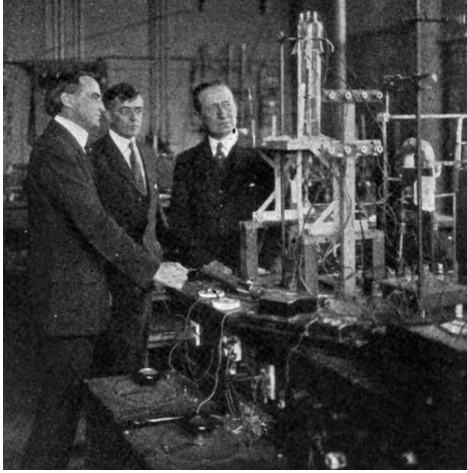
Figuur 1. Radiopionier Guglielmo Marconi (rechts) op bezoek bij Irving Langmuir (midden) in zijn lab bij General Electric, met links GE-directeur William R. Whitney[154]. De rechterfiguur toont een oude gloeilamp met een gloeidraadje van koolstof[155]. De levensduur van de lamp is beperkt doordat het koolstof uit de draad langzaam verdampt en op het glas neerslaat, waardoor het draadje steeds dunner wordt en uiteindelijk breekt.

te zuigen. De levensduur van een gloeilamp hangt voor een belangrijk deel af van wat er precies gebeurt met het gloeidraadje en het restje lucht dat nog in de lamp zit. Irving Langmuir is dit systematisch gaan onderzoeken bij lampenfabrikant General Electric. Hij ontdekte o.a. dat je beter een beetje edelgas in de gloeilamp kunt hebben dan een restje lucht. Met zijn werk heeft hij de basis gelegd van de oppervlaktefysica, het vakgebied dat zich tot op de dag van vandaag bezig houdt met o.a. metaaloppervlakken en de interactie van gassen daarmee. In 1932 kreeg Langmuir de Nobelprijs voor de Scheikunde voor zijn bijdragen op dit gebied.

Deze twee ontwikkelingen hebben meer met elkaar gemeen dan misschien op het eerste gezicht duidelijk is, want in feite gaat het in beide gevallen over de wisselwerking tussen metalen en gassen. Een katalysator bestaat namelijk vaak uit een heel fijn metaalpoeder. De deeltjes in dit poeder zijn tot een miljoen keer kleiner dan een millimeter en worden nanodeeltjes genoemd. Het poeder wordt verspreid over een poreus keramisch materiaal om te voorkomen dat het samenklontert. Deze keramische drager wordt samengeperst in korrels en wordt dan in grote reactorvaten gestopt. De grondstoffen voor de reactie worden als gas of vloeistof door de reactor geperst en stromen langs de katalysator, meestal bij temperaturen van een paar honderd graden. Als je de juiste katalysator bij de juiste omstandigheden gebruikt komt er aan de andere kant van de reactor het gewenste product uit.

De kern van zo'n katalyseproces is de wisselwerking tussen gas (of vloeistof) en metaalpoeder, en dit is precies het onderwerp dat Irving Langmuir bij de gloei-

Figuur 2. Katalyse op industriële schaal. Links een aantal katalysatoren; te zien zijn de poreuze keramische korrels die geïmpregneerd zijn met heel kleine metaaldeeltjes[156]. Rechts de reactorvaten van een PVC kunststoffabriek, die zijn gevuld met dit soort korrels[157].

lampen bestudeerde. In een industrieel katalyseproces komt echter nog veel meer kijken (Hoe moet zo'n reactor er uit zien, welke vorm van de keramische korrels werkt het best, hoe snel moet alles door de reactor stromen? Enzovoort), maar de belangrijkste vraag — wat gebeurt er precies rondom de metaaldeeltjes — is voor de meeste katalyseprocessen nog niet beantwoord.

Nieuwe ontwikkelingen na een eeuw aan onderzoek

De afgelopen honderd jaar is geprobeerd antwoorden op de laatste vraag te vinden. De moderne aanpak, van bijvoorbeeld de laatste twintig jaar, maakt gebruik van nanotechnologie, waarmee het mogelijk is om individuele atomen en moleculen (de bouwstenen van alle materialen, en chemische en biologische stoffen) te bekijken en te manipuleren. Dit is zeer succesvol geweest en heeft kennis opgeleverd over het gedrag op de atomaire schaal van een heel scala aan materialen. Dit soort experimenten vindt plaats onder zeer precies gecontroleerde, ideale omstandigheden met complexe apparatuur in een laboratorium. Het is heel moeilijk om op basis daarvan een beeld te vormen wat er gebeurt onder veel agressievere omstandigheden zoals in een reactorvat. En dat is juist informatie waar de chemische industrie veel aan zou hebben.

Het werk dat in dit proefschrift beschreven wordt is een balanceer-act tussen twee benaderingen: aan de ene kant wil je geweldig gedetailleerde informatie krijgen, die eigenlijk alleen bij model-omstandigheden te verkrijgen is, aan de andere kant

wil je dit doen onder relevante condities, dus niet te ver geïdealiseerd. Wereldwijd zijn er diverse universiteiten bezig om nieuwe meettechnieken hiervoor te ontwikkelen of bestaande technieken aan te passen. Zo ook aan de Universiteit Leiden, waar een groot deel van dit proefschrift tot stand is gekomen. Verder hebben we nauw samengewerkt met de TU Delft, waar men voorop loopt op het gebied van extreem kleine chemische reactoren die in een elektronenmicroscoop passen. Tot slot hebben we experimenten gedaan bij de European Synchrotron Radiation Facility (ESRF) in Grenoble, Frankrijk. In dit Europees onderzoeksinstituut wordt een deeltjesversneller gebruikt om zeer intense röntgenstraling te maken, waarmee je vervolgens allerlei bijzondere experimenten kunt doen.

Aan de Universiteit Leiden hebben we 's werelds eerste atomaire-kracht-microscoop (AFM) ontworpen en geconstrueerd waarmee je tijdens een chemische reactie zichtbaar kunt maken wat er gebeurt. Atomaire-kracht-microscopen gebruiken een heel scherp naaldje om lijn voor lijn een oppervlak af te tasten. Door de kracht te meten tussen het naaldje en het oppervlak kun je een plaatje maken waarop de individuele atomen in het oppervlak te zien zijn. Dit type microscoop is zo'n 30 jaar geleden uitgevonden, maar de ontwikkeling richtte zich tot nu toe ofwel op geweldige prestaties onder ideale omstandigheden (bijvoorbeeld met steeds meer detail individuele atomen afbeelden), ofwel op gebruiksgemak voor een breed scala aan eenvoudigere metingen (bijvoorbeeld voor gevoelige krachtmetingen aan biologische moleculen). Hoofdstuk 2 beschrijft de ReactorAFM, de microscoop die wij ontwikkeld hebben voor de katalyse-metingen (AFM staat voor atomic force microscope). De ReactorAFM levert geweldige prestaties onder omstandigheden die heel veel lijken op de woeste omstandigheden in de chemische industrie. Gebruiksgemak is natuurlijk geen vereiste als je grenzen wilt verleggen...

Apparatuur is tegenwoordig niet meer los te zien van software om die apparatuur aan te sturen en om meetgegevens te verwerken. Hoofdstukken 3 en 4 beschrijven computerprogramma's die we ontwikkeld hebben en die nu een vast onderdeel geworden zijn van respectievelijk het katalyse-microscopie-lab in Leiden en de ID03 bundellijn van het European Synchrotron Radiation Facility.

Het tweede deel van dit proefschrift gaat over het toepassen van dit soort nieuwe meettechnieken om meer begrip te krijgen over twee chemische reacties, die beide plaatsvinden in een autokatalysator. Sinds het begin van de jaren negentig zit in elke Europese auto een katalysator, die er voor zorgt dat de giftige stoffen in de uitlaatgassen omgezet worden in minder schadelijke stoffen. Dit heeft enorm bijgedragen aan het verbeteren van de luchtkwaliteit in de grote steden. De autokatalysator pakt drie soorten vervuilers aan: onvolledig verbrande koolwaterstoffen, diverse stikstofoxiden, en koolmonoxide. Hoofdstukken 5 en 6 gaan over NO, een stikstofoxide, en hoofdstuk 7 gaat over koolmonoxide of CO. Uit deze hoofdstukken blijkt dat de balanceer-act van onze ontwikkeling van nieuwe apparatuur goed heeft uitgepakt,

en dat we hierdoor unieke informatie hebben kunnen krijgen.

Hoofdstuk 5 beschrijft wat er gebeurt als een heel zuiver en supervlak stukje platina blootgesteld wordt aan NO en waterstof (H_2). De omzetting van het giftige NO naar het onschadelijke stikstof of N_2 is tamelijk complex, omdat er niet één reactie speelt maar meerdere, die elkaar ook nog eens tegenwerken. Voor je het weet, zet je NO om in ammonia, en dat is net zo slecht voor het milieu als NO zelf. Daar komt bij dat NO ook allerlei materialen aantast en zomaar onderdelen van je meetopstelling kapot kan maken. Desondanks hebben we met de röntgenstralen van de ID03 bundellijn in Grenoble kunnen zien dat het vlakke platina-oppervlak opbreekt in kleine facetten die zo'n 10 graden scheef staan ten opzichte van het oorspronkelijke oppervlak. De oorzaak hiervan is de grote hoeveelheid NO die aan het platina hecht, waardoor het oppervlak beïnvloed wordt. In hoofdstuk 6 gebruiken we de Delftse elektronenmicroscoop om te kijken naar platina nanodeeltjes. Van zichzelf hebben platinadeeltjes een geometrische vorm met zeer rechte zijkanten, een beetje zoals een voetbal gemaakt is van verschillende vlakjes leer. Met de elektronenmicroscoop zien we dat de rechte zijkanten verdwijnen als er NO op het oppervlak komt, en ze worden vervangen door een gekromd oppervlak. Dit is vergelijkbaar met wat we het hoofdstuk ervoor beschreven: vlakke platina oppervlakken verdwijnen onder invloed van NO, en we schrijven dit dan ook toe aan hetzelfde effect van het aanhechtende NO.

In hoofdstuk 7 wordt beschreven wat er gebeurt als CO en zuurstof (O_2) bij zo'n 400°C in contact komen met nanodeeltjes van het metaal palladium. Het resultaat van deze reactie is dat het giftige CO wordt omgezet in het veel minder schadelijke broeikasgas CO_2. Maar wat nog niet bekend was, is dat als de hoeveelheden CO en O_2 een bepaalde verhouding hebben, de katalysator dan vanzelf heen en weer schakelt tussen twee toestanden. Dit soort 'oscillaties' zijn bekend in allerlei chemische systemen, maar waren nog niet eerder ontdekt in deze specifieke combinatie van CO, O_2 en palladiumdeeltjes. Wat echter nog veel bijzonderder is, is dat het ons ook gelukt is om een belangrijk stuk van het mechanisme van de oscillaties te begrijpen. Het blijkt dat in de ene toestand de palladiumdeeltjes een dun oxide-huidje hebben, en dat de deeltjes dan heel effectief zijn in het omzetten van CO. Op een gegeven moment verdwijnen de oxidelaagjes en zijn de palladiumdeeltjes weer gewoon metaal; ze zijn dan veel minder effectief in het omzetten van CO. Dit hebben we kunnen concluderen door metingen uit Leiden, Delft en Grenoble te combineren: de microscopie in Leiden en Delft liet zien dat de vormveranderingen van de palladiumdeeltjes heel subtiel waren, en daardoor wisten we hoe we de röntgenmetingen uit Grenoble moesten interpreteren en hebben we kunnen aantonen dat de ultradunne oxidelaagjes een rol spelen.

De laatste drie hoofdstukken laten heel duidelijk zien dat het gebruik van één meettechniek maar beperkt informatie oplevert, en dat de belangrijke inzichten

komen door het combineren van meerdere technieken. Individueel zijn de gebruikte meettechnieken al bijzonder omdat ze het beste van twee werelden combineren, de katalyse plus de oppervlaktefysica. Maar echt krachtig wordt het als meerdere van dit soort technieken gecombineerd worden. Het vergt enige organisatie om voldoende expertise over de verschillende vakgebieden samen te brengen, maar het resultaat is grensverleggend onderzoek en unieke informatie.
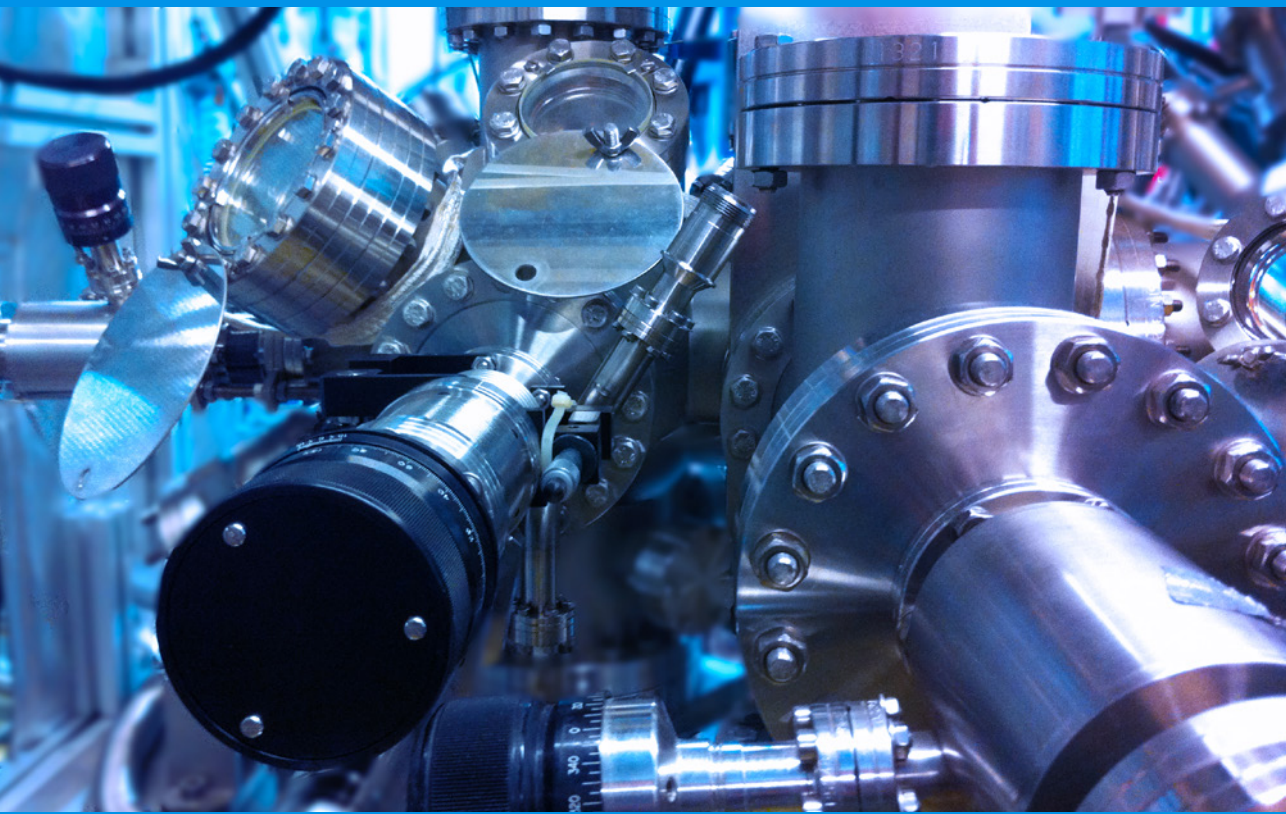
Acknowledgements

Many people have contributed in some way to the work described in this thesis, many more than can be mentioned here.

Apart from providing scientific guidance and encouragement, my promotor Joost Frenken paved the way for the joint experiments with Delft University of Technology and the European Synchrotron Radiation Facility (ESRF), in part via the NIMIC public-private partnership that also provided funding for this project.

At Leiden University, Mirthe Bergman and Peter van der Tuijn from the Fine Mechanical department played an essential role in the design and fabrication of the ReactorAFM, and my former colleague Marta Cañas-Ventura must be credited for the exceptional start of this line of development. Chapters 4 and 7 are the result of a joint effort with Willem Onderwaater. My (former) colleagues Matthijs van Spronsen, Richard van Rijn, Femke Tabak, Jan-Willem Beenakker, Marcel Rost, Johan Bakker, Irene Groot, Violeta Navarro, Kees Herbschleb, Rik Mom, Qian Liu, Marien Bremmer, Maarten van Es, and Tjerk Oosterkamp provided valuable input in scientific discussions and technical support. Chris Smiet, Jeroen Kraaij, and Olfa Jaïbi performed their BSc or MSc research projects in the context of the work described in this thesis. Raymond Koehler and Martin Moene from the Electronics Department provided assistance with the scanning probe electronics and software. Gertjan van Baarle and Alexei Ofitserof from the spin-off company Leiden Probe Microscopy provided technical support beyond what can be expected from a commercial company.

For the X-ray experiments I am grateful to the current and former ID03 beamline staff of the ESRF, in particular Roberto Felici, Olivier Balmes, Franscesco Carla, Jakub Drnec, Didier Wermeille, Andrea Resta, Helena Isern and Tomas Dufrane, for their input in scientific discussions, for technical support, and for participating in the measurements. Maria Messing from Lund University provided the size-selected Pd nanoparticle samples used in chapter 7. Marco Saluzzo provided the $SrTiO_3$ sample dataset for BINoculars, and Sabrina Disch the $(PbSe)_{4+\delta}(TiSe_2)_4$ dataset.

Access to the electron microscopy facility at TU Delft has been provided by Henny Zandbergen with technical support from Frans Tichelaar. Fredrik Creemer, also from TU Delft, provided the nanoreactors. Patricia Kooyman and Søren Vendelbo from TU Delft, and Christian Elkjær and Stig Helvig from Haldor Topsøe provided electron microscopy expertise and input to scientific discussions.
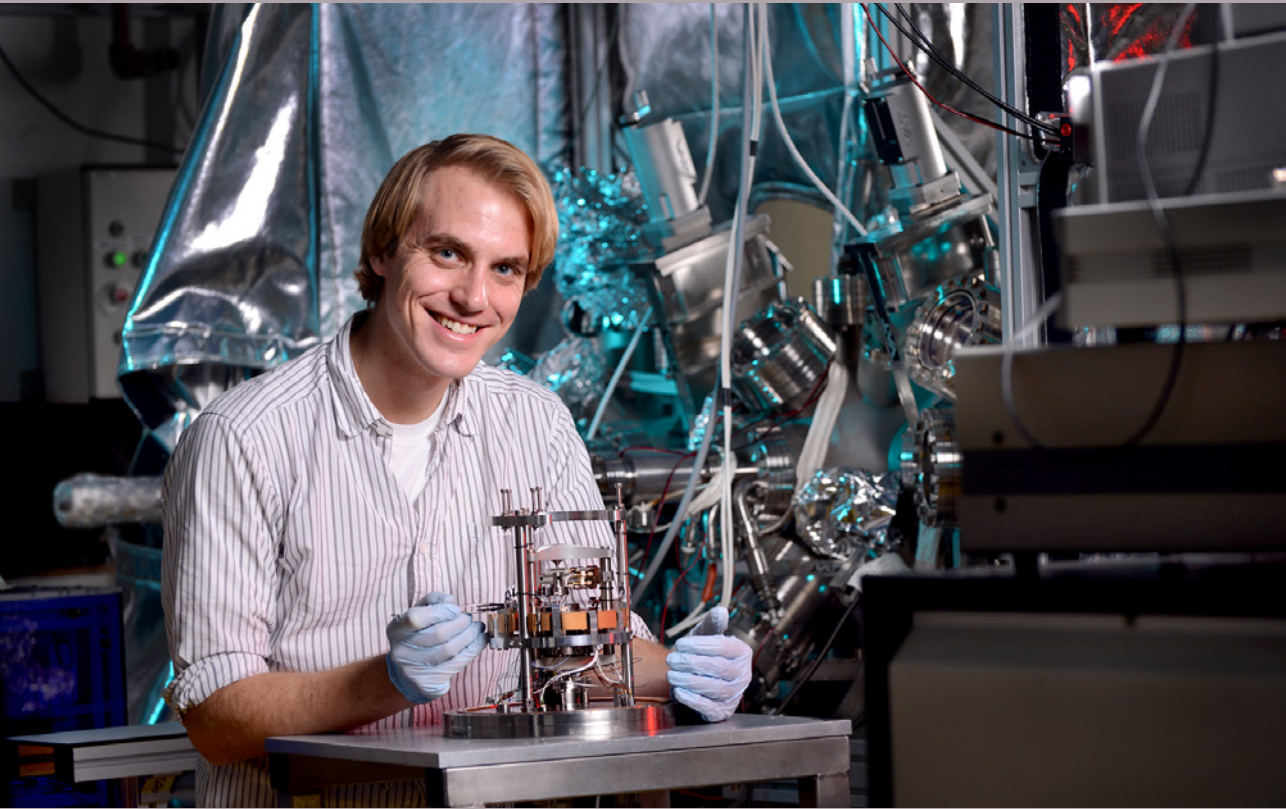
Curriculum vitae

Sander Bas Roobol was born on September 30, 1985 in Zeist. He got his Gymnasium degree from the Theresialyceum in Tilburg in 2003, and went to Leiden to study mathematics and physics at Leiden University. After obtaining a BSc in Mathematics and a BSc in Physics, both in 2008, he continued with a Masters track in experimental physics. Under supervision of Dr. Ir. W. M. van Spengen he worked on a project on Micro Electro-Mechanical Systems (MEMS) before moving into the field of surface science and catalysis for an internship at the European Synchrotron Radiation Facility (ESRF) in Grenoble, France. In this project, which was supervised by Dr. R. Felici, he investigated the Fischer-Tropsch process using Surface X-ray Diffraction, and this resulted in him obtaining an MSc in Physics in 2010.

He went on to pursue a PhD under the supervision of Prof. Dr. J. W. M. Frenken, which was focused on the development of high-pressure, high-temperature surface-science instrumentation for in-situ studies on heterogeneous catalysis, and the application of such equipment to catalytic model systems. He used a combination of scanning probe microscopy, electron microscopy, and X-ray scattering to investigate several model systems concerning the catalytic conversion of CO and NO. This work is described in this thesis.

Sander Roobol continues his career as a researcher at ASML in Veldhoven.
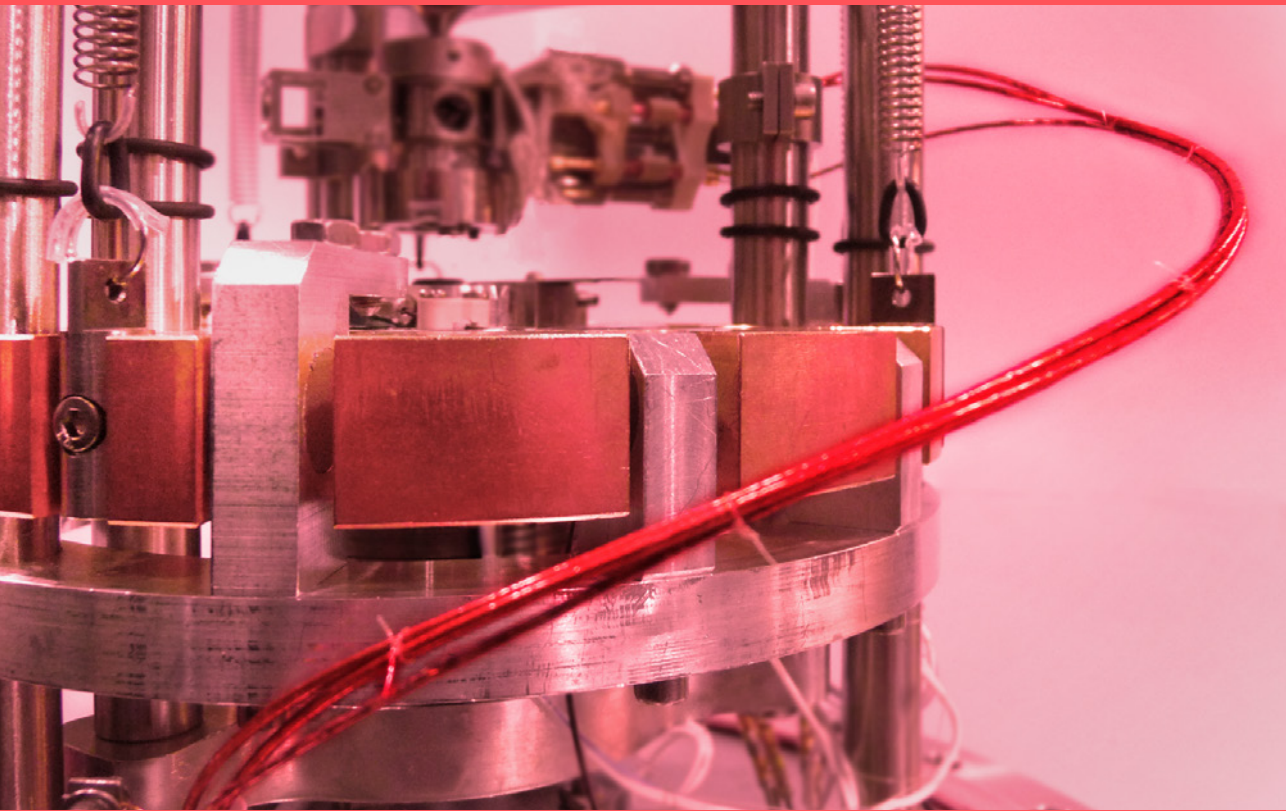
Based on a photo by Kees Herbschleb.

List of publications

S. B. Roobol, M. E. Cañas-Ventura, M. Bergman, M. A. van Spronsen, W. G. Onderwaater, P. C. van der Tuijn, R. Koehler, A. Ofitserov, G. J. C. van Baarle and J. W. M. Frenken, "The *ReactorAFM*: Non-Contact Atomic Force Microscope operating under high-pressure and high-temperature catalytic conditions", submitted (chapter 2).

S. B. Roobol, "*Spacetime*: analysis software for microscopy data of dynamical processes", submitted (chapter 3).

S. B. Roobol, W. G. Onderwaater, J. Drnec and R. Felici, "*BINoculars*: data reduction and analysis software for two-dimensional detectors in surface x-ray diffraction", submitted (chapter 4).

S. B. Roobol, W. G. Onderwaater, M. A. van Spronsen, F. Carla, O. Balmes, V. Navarro, S. Vendelbo, P.J. Kooyman, C. F. Elkjær, S. Helveg, R. Felici and J. W. M. Frenken, "Restructuring of Pt surfaces during high-pressure, high-temperature NO and H_2 exposure", in preparation (chapter 5 and 6).

W. G. Onderwaater, S.B. Roobol, R. van Rijn, O. Balmes, M.E. Cañas Ventura, M.E. Messing, A. Resta, D. Wermeille, R. Westerström, K. Deppert, E. Lundgren, S. Vendelbo, P. J. Kooyman, C. F. Elkjær, S. Helveg, R. Felici and J. W. M. Frenken, "Oxide shell formation during spontaneous oscillations in the catalytic oxidation of CO on palladium nanoparticles", in preparation (chapter 7).

C. T. Herbschleb, P. C. van der Tuijn, S. B. Roobol, V. Navarro, J. Bakker, Q. Liu, D. Stoltz, M. E. Cañas-Ventura, G. Verdoes, M. A. van Spronsen, M. Bergman, L. Crama, I. Taminiau, A. Ofitserov, G. J. C. van Baarle and J. W. M. Frenken, "The ReactorSTM: Atomically resolved scanning tunneling microscopy under high-pressure, high-temperature catalytic reaction conditions", *Review of Scientific Instruments* **85**, 083703 (2014), DOI: 10.1063/1.4891811

W. M. van Spengen, S. B. Roobol, W. P. Klaassen and T. H. Oosterkamp, "The MEMSamp: using (RF-)MEMS switches for the micromechanical amplification of electronic signals", *Journal of Micromechanics and Microengineering* **20**, 125011 (2010), DOI: 10.1088/0960-1317/20/12/125011

Y. S. Avotina, Y. A. Kolesnichenko, S. B. Roobol and J. M. van Ruitenbeek, "Conductance of a tunnel point contact of noble metals in the presence of a single defect", *Low Temperature Physics* **34**, 207 (2008), DOI: 10.1063/1.2889410

Bibliography

[1] F. Besenbacher, "Design of a Surface Alloy Catalyst for Steam Reforming", *Science* **279**, 1913 (1998), DOI: 10.1126/science.279.5358.1913.

[2] T. F. Jaramillo, K. P. Jorgensen, J. Bonde, J. H. Nielsen, S. Horch, and I. Chorkendorff, "Identification of Active Edge Sites for Electrochemical H2 Evolution from MoS2 Nanocatalysts", *Science* **317**, 100 (2007), DOI: 10.1126/science.1141483.

[3] G. Ertl, H. Knözinger, F. Schüth, and J. Weitkamp, eds., *Handbook of Heterogeneous Catalysis*, Wiley, 2008, ISBN: 978-3-527-31241-2.

[4] H. Ibach, *Physics of Surfaces and Interfaces*, Springer, 2006, ISBN: 978-3-540-34709-5.

[5] G. A. Somorjai and M. A. Van Hove, "Adsorbate-induced restructuring of surfaces", *Progress in Surface Science* **30**, 201 (1989), DOI: 10.1016/0079-6816(89)90009-9.

[6] B. Corain, G. Schmid, and N. Toshima, eds., *Metal Nanoclusters in Catalysis and Materials Science*, Elsevier, 2011, ISBN: 978-0-444-53057-8.

[7] B. Balamurugan and T. Maruyama, "Evidence of an enhanced interband absorption in Au nanoparticles: Size-dependent electronic structure and optical properties", *Applied Physics Letters* **87**, 143105 (2005), DOI: 10.1063/1.2077834.

[8] W. C. Conner Jr and J. L. Falconer, "Spillover in heterogeneous catalysis", *Chemical Reviews* **95**, 759 (1995), DOI: 10.1021/cr00035a014.

[9] J. Y. Park, J. R. Renzas, A. M. Contreras, and G. A. Somorjai, "The genesis and importance of oxide–metal interface controlled heterogeneous catalysis; the catalytic nanodiode", *Topics In Catalysis* **46**, 217 (2007), DOI: 10.1007/s11244-007-0331-7.

[10] J. W. M. Frenken and B. L. M. Hendriksen, "The Reactor-STM: A Real-Space Probe for Operando Nanocatalysis", *MRS Bulletin* **32**, 1015 (2007), DOI: 10.1557/mrs2007.210.

[11]   C. T. Herbschleb, P. C. van der Tuijn, S. B. Roobol, V. Navarro, J. W. Bakker, Q. Liu, D. Stoltz, M. E. Cañas-Ventura, G. Verdoes, M. A. van Spronsen, M. Bergman, L. Crama, I. Taminiau, A. Ofitserov, G. J. C. van Baarle, and J. W. M. Frenken, "The ReactorSTM: Atomically resolved scanning tunneling microscopy under high-pressure, high-temperature catalytic reaction conditions", *Review of Scientific Instruments* **85**, 083703 (2014), DOI: 10.1063/1.4891811.

[12]   P. L. Gai, E. D. Boyes, S. Helveg, P. L. Hansen, S. Giorgio, and C. R. Henry, "Atomic-Resolution Environmental Transmission Electron Microscopy for Probing Gas-Solid Reactions in Heterogeneous Catalysis", *MRS Bulletin* **32**, 1044 (2007), DOI: 10.1557/mrs2007.214.

[13]   J. F. Creemer, F. Santagata, B. Morana, L. Mele, T. Alan, E. Iervolino, G. Pandraud, and P. M. Sarro, "An all-in-one nanoreactor for high-resolution microscopy on nanomaterials at high pressures", *Proceedings of the IEEE 24th International Conference on Micro Electro Mechanical Systems* 1103 (2011), DOI: 10.1109/MEMSYS.2011.5734622.

[14]   S. Ferrer, M. Ackermann, and E. Lundgren, "In Situ Investigations of Chemical Reactions on Surfaces by X-Ray Diffraction at Atmospheric Pressures", *MRS Bulletin* **32**, 1010 (2007), DOI: 10.1557/mrs2007.209.

[15]   D. D. Fong, C. A. Lucas, M. Richard, and M. F. Toney, "X-ray probes for in situ studies of interfaces", *MRS Bulletin* **35**, 504 (2010), DOI: 10.1557/mrs2010.599.

[16]   J. Evans, A. Puig-Molina, and M. Tromp, "In Situ EXAFS Characterization of Nanoparticulate Catalysts", *MRS Bulletin* **32**, 1038 (2007), DOI: 10.1557/mrs2007.213.

[17]   H. Bluhm, M. Havecker, A. Knop-Gericke, M. Kiskinova, R. Schlogl, and M. Salmeron, "In Situ X-Ray Photoelectron Spectroscopy Studies of Gas-Solid Interfaces at Near-Ambient Conditions", *MRS Bulletin* **32**, 1022 (2007), DOI: 10.1557/mrs2007.211.

[18]   G. Rupprechter, "Sum Frequency Laser Spectroscopy during Chemical Reactions on Surfaces", *MRS Bulletin* **32**, 1031 (2007), DOI: 10.1557/mrs2007.212.

[19]   J. K. Norskov, M. Scheffler, and H. Toulhoat, "Density functional theory in surface science and heterogeneous catalysis", *MRS Bulletin* **31**, 669 (2006), DOI: 10.1557/mrs2006.175.

[20]   J. Rogal, K. Reuter, and M. Scheffler, "CO oxidation on Pd(100) at technologically relevant pressure conditions: First-principles kinetic Monte Carlo study", *Physical Review B* **77**, 155410 (2008), DOI: 10.1103/PhysRevB.77.155410.

[21]   S. Matera and K. Reuter, "When atomic-scale resolution is not enough: Spatial effects on in situ model catalyst studies", *Journal of Catalysis* **295**, 261 (2012), DOI: 10.1016/j.jcat.2012.08.020.

[22]   R. van Rijn, M. Ackermann, O. Balmes, T. Dufrane, A. Geluk, H. Gonzalez, H. Isern, E. de Kuyper, L. Petit, V. A. Sole, D. Wermeille, R. Felici, and J. W. M. Frenken, "Ultrahigh vacuum/high-pressure flow reactor for surface x-ray diffraction and grazing incidence small angle x-ray scattering studies close to conditions for industrial catalysis", *Review of Scientific Instruments* **81**, 014101 (2010), DOI: 10.1063/1.3290420.

[23]   J. F. Creemer, S. Helveg, G. H. Hoveling, S. Ullmann, A. M. Molenbroek, P. M. Sarro, and H. W. Zandbergen, "Atomic-scale electron microscopy at ambient pressure", *Ultramicroscopy* **108**, 993 (2008), DOI: 10.1016/j.ultramic. 2008.04.014.

[24]   B. J. McIntyre, M. Salmeron, and G. A. Somorjai, "A scanning tunneling microscope that operates at high pressures and high temperatures (430 K) and during catalytic reactions", *Catalysis Letters* **14**, 263 (1992), DOI: 10.1007/BF00769663.

[25]   M. A. van Spronsen, G. J. C. van Baarle, C. T. Herbschleb, J. W. M. Frenken, and I. M. N. Groot, "High-pressure operando STM studies giving insight in CO oxidation and NO reduction over Pt(110)", *Catalysis Today* in press (2014), DOI: 10.1016/j.cattod.2014.07.008.

[26]   D. D'Agostino, D. Jay, and H. McNally, "Development and testing of hyperbaric atomic force microscopy (AFM) for biological applications", *Microscopy and Microanalysis* **16**, 1042 (2010), DOI: 10.1017/S1431927610057739.

[27]   J. Lievonen, K. Ranttila, and M. Ahlskog, "Environmental chamber for an atomic force microscope", *Review of Scientific Instruments* **78**, 043703 (2007), DOI: 10.1063/1.2719598.

[28]   S. R. Higgins, C. M. Eggleston, K. G. Knauss, and C. O. Boro, "A hydrothermal atomic force microscope for imaging in aqueous solution up to 150 C", *Review of Scientific Instruments* **69**, 2994 (1998), DOI: 10.1063/1.1149226.

[29]   A. S. Lea, S. R. Higgins, K. G. Knauss, and K. M. Rosso, "A high-pressure atomic force microscope for imaging in supercritical carbon dioxide", *Review of Scientific Instruments* **82**, 043709 (2011), DOI: 10.1063/1.3580603.

[30]   F. J. Giessibl, S. Hembacher, and H. Bielefeldt, "Subatomic features on the silicon $(111) - (7 \times 7)$ surface observed by atomic force microscopy", *Science* **289**, 422 (2000), DOI: 10.1126/science.289.5478.422.

[31] L. Gross, F. Mohn, N. Moll, P. Liljeroth, and G. Meyer, "The Chemical Structure of a Molecule Resolved by Atomic Force Microscopy", *Science* **325**, 1110 (2009), DOI: `10.1126/science.1176210`.

[32] F. J. Giessibl, "High-speed force sensor for force microscopy and profilometry utilizing a quartz tuning fork", *Applied Physics Letters* **73**, 3956 (1998), DOI: `10.1063/1.122948`.

[33] *EBL #2, EBL Products*, URL: `http://www.eblproducts.com/`.

[34] Z. Xue, M. J. Strouse, D. K. Shuh, C. B. Knobler, H. D. Kaesz, R. F. Hicks, and R. S. Williams, "Characterization of (methylcyclopentadienyl)trimethylplatinum and low-temperature organometallic chemical vapor deposition of platinum metal", *Journal of the American Chemical Society* **111**, 8779 (1989), DOI: `10.1021/ja00206a002`.

[35] *Corning Inc.* URL: `http://www.corning.com/`.

[36] A. Botman, M. Hesselberth, and J. J. L. Mulders, "Improving the conductivity of platinum-containing nano-structures created by electron-beam-induced deposition", *Microelectronic Engineering* **85**, 1139 (2008), DOI: `10.1016/j.mee.2007.12.036`.

[37] F. J. Giessibl, "Advances in atomic force microscopy", *Reviews of Modern Physics* **75**, 949 (2003), DOI: `10.1103/RevModPhys.75.949`.

[38] R. Grober, J. Acimovic, J. Schuck, D. Hessman, P. J. Kindlemann, J. Hespanha, and A. S. Morse, "Fundamental limits to force detection using quartz tuning forks", *Review of Scientific Instruments* **71**, 2776 (2000), DOI: `10.1063/1.1150691`.

[39] M. J. Rost, L. Crama, P. Schakel, E. van Tol, G. van Velzen-Williams, C. F. Overgauw, H. Ter Horst, H. Dekker, B. Okhuijsen, and M. Seynen, "Scanning probe microscopes go video rate and beyond", *Review of Scientific Instruments* **76**, 053710 (2005), DOI: `10.1063/1.1915288`.

[40] M. E. Messing, R. Westerström, B. O. Meuller, S. Blomberg, J. Gustafson, J. N. Andersen, E. Lundgren, R. van Rijn, O. Balmes, H. Bluhm, and K. Deppert, "Generation of Pd Model Catalyst Nanoparticles by Spark Discharge", *Journal of Physical Chemistry C* **114**, 9257 (2010), DOI: `10.1021/jp101390a`.

[41] J. S. Villarrubia, "Algorithms for scanned probe microscope image simulation, surface reconstruction, and tip estimation", *Journal of Research of NIST* **102**, 425 (1997), DOI: `10.6028/jres.102.030`.

[42] E. P. Eernisse, R. W. Ward, and R. B. Wiggins, "Survey of quartz bulk resonator sensor technologies", *IEEE Transactions on Ultrasonics, Ferroelectrics and Frequency Control* **35**, 323 (1988), DOI: `10.1109/58.20453`.

[43] K. Keiji Kanazawa and J. G. Gordon II, "The oscillation frequency of a quartz resonator in contact with liquid", *Analytica Chimica Acta* **175**, 99 (1985), DOI: 10.1016/S0003-2670(00)82721-X.

[44] R. Hooke, *Micrographia: or some Physiological Descriptions of Minute Bodies Made by Magnifying Glasses with Observations and Inquiries Thereupon*, John Martyn and James Allestry, London, 1665.

[45] B. L. M. Hendriksen and J. W. M. Frenken, "CO oxidation on Pt(110): Scanning tunneling microscopy inside a high-pressure flow reactor", *Physical Review Letters* **89**, 046101 (2002), DOI: 10.1103/PhysRevLett.89.046101.

[46] S.B. Roobol, M.E. Cañas-Ventura, M. Bergman, M.A. van Spronsen, W. Onderwaater, P.C. van der Tuijn, R. Koehler, A. Ofitserov, G.J.C. van Baarle, and J.W.M. Frenken, *The ReactorAFM: Non-Contact Atomic Force Microscope operating under high-pressure and high-temperature catalytic conditions*, submitted.

[47] E. de Smit, I. Swart, J. F. Creemer, C. Karunakaran, D. Bertwistle, H. W. Zandbergen, F. M. F. de Groot, and B. M. Weckhuysen, "Nanoscale Chemical Imaging of the Reduction Behavior of a Single Catalyst Particle", *Angewandte Chemie International Edition* **48**, 3632 (2009), DOI: 10.1002/anie.200806003.

[48] T. Yokosawa, T. Alan, G. Pandraud, B. Dam, and H. Zandbergen, "In-situ TEM on (de)hydrogenation of Pd at 0.5–4.5bar hydrogen pressure and 20–400°C", *Ultramicroscopy* **112**, 47 (2012), DOI: 10.1016/j.ultramic.2011.10.010.

[49] M. Rudneva, B. Gao, F. Prins, Q. Xu, H. S. J. van der Zant, and H. W. Zandbergen, "In Situ Transmission Electron Microscopy Imaging of Electromigration in Platinum Nanowires", *Microscopy and Microanalysis* **19**, 43 (2013), DOI: 10.1017/S1431927613012300.

[50] Y. Yanson, J. W. M. Frenken, and M. J. Rost, "A general model of metal underpotential deposition in the presence of thiol-based additives based on an in situ STM study", *Physical Chemistry Chemical Physics* **13**, 16095 (2011), DOI: 10.1039/c1cp20886a.

[51] Y. I. Yanson, F. Schenkel, and M. J. Rost, "Design of a high-speed electrochemical scanning tunneling microscope", *Review of Scientific Instruments* **84**, 023702 (2013), DOI: 10.1063/1.4779086.

[52] F. Pérez, B. E. Granger, and J. D. Hunter, "Python: an ecosystem for scientific computing", *Computing in Science & Engineering* **13**, 13 (2011), DOI: 10.1109/MCSE.2010.119.

[53] T. E. Oliphant, "Python for scientific computing", *Computing in Science & Engineering* **9**, 10 (2007).

[54] J. D. Hunter, "Matplotlib: A 2D graphics environment", *Computing In Science & Engineering* **9**, 90 (2007).

[55] *Enthought Tools Suite*, URL: http://www.enthought.com/.

[56] *Leiden Probe Microscopy B.V.* URL: http://www.leidenprobemicroscopy.com/.

[57] *Gatan Inc.* URL: http://www.gatan.com/.

[58] *TVIPS GmbH*, URL: http://www.tvips.com/.

[59] *Pfeiffer Vacuum GmbH*, URL: http://www.pfeiffer-vacuum.com/.

[60] *Stanford Research Systems*, URL: http://www.thinksrs.com/.

[61] *MKS Instruments*, URL: http://www.mksinstr.com/.

[62] *Spacetime*, URL: http://spacetime.uithetblauw.nl/.

[63] *GNU General Public License*, URL: http://www.gnu.org/licenses/gpl.html.

[64] C. Ponchut, J. M. Rigal, J. Clément, E. Papillon, A. Homs, and S. Petitdemange, "MAXIPIX, a fast readout photon-counting X-ray area detector for synchrotron applications", *Journal of Instrumentation* **6**, C01069 (2011), DOI: 10.1088/1748-0221/6/01/C01069.

[65] U. W. Arndt and D. C. Phillips, "The linear diffractometer", *Acta Crystallographica* **14**, 807 (1961), DOI: 10.1107/S0365110X61002394.

[66] R. Shayduk and W. Braun, "Positioning errors during stepped scans in X-ray crystallography", *Journal of Applied Crystallography* **41**, 768 (2008), DOI: 10.1107/S0021889808018256.

[67] H. Winick, "Synchrotron Radiation Sources - Present Capabilities and Future Directions", *Journal of Synchrotron Radiation* **5**, 168 (1998), DOI: 10.1107/S0909049597018761.

[68] E. Vlieg, "Integrated intensities using a six-circle surface X-ray diffractometer", *Journal of Applied Crystallography* **30**, 532 (1997), DOI: 10.1107/S0021889897002537.

[69] J. Drnec, T. Zhou, S. Pintea, W. Onderwaater, E. Vlieg, G. Renaud, and R. Felici, "Integration techniques for surface X-ray diffraction data obtained with a two-dimensional detector", *Journal of Applied Crystallography* **47**, 365 (2014), DOI: 10.1107/S1600576713032342.

[70] J. Kieffer and D. Karkoulis, "PyFAI, a versatile library for azimuthal regrouping", *Journal of Physics: Conference Series* **425**, 202012 (2013), DOI: 10.1088/1742-6596/425/20/202012.

[71] D. Kriegner, E. Wintersberger, and J. Stangl, "xrayutilities: a versatile tool for reciprocal space conversion of scattering data recorded with linear and area detectors", *Journal of Applied Crystallography* **46**, 1162 (2013), DOI: 10.1107/S0021889813017214.

[72] O. Balmes, R. van Rijn, D. Wermeille, A. Resta, L. Petit, H. Isern, T. Dufrane, and R. Felici, "The ID03 surface diffraction beamline for in-situ and real-time X-ray investigations of catalytic reactions at surfaces", *Catalysis Today* **145**, 220 (2009), DOI: 10.1016/j.cattod.2009.02.008.

[73] *OAR resource and task manager*, URL: http://oar.imag.fr/.

[74] M. Folk, G. Heber, Q. Koziol, E. Pourmal, and D. Robinson, "An overview of the HDF5 technology suite and its applications", *Proceedings of the EDBT/ICDT 2011 Workshop on Array Databases* 36 (2011), DOI: 10.1145/1966895.1966900.

[75] E. Vlieg, "ROD: a program for surface X-ray crystallography", *Journal of Applied Crystallography* **33**, 401 (2000), DOI: 10.1107/S0021889899013655.

[76] I.K. Robinson, *Handbook on Synchrotron Radiation*, ed. by G.S. Brown and D.E. Moncton, vol. III, Elsevier, 1991, chap. 7, ISBN: 978-0-444-87422-1.

[77] J. V. Barth, H. Brune, G. Ertl, and R. J. Behm, "Scanning tunneling microscopy observations on the reconstructed Au(111) surface: Atomic structure, long-range superstructure, rotational domains, and surface defects", *Physical Review B* **42**, 9307 (1990), DOI: 10.1103/PhysRevB.42.9307.

[78] P. Steadman, K. Peters, H. Isern, J. Alvarez, and S. Ferrer, "Interaction of CO with the reconstructed Au(111) surface near atmospheric pressures", *Physical Review B* **62**, R2295 (2000), DOI: 10.1103/PhysRevB.62.R2295.

[79] K. F. Peters, P. Steadman, H. Isern, J. Alvarez, and S. Ferrer, "Elevated-pressure chemical reactivity of carbon monoxide over Au(111)", *Surface Science* **467**, 10 (2000), DOI: 10.1016/S0039-6028(00)00777-9.

[80] M. Salluzzo, S. Gariglio, X. Torrelles, Z. Ristic, R. Di Capua, J. Drnec, M. M. Sala, G. Ghiringhelli, R. Felici, and N. B. Brookes, "Structural and Electronic Reconstructions at the $LaAlO_3$/$SrTiO_3$ Interface", *Advanced Materials* **25**, 2333 (2013), DOI: 10.1002/adma.201204555.

[81] D. B. Moore, M. Beekman, S. Disch, and D. C. Johnson, "Telluride Misfit Layer Compounds: $[(PbTe)_{1.17}]_m(TiTe_2)_n$", *Angewandte Chemie International Edition* **53**, 5672 (2014), DOI: 10.1002/anie.201401022.

[82] J. Gustafson, M. Shipilin, C. Zhang, A. Stierle, U. Hejral, U. Ruett, O. Gutowski, P. A. Carlsson, M. Skoglundh, and E. Lundgren, "High-Energy Surface X-ray Diffraction for Fast Surface Structure Determination", *Science* **343**, 758 (2014), DOI: 10.1126/science.1246834.

[83]   *BINoculars*, URL: http://binoculars.uithetblauw.nl/.

[84]   R. M. Heck and R. J. Farrauto, "Automobile exhaust catalysts", *Applied Catalysis A, General* **221**, 443 (2001), DOI: 10.1016/S0926-860X(01)00818-3.

[85]   M. Shelef, "Nitric oxide: surface reactions and removal from auto exhaust", *Catalysis Reviews Science and Engineering* **11**, 1 (1975), DOI: 10.1080/01614947508079980.

[86]   B. E. Nieuwenhuys, "The surface science approach toward understanding automotive exhaust conversion catalysis at the atomic level", *Advances in catalysis* **44**, 259 (1999).

[87]   C. M. Comrie, W. H. Weinberg, and R. M. Lambert, "The adsorption of nitric oxide on Pt(111) and Pt(110) surfaces", *Surface Science* **57**, 619 (1976), DOI: 10.1016/0039-6028(76)90351-4.

[88]   R. J. Gorte, L. D. Schmidt, and J. L. Gland, "Binding states and decomposition of NO on single crystal planes of Pt", *Surface Science* **109**, 367 (1981), DOI: 10.1016/0039-6028(81)90494-5.

[89]   R. J. Gorte and J. L. Gland, "Nitric oxide adsorption on the Pt(110) surface", *Surface Science* **102**, 348 (1981), DOI: 10.1016/0039-6028(81)90034-0.

[90]   W. A. Brown, Q. Ge, R. K. Sharma, and D. A. King, "Lateral potential energy surfaces for molecular chemisorption on metals from experiment and theory: NO on Pt(110)-(1 × 2)", *Chemical physics letters* **299**, 253 (1999), DOI: 10.1016/S0009-2614(98)01272-X.

[91]   W. A. Brown, R. K. Sharma, and D. A. King, "Site switching and surface restructuring induced by NO adsorption on Pt(110)", *Journal of Physical Chemistry B* **102**, 5303 (1998), DOI: 10.1021/jp981061a.

[92]   M. Minca, S. Penner, T. Loerting, A. Menzel, E. Bertel, R. Zucca, and J. Redinger, "Chemisorption of hydrogen on the missing-row Pt(110)-(1 × 2) surface", *Topics In Catalysis* **46**, 161 (2007), DOI: 10.1007/s11244-007-0326-4.

[93]   P. Gardner, M. Tüshaus, R. Martin, and A. M. Bradshaw, "The adsorbate-induced removal of the Pt(100) surface reconstruction Part I: NO", *Surface Science* **240**, 112 (1990), DOI: 10.1016/0039-6028(90)90735-Q.

[94]   J. Siera, P. Cobden, K. Tanaka, and B. E. Nieuwenhuys, "The NO-H$_2$ reaction over Pt(100): oscillatory behaviour of activity and selectivity", *Catalysis Letters* **10**, 335 (1991), DOI: 10.1007/BF00769168.

[95]   A. G. Makeev and B. E. Nieuwenhuys, "Mathematical modeling of the NO + H$_2$ / Pt(100) reaction: "Surface explosion," kinetic oscillations, and chaos", *Journal of Chemical Physics* **108**, 3740 (1998), DOI: 10.1063/1.475767.

[96]   P. Fery, W. Moritz, and D. Wolf, "Structure determination of the (1×2) and (1×3) reconstructions of Pt(110) by low-energy electron diffraction", *Physical Review B* **38**, 7275 (1988), DOI: 10.1103/PhysRevB.38.7275.

[97]   I. K. Robinson, P. J. Eng, C. Romainczyk, and K. Kern, "X-ray determination of the 1×3 reconstruction of Pt(110)", *Physical Review B* **47**, 10700 (1993), DOI: 10.1103/PhysRevB.47.10700.

[98]   Y. Kuk, P. J. Silverman, and H. Q. Nguyen, "Adsorbate-induced reconstruction in the Ni(110)-H system", *Physical Review Letters* **59**, 1452 (1987), DOI: 10.1103/PhysRevLett.59.1452.

[99]   R. Feidenhans'l, F. Grey, R. L. Johnson, and M. Nielsen, "Determination of the Cu(110)-c(6×2)-O structure by x-ray diffraction", *Physical Review B* **44**, 1875 (1991), DOI: 10.1103/PhysRevB.44.1875.

[100]   F. M. Leibsle, R. Davis, and A. W. Robinson, "Scanning-tunneling-microscopy studies of (2×3) N-induced structures, thermal desorption, and oxygen coadsorption on the Cu(110) surface", *Physical Review B* **49**, 8290 (1994), DOI: 10.1103/PhysRevB.49.8290.

[101]   I. K. Robinson, P. J. Eng, C. Romainczyk, and K. Kern, "Higher order reconstructions of Pt(110) induced by impurities", *Surface Science* **367**, 105 (1996), DOI: 10.1016/0039-6028(96)00810-2.

[102]   E. Kampshoff, N. Waelchli, A. Menck, and K. Kern, "Hydrogen-induced missing-row reconstructions of Pd(110) studied by scanning tunneling microscopy", *Surface Science* **360**, 55 (1996), DOI: 10.1016/0039-6028(96)00653-X.

[103]   P. J. Schmitz, W. Leung, H. C. Kang, and P. A. Thiel, "Reconstructions of Au films on Pd(110)", *Physical Review B* **43**, 8834 (1991), DOI: 10.1103/PhysRevB.43.8834.

[104]   S. M. Foiles, "Reconstruction of fcc (110) surfaces", *Surface Science Letters* **191**, L779 (1987), DOI: 10.1016/0167-2584(87)90889-9.

[105]   R. Feidenhans'l, "Surface structure determination by X-ray diffraction", *Surface Science Reports* **10**, 105 (1989).

[106]   S. Ladas, R. Imbihl, and G. Ertl, "Microfacetting of a Pt(110) surface during catalytic CO oxidation", *Surface Science* **197**, 153 (1988), DOI: 10.1016/0039-6028(88)90578-X.

[107]   M. Sander and R. Imbihl, "Conditions and kinetics of facetting of a Pt(110) surface during catalytic CO-oxidation", *Surface Science* **255**, 61 (1991), DOI: 10.1016/0039-6028(91)90011-G.

[108] S. Ladas, R. Imbihl, and G. Ertl, "Kinetic oscillations and facetting during the catalytic CO oxidation on Pt(110)", *Surface Science* **198**, 42 (1988), DOI: 10.1016/0039-6028(88)90471-2.

[109] T. Wang and K. Reuter, private communication.

[110] P. Hanesch and E. Bertel, "Mesoscopic Self-Organization Induced by Intrinsic Surface Stress on Pt(110)", *Physical Review Letters* **79**, 1523 (1997), DOI: 10.1103/PhysRevLett.79.1523.

[111] A. Grossmann, W. Erley, and H. Ibach, "Adsorbate-induced surface stress: CO on Ni(100) and Ni(111)", *Surface Science* **313**, 209 (1994), DOI: 10.1016/0039-6028(94)91168-1.

[112] D. Sander, U. Linke, and H. Ibach, "Adsorbate-induced surface stress: sulfur, oxygen and carbon on Ni(100)", *Surface Science* **272**, 318 (1992), DOI: 10.1016/0039-6028(92)91457-M.

[113] H. Häkkinen, M. Moseler, O. Kostko, N. Morgner, M. Hoffmann, and B. von Issendorff, "Symmetry and Electronic Structure of Noble-Metal Nanoparticles and the Role of Relativity", *Physical Review Letters* **93**, 093401 (2004), DOI: 10.1103/PhysRevLett.93.093401.

[114] C. Herring, "Some theorems on the free energies of crystal surfaces", *Physical Review* **82**, 87 (1951), DOI: 10.1103/PhysRev.82.87.

[115] M. A. Newton, C. Belver-Coldeira, A. Martínez-Arias, and M. Fernández-García, "Dynamic in situ observation of rapid size and shape change of supported Pd nanoparticles during CO/NO cycling", *Nature Materials* **6**, 528 (2007), DOI: 10.1038/nmat1924.

[116] M. A. Newton, M. D. Michiel, A. Kubacka, and M. Fernández-García, "Combining Time-Resolved Hard X-ray Diffraction and Diffuse Reflectance Infrared Spectroscopy To Illuminate CO Dissociation and Transient Carbon Storage by Supported Pd Nanoparticles during CO/NO Cycling", *Journal of the American Chemical Society* **132**, 4540 (2010), DOI: 10.1021/ja9107512.

[117] H. Yoshida, K. Matsuura, Y. Kuwauchi, H. Kohno, S. Shimada, M. Haruta, and S. Takeda, "Temperature-Dependent Change in Shape of Platinum Nanoparticles Supported on CeO_2 during Catalytic Reactions", *Applied Physics Express* **4**, 065001 (2011), DOI: 10.1143/APEX.4.065001.

[118] S. B. Vendelbo, C. F. Elkjær, H. Falsig, I. Puspitasari, P. Dona, L. Mele, B. Morana, B. J. Nelissen, R. van Rijn, J. F. Creemer, P. J. Kooyman, and S. Helveg, "Visualization of oscillatory behaviour of Pt nanoparticles catalysing CO oxidation", *Nature Materials* (2014), DOI: 10.1038/nmat4033.

[119] J. F. Creemer, S. Helveg, P. J. Kooyman, A. M. Molenbroek, H. W. Zandbergen, and P. M. Sarro, "A MEMS Reactor for Atomic-Scale Microscopy of Nanomaterials Under Industrially Relevant Conditions", *Journal of Microelectromechanical Systems* **19**, 254 (2010), DOI: 10.1109/JMEMS.2010.2041190.

[120] *T100 gas analyzer, Leiden Probe Microscopy B.V,*
URL: http://www.leidenprobemicroscopy.com/.

[121] B. K. Chakraverty, "Grain size distribution in thin films—1. Conservative systems", *Journal of Physics and Chemistry of Solids* **28**, 2401 (1967), DOI: 10.1016/0022-3697(67)90026-1.

[122] D. Kashchiev, "Kinetics Of Thin-Film Coalescence Due To Crystallite Surface Migration", *Surface Science* **55**, 477 (1976), DOI: 10.1016/0039-6028(76)90253-3.

[123] P. Loof, B. Stenbom, H. Norden, and B. Kasemo, "Rapid Sintering in NO of Nanometer-Sized Pt Particles on $\gamma-Al_2O_3$ Observed by CO Temperature-Programmed Desorption and Transmission Electron Microscopy", *Journal of Catalysis* **144**, 60 (1993), DOI: 10.1006/jcat.1993.1314.

[124] R. Imbihl and G. Ertl, "Oscillatory kinetics in heterogeneous catalysis", *Chemical Reviews* **95**, 697 (1995), DOI: 10.1021/cr00035a012.

[125] C. D. Lund, C. M. Surko, M. B. Maple, and S. Y. Yamamoto, "Model discrimination in oscillatory CO oxidation on platinum catalysts at atmospheric pressure", *Surface Science* **459**, 413 (2000), DOI: 10.1016/S0039-6028(00)00482-9.

[126] N. Hartmann, R. Imbihl, and W. Vogel, "Experimental evidence for an oxidation/reduction mechanism in rate oscillations of catalytic CO oxidation on Pt/SiO2", *Catalysis Letters* **28**, 373 (1994), DOI: 10.1007/BF00806068.

[127] J. Sá, D. L. A. Fernandes, F. Aiouache, A. Goguet, C. Hardacre, D. Lundie, W. Naeem, W. P. Partridge, and C. Stere, "SpaciMS: spatial and temporal operando resolution of reactions within catalytic monoliths", *The Analyst* **135**, 2260 (2010), DOI: 10.1039/c0an00303d.

[128] R. C. Yeates, J. E. Turner, A. J. Gellman, and G. A. Somorjai, "The oscillatory behavior of the CO oxidation reaction at atmospheric pressure over platinum single crystals: Surface analysis and pressure dependent mechanisms", *Surface Science* **149**, 175 (1985), DOI: 10.1016/S0039-6028(85)80021-2.

[129] S. Jakubith, H. H. Rotermund, W. Engel, A. von Oertzen, and G. Ertl, "Spatiotemporal concentration patterns in a surface reaction: Propagating and standing waves, rotating spirals, and turbulence", *Physical Review Letters* **65**, 3013 (1990), DOI: 10.1103/PhysRevLett.65.3013.

[130] M. Sander, R. Imbihl, and G. Ertl, "The mechanism of kinetic oscillations in catalytic oxidation of CO on Pt(210)", *Journal of Chemical Physics* **95**, 6162 (1991), DOI: 10.1063/1.461584.

[131] B. L. M. Hendriksen, M. Ackermann, R. van Rijn, D. Stoltz, I. Popa, O. Balmes, A. Resta, D. Wermeille, R. Felici, S. Ferrer, and J. W. M. Frenken, "The role of steps in surface catalysis and reaction oscillations", *Nature Chemistry* **2**, 730 (2010), DOI: 10.1038/nchem.728.

[132] P. Mars and D. W. van Krevelen, "Oxidations carried out by means of vanadium oxide catalysts", *Chemical Engineering Science* **3**, 41 (1954), DOI: 10.1016/S0009-2509(54)80005-4.

[133] R. Jensen, T. Andersen, A. Nierhoff, T. Pedersen, O. Hansen, S. Dahl, and I. Chorkendorff, "Self-sustained carbon monoxide oxidation oscillations on size-selected platinum nanoparticles at atmospheric pressure", *Physical Chemistry Chemical Physics* **15**, 2698 (2013), DOI: 10.1039/c2cp43684a.

[134] T. Schalow, B. Brandt, M. Laurin, S. Schauermann, S. Guimond, H. Kuhlenbeck, J. Libuda, and H. Freund, "Formation of interface and surface oxides on supported Pd nanoparticles", *Surface Science* **600**, 2528 (2006).

[135] T. Schalow, B. Brandt, M. Laurin, S. Schauermann, J. Libuda, and H. Freund, "CO oxidation on partially oxidized Pd nanoparticles", *Journal of Catalysis* **242**, 58 (2006).

[136] B. Brandt, T. Schalow, M. Laurin, S. Schauermann, J. Libuda, and H. Freund, "Oxidation, Reduction, and Reactivity of Supported Pd Nanoparticles: Mechanism and Microkinetics", *Journal of Physical Chemistry C* **111**, 938 (2007), DOI: 10.1021/jp0658086.

[137] K. Zorn, S. Giorgio, E. Halwax, C. R. Henry, H. Grönbeck, and G. Rupprechter, "CO Oxidation on Technological Pd$-$Al$_2$O$_3$ Catalysts: Oxidation State and Activity", *Journal of Physical Chemistry C* **115**, 1103 (2011), DOI: 10.1021/jp106235x.

[138] S. Penner, P. Bera, S. Pedersen, L. T. Ngo, J. J. W. Harris, and C. T. Campbell, "Interactions of O2 with Pd Nanoparticles on α-Al$_2$O$_3$(0001) at Low and High O2 Pressures", *Journal of Physical Chemistry B* **110**, 24577 (2006).

[139] N. Kasper, A. Stierle, P. Nolte, Y. Jin-Phillipp, T. Wagner, D. G. de Oteyza, and H. Dosch, "In situ oxidation study of MgO(100) supported Pd nanoparticles", *Surface Science* **600**, 2860 (2006), DOI: 10.1016/j.susc.2006.05.030.

[140] G. Renaud, R. Lazzari, and F. Leroy, "Probing surface and interface morphology with Grazing Incidence Small Angle X-Ray Scattering", *Surface Science Reports* **64**, 255 (2009), DOI: 10.1016/j.surfrep.2009.07.002.

[141] J. Rogal, K. Reuter, and M. Scheffler, "First-Principles Statistical Mechanics Study of the Stability of a Subnanometer Thin Surface Oxide in Reactive Environments: CO Oxidation at Pd(100)", *Physical Review Letters* **98**, 046101 (2007), DOI: 10.1103/PhysRevLett.98.046101.

[142] M. J. Hoffmann and K. Reuter, "CO Oxidation on Pd(100) versus PdO(101)-$(\sqrt{5} \times \sqrt{5})R27°$: First-Principles Kinetic Phase Diagrams and Bistability Conditions", *Topics In Catalysis* **57**, 159 (2013), DOI: 10.1007/s11244-013-0172-5.

[143] S. B. Vendelbo, P. J. Kooyman, J. F. Creemer, B. Morana, L. Mele, P. Dona, B. J. Nelissen, and S. Helveg, "Method for local temperature measurement in a nanoreactor for in situ high-resolution electron microscopy", *Ultramicroscopy* **133**, 72 (2013), DOI: 10.1016/j.ultramic.2013.04.004.

[144] R. Lazzari, "IsGISAXS: a program for grazing-incidence small-angle X-ray scattering analysis of supported islands", *Journal of Applied Crystallography* **35**, 406 (2002), DOI: 10.1107/S0021889802006088.

[145] A. R. Stokes, A. J. C. Wilson, and W. L. Bragg, "A method of calculating the integral breadths of Debye-Scherrer lines", *Mathematical Proceedings of the Cambridge Philosophical Society* **38**, 313 (1942), DOI: 10.1017/S0305004100021988.

[146] R. van Rijn, O. Balmes, A. Resta, D. Wermeille, R. Westerström, J. Gustafson, R. Felici, E. Lundgren, and J. W. M. Frenken, "Surface structure and reactivity of Pd(100) during CO oxidation near ambient pressures", *Physical Chemistry Chemical Physics* **13**, 13167 (2011), DOI: 10.1039/c1cp20989b.

[147] R. van Rijn, O. Balmes, R. Felici, J. Gustafson, D. Wermeille, R. Westerström, E. Lundgren, and J. W. M. Frenken, "Comment on "CO Oxidation on Pt-Group Metals from Ultrahigh Vacuum to Near Atmospheric Pressures. 2. Palladium and Platinum"", *Journal of Physical Chemistry C* **114**, 6875 (2010), DOI: 10.1021/jp911406x.

[148] F. Gao, Y. Wang, and D. W. Goodman, "Reply to "Comment on 'CO Oxidation on Pt-Group Metals from Ultrahigh Vacuum to Near Atmospheric Pressures. 2. Palladium and Platinum'"", *Journal of Physical Chemistry C* **114**, 6874 (2010), DOI: 10.1021/jp100134e.

[149] J. T. Hirvi, T. J. Kinnunen, M. Suvanto, T. A. Pakkanen, and J. K. Nørskov, "CO oxidation on PdO surfaces", *Journal of Chemical Physics* **133**, 084704 (2010), DOI: 10.1063/1.3464481.

[150] F. Gao, Y. Wang, Y. Cai, and D. W. Goodman, "CO Oxidation on Pt-Group Metals from Ultrahigh Vacuum to Near Atmospheric Pressures. 2. Palladium and Platinum", *Journal of Physical Chemistry C* **113**, 174 (2009), DOI: 10.1021/jp8077985.

[151] E. Wutscher and F. J. Giessibl, "Atomic force microscopy at ambient and liquid conditions with stiff sensors and small amplitudes", *Review of Scientific Instruments* **82**, 093703 (2011), DOI: 10.1063/1.3633950.

[152] J. M. Yuk, J. Park, P. Ercius, K. Kim, D. J. Hellebusch, M. F. Crommie, J. Y. Lee, A. Zettl, and A. P. Alivisatos, "High-Resolution EM of Colloidal Nanocrystal Growth Using Graphene Liquid Cells", *Science* **336**, 61 (2012), DOI: 10.1126/science.1217654.

[153] Effeietsanders, *Academiegebouw Leiden – Senaatskamer*, retouched to reduce reflections, Creative Commons BY-NC 3.0 NL, URL: http://commons.wikimedia.org/wiki/File:Academiegebouw_Leiden_-_Senaatskamer.JPG.

[154] Public domain, URL: http://en.wikipedia.org/wiki/File:Irving_Langmuir_and_Guglielmo_Marconi_in_lab.jpg.

[155] Ulf Seifert, *Carbonfilament*, Creative Commons BY-SA 3.0, URL: http://commons.wikimedia.org/wiki/File:Carbonfilament.jpg.

[156] BASF, *BASF catalysts*, Creative Commons BY-NC-ND 2.0, URL: http://www.flickr.com/photos/basf/7460836832.

[157] Jorge Franganillo, *Solvay Martorell*, Creative Commons BY 2.0, URL: http://www.flickr.com/photos/franganillo/3129290866.